Flow Controlled Solvent Vapor Annealing of Block Copolymers for Lithographic Applications

by

Kevin Willy Gotrik

B.S. Engineering Physics
University of Wisconsin - Madison (2008)

Submitted to the Department of Materials Science and Engineering
in partial fulfillment of the requirements for the degree of

Doctor of Science in Materials Science and Engineering

at the

MASSACHUSETTS INSTITUTE OF TECHNOLOGY

June 2013

© Massachusetts Institute of Technology 2013. All rights reserved.

Author .....
Department of Materials Science and Engineering
May 17, 2013

Certified by .....
Caroline A. Ross
Toyota Professor of Materials Science and Engineering
Thesis Supervisor

Accepted by .....
Gerbrand Ceder
R. P. Simmons Professor of Materials Science and Engineering
Chair, Departmental Committee on Graduate Students

Flow Controlled Solvent Vapor Annealing of Block Copolymers for Lithographic Applications

by

Kevin Willy Gotrik

Submitted to the Department of Materials Science and Engineering
on May 17, 2013, in partial fulfillment of the
requirements for the degree of
Doctor of Science in Materials Science and Engineering

Abstract

Self-assembly of block copolymer thin-films may provide an inexpensive alternative to patterning lithographic features below the resolution limits of traditional optical methods. Block copolymers (BCPs) are polymers made of two or more distinct monomer/block units that are covalently bonded. Due to their differences in surface energy, the different blocks tend to phase segregate like oil and water; but because of the covalent linkage, this segregation is practically limited to size scales ranging from only a few nm to $\approx$ 100 nm. A thin film of a BCP can be used in much the same way as a photoresist in the lithographic process, whereas a desired pattern morphology can be obtained by etching one block away and leaving behind a self-assembled hard mask for the underlying substrate.

After a thin film of BCP is coated onto a given substrate, the BCP must be given an annealing step, where the disordered entangled polymer networks can be allowed to diffuse and equilibrate into lower free energy configurations which result in periodic patterns of micelles with different morphologies such as spheres, in/out of plane cylinders, etc. This work explored the technique of solvent vapor annealing, where organic solvents were allowed to interact with BCP thin films to facilitate annealing and act as surrogates for the different BCP polymer blocks. This allowed for a wide range of control over the BCP self-assembly (morphology, periodicity, etc.) for a given molecular weight BCP. Additionally, by adding heat at critical times during the self-assembly, time scales for solvent vapor enhanced self-assembly could be reduced from hours to seconds making the prospects for this technology to become industrially applicable more promising.

Thesis Supervisor: Caroline A. Ross
Title: Toyota Professor of Materials Science and Engineering

Acknowledgments

I would like to start off by apologizing to anyone that I fail to acknowledge. I know that a man is not an island unto himself; but rather, he is affected in some way by every person he ever interacts with. I have been very fortunate to be able to grow and mature in a surrounding where the people and communities have had a great and positive influence on me. I hope that in my life I will be able to continue the work of passing on these received gifts for the next generations to come.

I would like to thank my parents for raising me in a loving and caring household where values such as compassion, self-sacrifice, faith, and hard work were instilled in me. I would like to thank my siblings for being such great companions, and I look forward to what the future brings. I would like to thank the community of educators in my hometown of Gretna, NE where I spent twelve years learning how to learn. I would like to thank my grandmother for putting up with me during my first two years at the University of Wisconsin and my relatives there for the early morning transportation on game days (Renee, Don, and Patti!). I would also like to thank the UW for providing an opportunity to explore my research interests almost immediately when I arrived there in 2003, and I would like to thank my mentors there: Prof. Rob Carpick, Prof. Hal Evenson, Prof. Franz Himpsel, Prof. Wendy Crone and Dr. Hongquan Jiang. I would like to thank those involved in helping me have successful study abroad opportunities in Germany: Mary Bird, Dr. Tom Thersleff, and the staff from DAAD's RISE program.

I would like to thank my advisor, Prof. Caroline Ross for all of her guidance throughout my thesis; without which, my time would not have been nearly as enjoyable. I would like to thank all of the support staff who have been invaluable with helping me find solutions to my problems: David Bono, Mike Tarkanian, James Daley, Mark Mondol, and Dr. Shiahn Chen. I would like to thank some of my many mentors at MIT: Prof. Karl Berggren, Prof. Jeff Grossman, and Prof. Michael Demkowicz. I would like to thank the many friends and acquaintances that I met while at MIT and especially those with whom I worked with on various projects. I would like to thank the undergraduates of Conner4 who I was able to meet and mentor during my time as a graduate resident tutor - I couldn't have found a more pleasing place to reside. I would like to thank my daughter Felicity (and now Eleanor!). I know she won't remember living here, but it brought joy to my day when I would come home to a squealing one and a half year-old excited to see 'daddo.' And lastly, I would like to thank my best friend and loving wife Susan. She made every day a joy.

Contents

List of Figures

List of Tables

Chapter 1

Introduction and Motivation

1.1 Motivation and Outline of Thesis

The invention of the electronic transistor heralded dramatic changes to the way that humans interact with the natural world. As researchers discovered new methods to shrink the size of transistors in a systematic way (following the well-known Moore's Law) computer systems have gotten more and more powerful enabling humans to have access to tools that would be thought of as unthinkable a century ago. Today, many carry in their pocket devices as powerful as the supercomputers of decades ago which filled large rooms.

In general, transistors and how they are used as arrangements allowing for logical computation has remained unchanged. What has changed is their size. Smaller transistors yields ever increasing computational ability for a given unit area and also generally allows for more computation completed per unit energy input. The ability to make smaller and smaller patterns for the wires and junctions making up the transistors and their layout has been led by advancements in optical lithography.

Patterning transistors with photons is diffraction limited. The resolution, R, or the spacing between two neighboring sufficiently distinguishable intensity peaks for a light source with a wavelength, λ, is given by the well-known $R = \frac{\lambda}{2\mathrm{NA}}$, where NA is the numerical aperture which corresponds to the range of angles over which a system can accept light (θ degrees from the source, traveling through a medium with index of

refraction n) and is defined numerically as $n\sin(\theta)$. Currently, the wavelength of light used in industry to pattern computer chips is 193 nm and may remain so for some time even though historically the easiest way to shrink pattern sizes and decrease the resolution limit was to use shorter wavelengths. Instead, advancements have come in clever ways to use this wavelength to make increasingly smaller patterns. For example, immersion lithography (193i) changes the medium that light travels through from air, with n of 1, to higher index fluids which increase NA and therefore decreases the resolution to smaller periodicities available to pattern. These strategies have allowed 193 nm light (in conjunction with other strategies) to result in modern computer chips that have approximately 20 nm half-pitch features.

Extreme ultraviolet lithography (EUV) aims to improve the resolution limit by using smaller wavelength light (13.5 nm), but it currently is encountering a host of technological challenges that are preventing it from being used even though billions of dollars have been spent on developing the technology. One technological hurdle is that no light source has been developed that meets the stringent requirements of stability and intensity needed to pattern quickly and effectively enough for industry.

Electron beam lithography is an available technology that can pattern features much smaller than 193i (owing in part to the sub-nm wavelength of electrons) but it also runs into profitability issue due to the serial nature of the patterning, where a beam of electrons is scanned line by line over in an entire area for patterning when compared to optical lithography, where the entire area is flashed and exposed for patterning simultaneously. No one is entirely certain which technology is going to end up providing the ability to pattern smaller features sizes beyond 193i, and this is where self-assembly comes into the picture.

Nature uses self-assembly all around us. The complexities of the human body are encoded within DNA which has a much higher information storage density than anything that humans can currently produce and which allows for the self-assembly of complex structures with sufficient material and energy input. All of this is done taking by advantage of thermodynamic principles which guide all processes. If humans can become adept in controlling self-assembly, then technological advancements will

continue at a rapid pace.

The basic concept for utilizing thermodynamic self-assembly to improve the resolution limit of computer chips is to combine two approaches: First, use available technology to produce patterned regions that act as macro-scale boundary conditions on the order of 10s of nm's in dimension. Then, fill these regions with molecules that are mobile and thermodynamically driven to self-assemble and arrange themselves into chemically distinct patterns with periodicities much smaller than the macro scale boundary conditions where were initially set. For example, use optical lithography two create a trench 100 nm in width and then fill the trench with molecules that lineup in and along the trench direction and which space themselves with 10 nm periodicities. After etching away one of the chemically distinct regions of these molecules, trenches with periodicities of 5 nm's have been produced. Self-assembly has the advantage, like optical lithography, of being a parallel process. No matter where the molecules are located, they will all have thermodynamic driving forces guiding them to arrange themselves locally. Self-assembly is not completely understood though and it can be fraught with difficulties, so being able to control the thermodynamic driving forces is an important problem to tackle. This thesis aimed to understand and improve upon the current methods for controlling these driving forces, whether through placement of physical boundary conditions or by environmental control by introduction of solvent vapor and/or heat.

This chapter introduces one class of self-assembling systems known as block copolymers and introduces annealing methods which help them equilibrate into periodic patterns. Block copolymer self-assembly is one of the competing strategies for producing high-resolution patterns over a large area. Numerical modeling techniques, in particular self-consistent mean field theory, is briefly introduced and discussed. Results from this modeling method are compared to experimental results throughout this thesis.

Chapter 2 explains detailed experimental setups of the basic solvent vapor annealing system, the flow controlled solvent vapor annealing system, and the solvothermal annealing system which were used in this thesis. Enough detail is listed such that

anyone wishing to reconstruct these systems should have enough information to do so. Also explored is the effect that powerful mobile computational devices, such as tablet computers, are starting to have on how research is done in an academic lab setting.

Chapter 3 explores the block copolymer materials system used and the basic solvent vapor annealing methodology which can enable a wide range of control during the self-assembly such as microphase morphology and orientational control which can enable higher aspect ratio perpendicular features. The importance of controlling solvent removal rate is noted here.

Chapter 4 discusses the flow controlled solvent vapor annealing system which was constructed during this thesis work to expand upon the capabilities of the basic solvent vapor annealing system and which allows for a higher degree of control and reproducibility. The important differences between this method and the basic solvent vapor annealing method, such as the ability to accurately probe lower vapor pressures and enable the self-assembly of lower molecular weight block copolymers, is covered.

Chapter 5 summarizes templated self-assembly which combines electron beam lithography, a top-down technique, with block copolymer self-assembly, a bottom-up technique, to enable a wide range of lithography strategies such as three-dimensional self-assembly. Using templated self-assembly with removable materials and the importance of the chemical functionalization of the templated boundary conditions is discussed.

Chapter 6 shows how the introduction of heat during a solvent vapor anneal can drastically shortened the time scales of annealing to make this technique more industrially viable. This method of solvothermal annealing is explored with templated systems and is shown to be capable of annealing regions of interest within minutes of exposure to the proper sequence of solvent vapor and heat. Drastically reducing the time scales of annealing makes self-assembly an attractive candidate for next generation lithography.

1.2 Introduction to Block Copolymers

Block copolymers (BCP) are of interest for lithographic applications due to their ability to generate patterns with periods ranging from 5 to 100 nm[3–9]. This range overlaps with and exceeds that which is currently achievable with conventional photolithography processes. By harnessing the self-assembly inherent in this process, this technology enables a cost-effective, high-resolution, and high-throughput nano-patterning capability, especially when combined with current nano patterning techniques such as electron beam lithography and nano imprint lithography. This bottom-up approach to patterning surfaces is still some years away from being implemented in industry, with the current ITRS report still considering it an emerging technology. Looking forward there are still many obstacles to overcome such as reproducibility, precision morphology control, and defect control of the BCPs if this technology is to be used on an industrial scale. Templated self-assembly (industrially known as DSA or directed self-assembly) and precision solvent annealing is of increasing interest in accomplishing these goals and expanding the domain of application of this technology. The ability to selectively swell different components in BCPs can induce varying degrees of changes from the bulk morphology commonly seen, and this is currently only possible through the use of solvent annealing.

Diblock copolymers, or AB block copolymers, are two chemically distinct polymer chains connected together in a linear fashion with a covalent bond[10]. Due to their differing chemistry, the blocks of the BCP tend to be immiscible and undergo phase segregation at temperatures below their order-disorder transition temperature. Macro scale phase segregation is prevented by the presence of the covalent bond linking the two immiscible polymers; hence the separation distance, D, is limited to sizes on the order of the radius of gyration, R_g, of the polymer chains (10s of nm): $D \sim R_g \sim aN^{\frac{1}{2}}$, where a is the monomer length, and $N = N_A + N_B$ is the degree of polymerization which is approximately the number of monomer units. In bulk, the self-assembly of block copolymer morphology (lamella, cylinders, etc.) is determined by the volume fraction of the blocks, f, the degree of polymerization, and the degree with which the

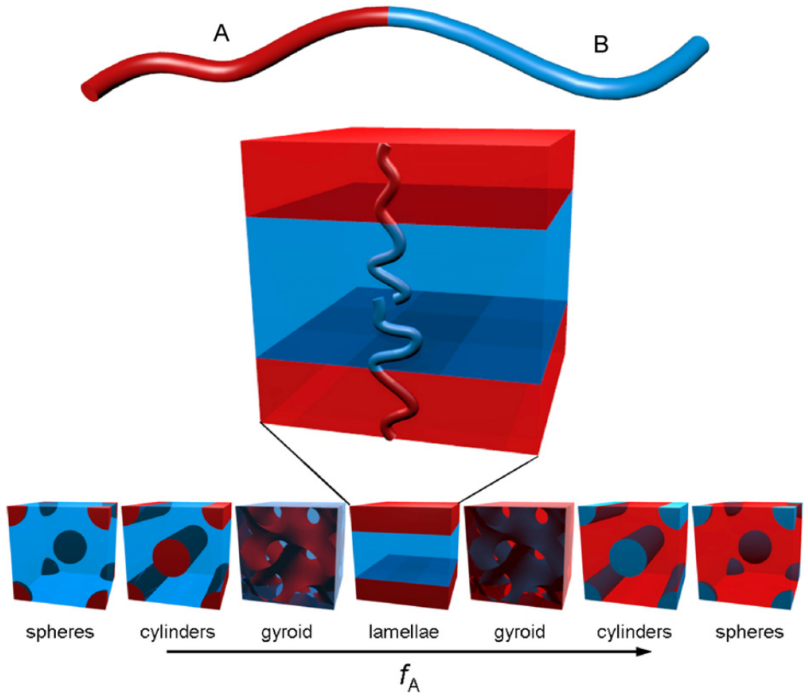

Figure 1-1: A schematic of the some of the morphologies obtainable with BCPs[1].

two blocks are immiscible, which we designate quantitatively with the segmental Flory-Huggins interaction parameter, χ_{AB}, which is inversely proportional to temperature. In thin films, the available morphologies are in and out-of-plane cylinders and lamella, perforated lamella, and spheres. Bulk morphologies are seen in Figure 1.2.

One simple but powerful thermodynamic approach to understanding the driving forces that cause spontaneous microphase separation is the Flory-Huggins model, which gives a Gibbs free energy of mixing equation

$$\frac{\Delta G_{mix}}{kT} = \frac{f_A}{N_A}\ln(f_A) + \frac{f_B}{N_B}\ln(f_B) + f_A f_B \chi$$

where f is the volume fraction and N is the number of repeat units of each polymer type.

The change in Gibbs free energy, ΔG_{mix}, is related to the total entropy change of the universe which must be > 0 for a spontaneous process to follow the 2nd law of thermodynamics. When ΔG_{mix} is < 0, the entropy of the universe would increase if the process was allowed proceed uninterrupted. When considering the functional

form of this equation it is important to realize that it is describing a simplification of the actual BCP system. The first two terms describe the well known configurational entropy terms. I.e. the maximum configurational entropy would occur in a BCP system if the monomers making up the polymers were randomly mixed. There are other entropy terms that are not explicitly shown in this equation. For example, consider the conformational entropy of a polymer chain segment concerning itself with how two neighboring monomers are rotated relative to each other (assuming that these two neighboring monomers have single bonds and are capable of rotation). If there are many states, W, that are available for these two neighboring monomers to be in relative to each other, then their conformational entropy is high. This is noted by considering the well known Boltzmann entropy formula, $S = k\ln(W)$. This picture helps intuit how spontaneous processes that seemingly increase the 'order' of a system are not in fact breaking any laws of thermodynamics. A good example of this is the case of oil and water spontaneously separating. Although it may seem like the entropy is decreasing when two materials systems are separated; in fact, the configurational entropy is decreasing, but it is being more than compensated for by the increase in conformational entropy that results when water molecules go to one region of the cup and oil molecules go to another: water molecules can hinder rotational conformations of the long oil molecules. If water segregates, oil molecules can access more conformations and increase the total entropy of the system.

There are a wide range of entropic components that can describe very deep details of the system (even electronic configurations within neighboring bonds have entropic components) making it difficult to keep track of every interaction possible. That is why the Flory-Huggins model of BCP mixtures takes the route of wrapping all of these other terms into an 'energetic' penalty term χ. Now, instead of dealing with the complexity of how a water molecule is hindering bond rotations from steric interactions, etc., we can simply say that there is an energetic or enthalpic penalty to ΔG_{mix} proportional to how many water molecules are located near oil molecules $(f_A f_B)$.

This picture helps explain why order disorder transitions within a BCP system

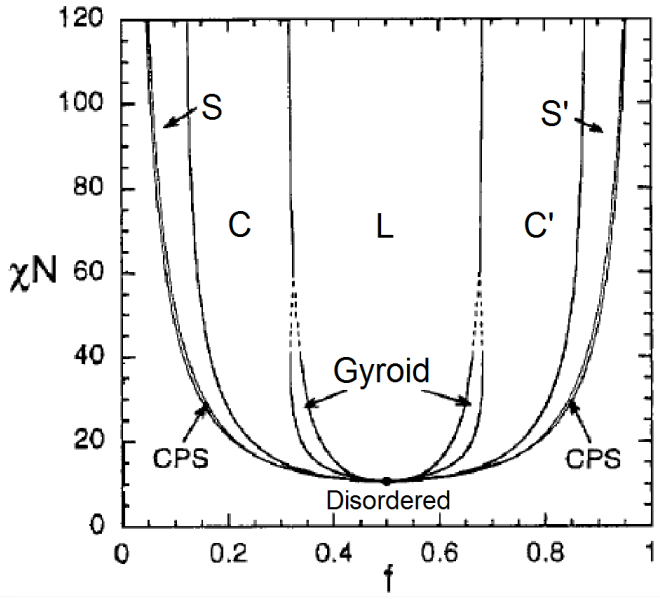

Figure 1-2: A phase diagram of diblock copolymers predicted with self-consistent mean field theory[2]

can arise. If the BCPs are sufficiently small (N is small), then there are fewer constraints for example on rotational configurations due to there being fewer monomer bonds in general and thus fewer segments of consideration. This starts making the configurational entropy term of more and more important unless χ is very large to counteract this. This interplay between χ and N are why they are usually considered as a multiplicative pair χN. If χN is too low (< 10.5 for bulk systems where $f = 0.5$) a BCP system is unable to spontaneously phase separate as doing so would break the second law of thermodynamics. The bluk di-BCP phase behavior relating χN and f is shown in Figure 1.2. As χN decreases (for example, by increasing temperature) the polymer system may go through an order disorder transition and become a homogenous melt.

Although the bulk phase diagram shown in Figure 1.2 appears ordered and symmetric, in real systems this is not the case. Asymmetries can arise in real systems due to differing properties of the two blocks (in reality there is no B block that is the exact opposite of an A block in a mathematical sense). Additionally, constraints come about when the system is confined to thin films as opposed to the bulk systems that

were modeled numerically to determine the phase diagram.

Lastly, it is important to mention that for lithographic applications, BCPs are not used in bulk, but as thin films. When BCPs are confined to thin films, the surface energetics start taking up a larger fraction of the systems energetic consideration and can result in different phase behaviors that are explored throughout this thesis. A thin film of a given thickness, t, will, after annealing, contain periodic BCP microphase separated structures with a domain spacing of L_0. To compete with the cutting edge of optical lithography methods, BCPs with domain spacings of <50 nm periodicities are most important (although outside of the narrow field of BCPs for semiconductor lithographic applications, there are a wide range of applications for BCPs with larger periodics for a variety of applications related to filtration, photonics, etc. that were not explored in this thesis work).

1.3 Annealing Methods

1.3.1 Thermal Annealing

In order to make equilibrium morphologies that are stable at room temperature, it is desirable that the majority block have a glass transition temperature, T_g, that is greater than the temperature at which further processing of the BCPs will commence. There are many methods used in applying thin films of BCPs to surfaces such as spin/dip/spray coating, reel to reel, etc., and each of these methods will require some post processing/annealing to initiate microphase separation. If defects in the microdomain order are undesirable, then it is necessary to anneal the defects away by allowing kinetically trapped polymers to diffuse towards a state of lower energy. Thermal annealing does this by raising the temperature of the system near T_g and allowing the individual kinetically constrained chains to start reptating and diffusing. An activated reptation model for the diffusion coefficient, D, of a BCP undergoing Rouse dynamics is

$$D = D_0 e^{-\frac{\Delta \mathrm{F}}{\mathrm{kT}}}$$

D_0 depends strongly on the degree of polymerization, and ΔF is a thermodynamic energy barrier that is proportional to χN. A value of χN $\sim$ 7.6 is an estimate of when a BCP first undergoes significant difficulty in diffusion[11], this value is below the critical χN = 10.5 for microphase separation in lamellar diblock copolymer systems.

Although thermal annealing has been shown to be very effective in removing defects, thermal budgets should ideally be minimized when considering implementation of these technologies on industrial scales. Additionally, if changing periodicity is desired, the control over how much the individual blocks are changing in their volume fraction is negligible. If a process requires that a certain BCP materials system is used, then in order to achieve changes in BCP pitch and morphology entirely new molecular weights of the polymers must be synthesized in order to change. This can be seen by considering how the period, L_0, in the strong segregation regime scales as

$$L_0 \sim aN^{\frac{2}{3}}\chi^{\frac{1}{6}}$$

where a is the Kuhn monomer length.

L_0 does show weak dependence on χ, but this is not sufficient to realize significant changes in L_0 due to the subsequent cooling which will bring the interaction parameter back to its nominal value. Thermal annealing is effective in removing defects in microdomain order. Solvent annealing, on the other hand, also removes defects in addition to offering greater flexibility in BCP pitch and morphology by allowing solvent molecules to incorporate into the block copolymers and act temporarily as surrogate members of the self-assembling system that can effectively change χ and N.

Thermal annealing increases the temperature to bring the system closer to T_g, but it is also possible to decrease T_g by incorporation of solvents molecules into polymer networks, which changes interfacial interaction between the blocks of the BCP and their chain mobility by acting as a plasticizer. The effective strength of the initial Flory-Huggins interaction parameter changes depending on the fraction, f, of solvent incorporated into the polymer film as

$$\chi_{AB,\text{eff}} = \chi_{AB,\text{init}}\left(1 - f_{\text{solvent}}\right)$$

It is evident that decreasing T_g and χ serve well to allow the polymer to reach an equilibrium state without increasing temperatures, and there is the added benefit that solvents can selectively swell different blocks of the polymer effectively changing the volume fraction of the blocks allowing for varying degrees of morphology control. The amount that individual blocks swell depends upon the interaction parameter between the solvent molecule and the block in question. The Flory-Huggins equation can relate how a thin film of homopolymer (one of the blocks for example) swells depending on the vapor pressure, p, and the interaction parameter[12].

$$\ln\left(\frac{p}{p_0}\right) = \chi_{\text{solvent}-\text{polymer}}\left(\frac{D_0}{D}\right)^2 + \ln\left(1-\frac{D_0}{D}\right) + \left(1-\frac{1}{N}\right)\left(\frac{D_0}{D}\right)$$

1.3.2 Solvent Vapor Annealing (SVA)

Solvent annealing has proven to be a powerful technique for allowing thin films of BCPs to obtain different equilibrium structures with low defect concentration. Previously studies in our group have shown a wide range of morphology control using polystyrene-block-polydimethylsiloxane (PS-b-PDMS), and this system has shown to be quite interesting for a number of reasons. For one, the high Si content in PDMS leaves a robust oxide-like etch mask after a two step reactive ion etch (RIE), and the χ parameter of PS-b-PDMS (χ is approximately 0.26 at 300K) is quite larger than those of other commonly used BCP systems such as polystyrene-block-poly(methyl methacrylate) (PS-PMMA, χ is approximately 0.06 at 300K) and polystyrene-block-polyethylene oxide (PS-PEO, χ is approximately 0.08 at 300K). The higher value of χ allows for smaller values of N (smaller features) to be achieved without the BCP becoming disordered at room temperature. The cosolvent system used for annealing PS-b-PDMS consists of toluene and heptane (heptane is very selective to swelling PDMS, and toluene is moderately selective to PS and PDMS). Initial studies involved 45 kg/mol PS-b-PDMS (f_{PDMS}=0.32), which forms cylinders in bulk. By changing the vapor pressure of toluene and heptane, different morphologies could be obtained[13].

Experimentally, this was done by placing a spin-cast BCP film on top of a small glass pedestal inside of a larger crystallization dish. Then, a 1 - 2 ml of solvent (with

varying mole fractions of toluene) were added to the dish, and after placing a glass cover over the setup, the solvent is allowed to evaporate and the BCP film is allowed to anneal. The glass top does allow for a constant flux of solvent to escape and was required so that the polymer does not swell too much and dewet (by keeping the partial pressures of the solvents down). The vapor pressures were controlled in magnitude by changing the amount of solvent added to the dish; the closer the BCP film was to the solvent the higher the vapor pressure. This simple setup showed success, but reproducibility and consistency was a problem for a number of reasons and these are discussed in detail Chapter 2 and consist for example of the vapor pressure being heavily dependent on size of leak gaps over time between dish and cover. These reasons, along with others, necessitated that a system be built more capable of accurately controlling the vapor pressures of the solvents while allowing *in situ* monitoring to help give us insight into the swelling behavior of the BCP films. This system is discussed in Chapter 4.

1.4 Templated Self-Assembly

The pressing question at hand is how these patterns which result from intermolecular attractive and repulsive forces can be effectively harnessed to generate useful features with low defect density and reasonable annealing times. One way that researchers are attempting to generate useful features with BCPs is by templating the regions of interest with lithographically controlled chemical[3,14,15] or physical patterns[9,16–26]. The basic strategy revolves around combining top-down lithographic techniques such as optical and electron beam lithography with self-assembly. This takes advantage of the control of the top-down technique and combines it with the resolution of the bottom-up self-assembly. The types of boundary conditions imposed by the top-down self-assembly vary but usually consist either of physical or chemical templating. In physical templating, the substrate topography is physically modified or altered in some way by for example etching into a Si wafer to create an array of trenches, or using trenches resulting from a developed resist as guides for a self-assembling BCP.

After the BCP is added to the trenches, the chemistry of the side walls of the trenches should be such that they are more favorable to be wet by one of the blocks. This allows a domain ordering front to form along the side walls of the trench, which is where the BCPs will initially wet to minimize surface energy of the entire system in an analogous manner to a droplet of fluid wetting a corner to satisfy capillary forces. After sufficient annealing, the BCP domains will have arranged themselves along the trenches that could be linear or curved. In-plane cylinders for example tend to align with the underlying topography due to the energy penalty that a cylinder undergoes when trying to conform to sharp bends causing distortion to the polymer chains[27]. Patterning to control the orientation of individual cylinders by use of posts of hydroxyl silsesquioxane (HSQ, also chemically functionalized) has been a recent breakthrough that takes advantage of HSQ cylinders being able to interact with in-plane cylinders and this method was used throughout this thesis work.

In chemical templating, the substrate surface is modified such that different chemical species occupy periodic locations along the sample. This can be accomplished for example by first chemically reacting a short chained hydroxy-terminated polymer with the native SiO_2 and then using top-down lithography methods to degrade or crosslink periodic regions within this 'brush' treated surface. Due to the periodic arrangement of regions with differing surface energy, the different blocks will tend to wet whichever region it is most compatible to. One advantage to this method is that it does not destruct the underlying hard or soft substrate in any way. One disadvantage though is that although the BCPs can appear to have simple patterns that correspond to the underlying surface chemistry, it is likely that the three dimensional nature of how exactly the BCP microdomains are orienting themselves can be complex and non-regular meaning that care has to be taken when pattern transferring since different regions between neighboring BCP microdomains may have different amounts of polymer to etch through[28].

These issues aside, many groups have shown great control of lamellar forming PS-b-PMMA by using extreme ultraviolet interference lithography or electron beam lithography to pattern dense lines and spaces with periods on the order of the block

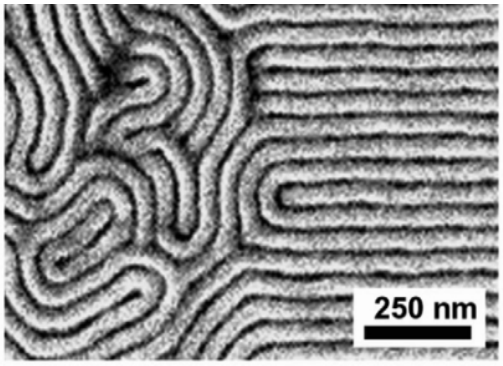

Figure 1-3: An SEM micrograph showing the transition of perpendicular lamellar PS-PMMA to a chemically patterned region that guides the self-assembly.[3]

copolymer period[5,7,8,24,29,29–35] as shown in Figure 1.4 where the chemical contrast that results from the photon beam oxidation of the photoresist caused lamella to align in the direction of the patterning, with each block of the lamellar BCP tending to minimize its free energy by wetting the patterned or unpatterned regions to minimize unfavorable substrate-polymer interactions. By changing the commensurability of the chemical pattern strain can be induced into the polymer resulting in changes in line width and periodicity until it becomes energetically unfavorable and defects start to form.

For making perpendicular lamellar lines, chemically patterned surfaces have been promising with the control they exhibit, however this technique does not allow for placement control of morphologies such as in-plane cylinders and spheres. Instead, physically templating substrates with changes in surface topography can be used to guide the formation of such patterns[9,27,33,36].

1.5 Modeling

BCPs consist of many components: PS-b-PDMS, with a molecular weight of around 45 kg/mol, is composed of $\sim$ 400 monomer units, with each monomer containing about 10 elements and being about 0.1 nm^3. A 20 nm spherical micelle has on the order of 42 000 monomers and involves 200 or so BCPs. If BCPs are to be modeled

with numerical simulations, then the ability to model realistically sized regions of 10's of nm's quickly becomes intractable if the positions and orientations of each element are kept track of along with their connectivity, as limitations are reached into how quickly a given calculation can update tens of millions of memory locations hundreds of thousands of times. These limitations led physicists to develop a wide variety of simulation techniques that effectively try to ignore these many small size scale effects and wrap them up into a smaller number of macroscopic effects that behave equivalently. This strategy is known as coarse graining. Coarse graining conceptually wraps up a number of neighboring monomer units and makes larger scale monomers that are connected together. Instead of a polymer being composed of hundreds of monomers, it is composed instead of tens of monomers each following a variety of rules that guide their relationships to their neighbors (spring constants replace calculated bonding energy versus distance using quantum dynamics, etc.). This strategy makes it possible with modern computers to model systems of many macroscopic chains over larger length scales by tracking every component in what is known as a molecular dynamics approach. Another approach used throughout this thesis is less computationally intensive than molecular dynamics and works by modeling the energetics of one coarse grained BCP in an effective mean field. This mean field approximates the averaged energetic contributions of the BCPs which would surround this coarse grained BCP, and this field behavior is actually calculated from the individual BCP. Effectively, this is a BCP interacting with an averaged-out surrounding of itself. The next section on this method, known as Self-Consistent Mean Field Theory (SCFT), goes over some of the basic math behind this method, and Mathematica code that can run such a simulation is included in the appendix of this thesis.

1.5.1 Self-Consistent Mean Field Theory

SCFT[37–41] has its foundations in statistical mechanics and involves the partition function, Z. Recall that the partition function is related to the probability that a given configuration of objects will occur. One way to intuit this is as follows: imagine

standing above a door-less room with a floor covered completely with red plastic cups of varying diameter. If a ball is thrown from a random location into the room, the probability that it lands in a given cup will be proportional to the diameter of the cup. Each cup could represent a given configuration of BCPs where each configuration has a certain energy value associated with it, and the size of the cup diameter was exponentially related to this energy value, which is expressed with an energy Hamiltonian, H. In this example, the partition function, Z, is the total added area of all the cups. Z encodes information about every cup (energetics of a given configuration $\rightarrow$ Boltzman probability of such a configuration $\rightarrow$ cup diameter), and therefore it turns out to be a valuable mathematical tool for thermodynamics. Z is written as a function of H; and in SCFT, H is a function of the averaged 'mean' field of the surrounding area outside of the given BCP. These are chemical potential fields, Ω. In a given region of space that is being simulated, at a given step in a simulation, a mean field will be tested, and there will be a field value associated with each coordinate in this space. Simply put, a field represents the a 4D object: three dimensions map out the coordinates, and the last dimension represents the field value at the location (this field value wraps up information about energetic penalties for overlapping polymers of different type for example). To find Z, the summation of each probability involves functional integration as follows:

$$Z = \int e^{-\frac{H[\Omega]}{\mathrm{kT}}} \mathrm{D}\Omega$$

The goal of an SCFT calculation is to find the mean field configuration, Ω^*, that dominates the partition function[38]. I.e. we want to find the largest diameter cup which represents what is most likely to happen statistically (and thus in nature). Mathematically speaking, the saddle point solution to SCFT is sought after. I.e. when the derivative of the energy with respect to the field configuration is zero. This represents a saddle point in this context which could be either a maximum, minimum, or a saddle point as typically described. This points to one disadvantage of SCFT worth mentioning, which is that meta-stable local minima can be found instead of global minima (maxima can be found, but SCFT has built in temperature-like fluctuations

of field values that drive the system out of them and into local, or more hopefully global, minima). The goal written mathematically is the functional derivative:

$$\left.\frac{\delta \mathrm{H}[\Omega]}{\delta \Omega}\right|_{\Omega^*} = 0$$

These are the two most important equations for SCFT in general. When moving to system specific cases, H has to be described specifically. For a diblock copolymer system, H will not be derived here, but typically the method of finding H starts with a standard Gaussian chain partition function follwed by a Hubbard-Strantovich transformation (a mathematical tool that makes solving later SCFT steps easier, this is actually the step where the fields are introduced to replace the coarse graining of the system around the BCP chain). This results for the case of AB diblock copolymers in:

$$H[\Omega] = -C\left\{i\int \Omega_+\left[\vec{r}\right]\, d\vec{r} - \tfrac{1}{\chi \mathrm{N}}\int \Omega_-^2\left[\vec{r}\right]\, d\vec{r} + V\sum\nolimits_n \ln Q_n[\Omega]\right\}$$

where Ω_+ is a chemical potential field (with only imaginary values, thus making H real) corresponding to 'pressures' in the system trying to keep the BCP density constant (this helps prevent polymer from overlapping in space and making densities unrealistically large). Ω_- is a chemical potential field corresponding to the energetic penalties of interactions. I.e. the different chains do not want to overlap and the amount of this dislike is related to the Flory-Huggins interaction parameter, χ. V is the system volume, C is a materials constant that includes for example the Ginzberg parameter, and Q_n is the single chain partition function for the nth species (AB diblock, homopolymer of B, solvent a, triblock ABA, etc.) which is calculated differently for each.

In general, each component in a given species (A and B for an AB diblock) has a corresponding field (in a similar way, in a given mixture of different components, each component has a chemical potential field associated with it which 'guides' its diffusion for example). For the case of an AB diblock, $\Omega_A = \mathrm{i}\Omega_+ + \Omega_-$ and $\Omega_B = \mathrm{i}\Omega_+ - \Omega_-$. Q_n can be found by utilizing different mathematical tools to help solve for the single chain partition propagator q_n from a modified diffusion equation using the pseudo-spectral algorithm and then summing over q_n for each chain. Q_n is then

Table 1.1: The collection of diffusion equations to solve for the propagator q_n which helps solve for the single chain partition function needed for SCFT.

$\frac{\partial q_n}{\partial s} = \frac{a^2}{6}\nabla^2 q_n - \Omega\left[\overrightarrow{\phi}_n\right] q_n$	$\frac{\partial q_n^\dagger}{\partial s} = \frac{a^2}{6}\nabla^2 q_n^\dagger - \Omega\left[\overrightarrow{\phi}_n\right] q_n^\dagger$
$q_n = q_n\left[\overrightarrow{r}, s, \Omega\right]$	$q_n^\dagger = q_n^\dagger\left[\overrightarrow{r}, s, \Omega\right]$
$q_n\left[\overrightarrow{r}, s = 0, \Omega\right] = 1$	$q_n^\dagger\left[\overrightarrow{r}, s = 0, \Omega\right] = 1$

$$Q_n[\Omega] = \frac{1}{V}\int q_n\left[\overrightarrow{r}, s = 1, \Omega\right] d\overrightarrow{r}$$

where s is the position along the chain. (I.e. each chain has a number of monomers, N_s, and each monomer starting from the beginning of the chain(position s=0) is indexed with the last one being represented by position s=1). The equations solved to find the propagator are shown in Table 1.1, where a is the Kuhn monomer (related closely to the size of the physical polymer system's monomer diameter) and $q_n^\dagger$ is the complimentary propagator that starts at the opposite chain end. q_n is closely analogous to the wave function in quantum mechanics: Consider a line of length one ($s \in [0, 1]$). For an AB diblock copolymers, q_n can be thought of as a wave function representing a probability distribution of how the A block is distributed and $q_n^\dagger$ representing how the B block is distributed along the chain. Initially in the simulation, the probabilities are unity at each end (Dirac delta function, as in the last row of Table 1.1), but as time steps go on, the probability amplitude spreads out. This is why the Fokker-Planck equation (first row of Table 1.1) is used; it describes the time evolution of a probability density function. As each of the probability distributions evolve and start overlapping, the overlap has an interaction penalty as expected due to the χ parameter.

After $q_n^\dagger$ and q_n are solved, the normalized local polymer density, ϕ_n can be calculated from:

$$\phi_n\left[\overrightarrow{r}\right] = \frac{\rho_n\left[\overrightarrow{r}\right]}{\rho_0} = \frac{1}{Q_n}\int_0^1 q_n^\dagger\left[\overrightarrow{r}, 1-s, \Omega\right] q_n\left[\overrightarrow{r}, s, \Omega\right] ds$$

This is analogous to solving for $\psi^*\psi$ in quantum dynamics calculations, where ρ_0 is the monomer density and ρ_n is the local polymer density. In the special case of a single monomer species, such as a solvent of type N (N could be solvent a, b, etc.), Q_{SolN} is

$$Q_{\mathrm{SolN}} = \int e^{\Omega_{\mathrm{SolN}}\left[\vec{r}\right]} d\vec{r}$$

and the normalized density of solvent is

$$\phi_{\mathrm{SolN}}\left[\vec{r}\right] = \frac{e^{\Omega_{\mathrm{SolN}}\left[\vec{r}\right]}}{Q_N}\nu_{\mathrm{SolN}}$$

where ν_{SolN} is a volume fraction of solvent.

As SCFT iterates through solutions, there must be conditions that are satisfied so that the system remains self-consistent. This is because as a solution to a given field is found, it may pull the solution of another field further from its equilibrium solution since they are all interconnected. Thus a 'relaxation' scheme is used to 'relax' the fields. These relaxation equations belong to the pseudo-dynamic complex Langevin dynamics scheme:

$$\frac{\delta \mathrm{H}}{\delta \mathrm{i}\Omega_+} = \lambda_+ \frac{\delta \mathrm{i}\Omega_+}{\delta \mathrm{t}} = \lambda_+ C\left(1 - \phi_A - \phi_B\right)$$

$$\frac{\delta \mathrm{H}}{\delta \Omega_-} = \lambda_- \frac{\delta \Omega_-}{\delta \mathrm{t}} = \lambda_- C\left(2\nu - 1 - \phi_B - \phi_A - \frac{2\Omega_-}{\chi \mathrm{N}}\right) + \lambda_- \eta\left[\vec{r}, t\right]$$

where λ_+ and λ_- are relaxation parameters, and t is a fictitious simulation time step unrelated to real time. The equations basically try to approximate how the energetics of a field configuration, H, evolve with the field configurations, and the approximation is made that this evolution is proportional to how the field evolves in t. If the time steps are too big, then the system can overshoot relaxed field configurations, but if the time step is too small, then the simulation can take too long to complete in a reasonable amount of time. Finding the values for these part of the Langevin relaxation scheme are done empirically. $\eta\left[\vec{r}, t\right]$ is random Gaussian noise used in the scheme to add effective 'temperature' fluctuations to help prevent the system from getting trapped in meta-stable equilibrium conditions[37].

Thus a simulation begins by starting with random field configurations, solving the diffusion equations for each propagator, finding the densities of the polymer related to the propagator, updating the fields with the relaxation scheme and iterating this until $\frac{\delta \mathrm{H}[\Omega]}{\delta \Omega}\Big|_{\Omega^*} = 0$ (although it wont be numerically equal to zero, as the random temperature fluctuations prevent this). Numerically, SCFT confines the polymer space to an N_x by N_y by N_z grid. Thus, the fields, densities, and propagators are 3D matricies of this size, where each coordinate in the matrix represents a physical coordinate in the unit cell being simulated (with periodic boundary conditions). The physical distance between two grid points in the 3D cell in relation the the actual polymer monomer size are related to L_0. Fixing field configurations for certain regions during the simulation effectively adds boundary conditions (like posts patterned for templated self-assembly)[42].

1.6 Summary

Due to the pressing need to create new technologies that take advantage of nanoscale features smaller that what is currently economically viable, much effort has been expended to understand BCP self-assembly which has shown itself to be a very promising candidate for this type of patterning. Researchers have usually dealt with annealing by using heat, but this methods has limitations as discussed. Thus, solvent vapor annealing has been found to be a very promising technique for the self-assembly of BCP systems. Unfortunately, much there is much complexity to a SVA that has yet to be completely understood. Researchers have found reproducibility to be a vexing problem that has resulted in a gradual understanding of the vast number of control variables required during a SVA (humidity, temperature, vapor composition, film thickness, etc.). The SVA methods used before I began my thesis worked revolved around very simple systems where a BCP film was simply placed in the neighborhood of an evaporating solvent at room temperature in an open or closed system for hours to days. The difficulties with this method are discussed in Chapter 2. This need for better control of SVA guided my work in designing a flow controlled SVA system whose setup

is described in Chapter 4. This work resulted in an improved understanding of the complex thermodynamic systems when a diblock copolymer is introduced to varying populations of two solvents by tracking *in situ* the behavior of the thin films during exposure to controlled solvent vapor conditions. This better understanding of the important characteristics required for a controlled SVA allowed for the development of solvothermal annealing which combines the best characteristics of SVA with those of thermal annealing in a non-linear fashion. Future work in this area should yeild much fruit in understanding of best-practice annealing methods and my current results show that it is possible to reduce time-scales of self-assembly to the minutes or seconds time scales making it very promising for industrial manufacturing where these timescales are required. The work presented here on templated self-assembly was possible due to the nature of controlled solvent vapor annealing. This is especially the case for the bilayer self-assembly, where magnificently complex levels of 3D self-assembly were found to be possible with SVA but not with thermal annealing. These results are discussed in Chapter 5. Enabling complex 3D self-assembly could result in drastic reductions to future nano-lithography whereby multiple patterning and planarization steps are instead replaced with single 3D self-assembly steps.

Chapter 2

Experimental Design and Methodology

2.1 Solvent Vapor Annealing Setups

The following section summarizes the key details that went into the construction of the solvent vapor annealing setup. This section contains enough information for anyone interested in creating such a system to do so by following the general outline presented here. Key differences between this system and the previous basic system used in our group are discussed.

The basic purpose of this device was to create a controlled solvent vapor atmosphere with set pressures of one or more solvents in a chamber that has uniform steady state vapor conditions wherein a polymer thin-film can be placed and exposed to the solvent vapors. The main difference between a system like this and the solvent vapor annealing setup that was used in the past in our group was that this system took advantage of steady-state vapor flows instead of more equilibrium like vapor conditions inside of a small partially closed container as discussed in the next section.

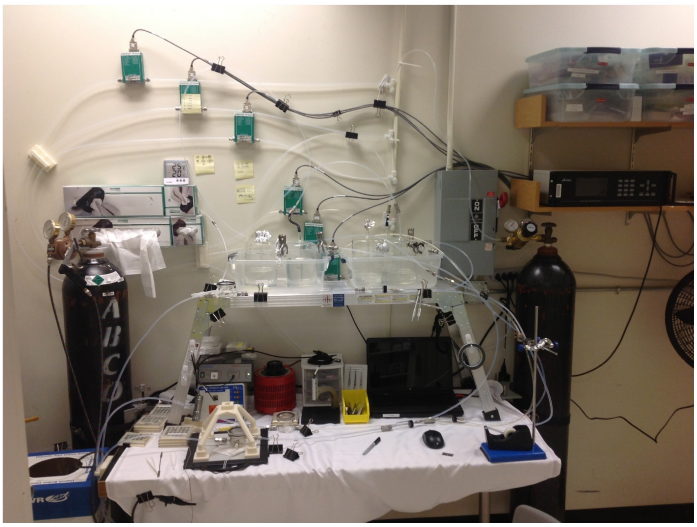

Figure 2-1: The flow controlled solvent vapor annealing system.

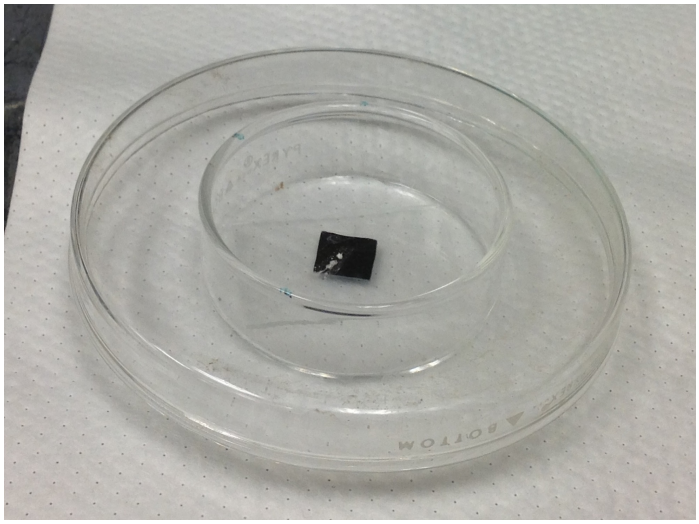

Figure 2-2: The previous setup used in creating a solvent vapor condition for annealing BCP's.

2.1.1 Basic Solvent Vapor Annealing

This basic solvent vapor annealing setup shown in Figure 2.1.1 consisted of the following: a crystallization dish, microscope slides, and a petri dish for the top cover. Typically three microscope slides were cleaved in half and stacked to make a pile of six inside of the crystallization dish. The experimental procedure was: first, a Si wafer with a polymer film was placed on top of the microscope slides. Then, an amount of solvent was added to the crystallization dish to reach a level almost as high as the sixth microscope slide. Then, the petri dish was added to the top to keep the solvent vapor relatively contained.

This was the setup used in annealing BCPs before I began my thesis work and was utilized for some experiments during my time here, but it had some disadvantages. Due to imperfections in the connectivity between the crystallization dish and the petri dish small gaps form where solvent vapor could leak out the top of the crystallization dish. Typically 1 to 2 mL of solvents were placed inside and the gaps resulted in a release rate of a few micrograms of solvent per second. Among other effects, this basically resulted in pressure conditions that were not entirely constant in time.

There are a few other important things to notes in this system before further discussion. The first was that do to the small volume of air above the polymer and solvent liquids, the chamber reached close to saturated vapor pressure conditions within only 1 - 3 minutes. Additionally, the distance from the solvent liquid air interface to the polymer air interface was initially very low. This in turn resulted in vapor conditions at the polymer air interface that would be very close to literature values of the solvent vapor pressures at the temperature conditions of this setup at room temperature. However, due to the gap at the top of the crystallization dish the solvent vapor pressures near the top would be lower than near the solvent liquid air interface and thus at the polymer surface since it resides in between the two regions. As time progressed during an anneal and the solvent liquid continued to evaporate, the distance between the polymer film and the solvent liquid air interface continued to increase. This increase resulted in a small decrease in vapor pressure conditions at the

surface of the polymer film. This effect could be measured by tracking the swelling conditions of the polymer film in real time during the anneal. Typically what happened was that the swelling ratio remained approximately constant until the solvent vapor was about to completely dry up, in which case the swelling ratio drastically decreased as the pressure conditions were decrease inside the chamber. This effect is explored in more detail in Chapter 3 where my work on achieving perpendicular BCP features was explored.

One of the disadvantages of this system is that due to nonuniformities in production of these glass pieces different solvent vapor conditions were achieved in different dish setups due to the different gap sizes that result from these two non-planar interfaces touching. I.e the size of the gap at the top of the glass dish resulted in differing vapor pressure conditions and thus different swelling ratio vs. time conditions. To mitigate these effects typically a single (glass dish+glass cap) system that was found to work was used for all relevant experiments and markings were drawn on top of the glass petri dish so that similar orientation between the two interfaces could be maintained between experiments on different days. This made it possible for a single researcher to reproduce successful experimental runs, but it made it too difficult for another researcher to use different glass pieces and have precisely the same results. These difficulties aside, it was possible to take advantage of knowledge of this behavior to achieve difference qualitative results by changing the gap size. For example, knowing that a given petri dish and crystallization dish setup would have a range of different gap sizes which could be explored by the rotation of each to relative to each other, three different vapor pressure conditions could you explored with the given dish. A high-pressure, high swelling ratio, low gap size regime, an intermediate regime, and a low pressure, low swelling ration, high gap size regime. This could be very simply accessed by rotating the petri dish relative to the crystallization dish and noting the three locations. The gap size was highest when the greatest amount mismatch between the two were noted by how much wobble could be felt in the petri dish when pressed against the crystallization dish and vice versa for the lowest gap size.

Another difficulty when using this glass dish system was that the experimental

steps had no 'atmosphere purging' step where ambient air condition were neutralized. Because the room temperature and humidity were typically not precisely controlled in these general lab settings, and because these variables can cycle greatly during weather changes in the region, different researchers found that different days, under what was assumes to be the same solvent vapor conditions, could actually result in completely different self-assembly. The reason for this was that water as a solvent can have a non-negligible effect on the swelling of the different domains in the BCP (depending in the particular BCP chemistry) and on the surface energies of the polymer-air (solvent A, solvent B, ..., H_2O, N_2, O_2, etc.) interface. Differing amounts of humidity changed the amounts of water presents in the system, and different temperatures of the system changed the vapor pressures achieved.

Another important difficulty to mention in this 'simple' system was the fact that solvents tended to adsorb to any surface inside the closed annealing dish. That meant that if a new, clean setup was used then different swelling ratios in the experiment could be observed because some amounts of the solvent molecules were going to adsorb onto all of the glass surfaces inside of the annealing chamber. Therefore, it was typically important to use the same setup with the same starting conditions. For example, only one solvent system (e.g. 5:1 by weight Toluene:Heptane) should be used in a given annealing dish, and if the solvent system was to be changed then the annealing dish should be cleaned and a dry run of the new solvents should be done with no polymer film inside and allowed to evaporate before the actual run was done. This helped create consistent chamber wall conditions between different annealing experiments on different days.

The question might arise as to why a completely closed system wasn't used, for example a system very similar except where the petri dish was replaced by a screw on cap that fixed in the solvent liquid. The reason was it was found that the solvent vapors in a closed system reached such a high vapor pressure for these particular polymers that the polymer films tended to dewet completely. This is because the driving force for any system that is mobile is a reduction in the free energy resulting from surfaces. A polymer film is always tending to form droplets(albeit usually on

Figure 2-3: N_2 was used as the carrier gas for the flow controlled solvent vapor annealing setup.

time scales beyond human time scales) because this reduces its surface area and thus its free energy. Therefore, by introducing gaps, the solvent system is never able to reach its absolutely highest possible vapor pressures and thus the amount of dewetting can be more fully controlled.

The difficulties presented in this 'simple' system made the system not quite simple and not quite reproducible or satisfactory enough for our goals. Thus it was necessary to build a setup that could mitigate some of these disadvantages that were present, and expand on the limitations.

2.1.2 Flow Controlled Solvent Vapor Annealing

In order to work around the limitations of the simple system, where the solving vapor conditions were constantly changing, it was necessary to move to a system where steady-state solvents vapor conditions could be obtained. Such a system would require a carrier gas, a source of solvents, and an annealing chamber separate from the solvent source. This was the general framework under which the construction of the system was guided.

A standard high purity (99.999%) N_2 tank was used as the source of the carrier gas. The pressure regulator was set to be less than 30 PSI due to the requirements of the mass flow controllers. Typically this did not need to be adjusted. Additionally, the pressure regulator had a Swagelok (316PST) fitting that connected it to 1/4 in. outer diameter perfluorinated tubing.

The perfluorinated tubing from the N_2 container reached a series of five T-junctions

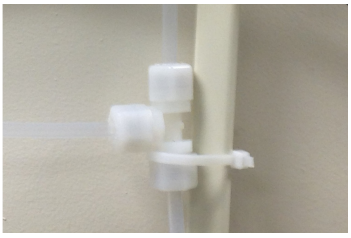

Figure 2-4: Nylon T junctions used to separate the carrier gas flow between a number of mass flow controllers.

Figure 2-5: Mass flow controllers were used to regulate the mass/volumetric flow rate of the carrier gas before it was sent to the solvent sources.

(durable white nylon compression tube fitting, Tee for 1/4 in. tube OD, McMaster 50775K395) in the setup. Metallic junctions were not needed in this case due to the lower pressures that were required for the mass flow controllers, this allowed for the use of nylon T-junctions (with a lower maximum pressure of operation) as a cost-saving measure.

Each nylon T-junction, except for the last in the series, was connected to one mass flow controller (MKS Type M100B Mass-Flo Controller). For more information on how these mass flow controllers operate see the appendix.

These mass flow controllers can have a wide range of flow rates available (0-50,000 sccm). However, each range of operation must be calibrated by the manufacturer and possibly altered by changing internal components such as the stacked disk bypass assembly which controls the amount of initial pressure drop internal to the device.

Additionally, each internal electronic feedback setup must be calibrated to the type of material that will travel through the device. Each of the mass flow controllers used in the system was calibrated to have a maximum flow rate of 10 sccm of N_2 gas.

There are a couple of important points to note as to why the mass flow controllers were placed before the solvent canisters instead of after. One reason was that because each flow controller required a specific calibration depending on the type of gas that would travel through it, it drastically increased the ease of operation and the flexibility of the solvent annealing setup to just stick with one highly calibrated gas flow of N_2. If for example we had calibrated the device for particular mixture of toluene and heptane gas, then whenever a new solvent system was used a new calibration routine would be required. One other very important reason as to why this was placed before the solvent source was that internal to the device were a number of plastic-based seals. It was possible to find and purchase a number of different brands and plastic type of seals that were resistant to a certain set of solvents, however changing these depending on the solvent system of interest would hinder the ease of use and could dramatically increase the cost of operation because each MFC is $>$ \$1k and seals can range from \$10-\$100.

In addition to this, by decreasing the number of times that an operator was required to manually handle the flow controllers, the amounts of drift in the zero set-point calibration could be decreased. Each controller had a number of mechanical moving parts internal to the device that controlled the flow rate and these parts were susceptible to drift in airflow calibration by vibrations and movements that could bring the device further from the original calibration.

By placing the flow controllers on the wall, vibrations could be reduced, and this reduction decreased the amount intervention required by operators in adjusting zero point calibration. This is not the only advantage though in placing the controllers here. One of the operational variables of a flow controller is the ambient temperature, and this is because part of the operation and feedback control requires the measurement of the temperature of the incoming gas. By connecting the controllers directly to the wall, which can be thought of as having a high thermal mass, and inertia against

Figure 2-6: The control box for the flow controllers which is capable of operating eight channels simultaneously.

temperature fluctuations in the room can be provided which further increases the operational accuracy of the flow controllers.

Each mass flow controller was connected to the 'MKS multi gas controller 647C'. This device provided a digital readout of the set points and real-time flow conditions of each of the six channels that were used. Numerical values from 0 10 sccm were entered directly into this device. An RS232 port is located in the back of this device and allows for connection to a computer via an 'RS-232 to USB' cable. This would allow for the possibility of more advanced 'flow control versus time' type of operation, however this was not used during the studies contained in this thesis, because typically steady-state operations were being observed for one hour, and the time delay between noticing a change in steady-state vapor pressure inside of the annealing chamber could be on the order of 30 minutes depending on flow rates, which was thought to be too long of a time delay to study novel changes in swelling ratio versus time.

Perfluorinated tubing (3/16 x 1/4 x 1/32, Thermo Scientific 8050-0250 Tubing 890 FEP) used to connect the mass flow controllers to the solvent source were found to be quite unyielding when trying to control their position and orientation due to their high stiffness. This tubing was required because, in terms of plastic tubing, it had the highest resistance to the solvents used in our study. It was important to choose a tubing material that was resistant to incorporating solvents that were going to be used, because any solvent incorporation in the tubing could create deviations in the vapor pressures expected, and improper tubing could allow the solvents to diffuse out of the tubing and create a health hazard.

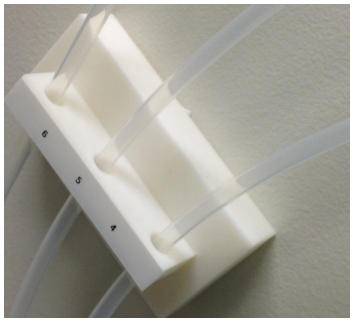

Figure 2-7: A 3-D printer was utilized to construct mounts to guide stiff perfluorinated tubing.

Figure 2-8: A glass chamber was used to contain the solvents. These pieces were custom-made.

The 3-D printer in the Laboratory for Engineering Materials was utilized many times throughout this thesis. It was found to be an excellent tool for creating extremely specific solid objects for laboratory use and rapid prototyping. I found the fastest and most simplest way to create an object for 3D printing was to use SketchUp (once owned by Google) and a plug-in that immediately created *.STL files. Many hours were saved by simply printing objects instead of using traditional machine shop methods where none were actually required (metal/wood vs. plastic), such as in the previous example of the tubing guide mounts.

The perfluorinated tubing connected the mass flow controllers to the solvent containers. These solvent containers, and all other custom glassware were custom

designed and made by glassblowers at G. Finkenbeiner Inc. The solvents container design had to satisfy a few requirements. Firstly, it was necessary that the container had a low probability of solvent leakage, because the solvent annealing setup was used outside of the fume hood. Thus, the container was designed with only two openings; an inlet for the carrier gas and an outlet for the saturated solvent vapor, where the outlet could also be used as the input for the solvent liquid itself. Secondly, it was desirable to have a fast and easy 'sanity check' where it would be immediately clear that the device was in operation. When the gas flow was on it was easy to see immediately that bubbles were being formed in the solvent liquid. This gave other lab users knowledge that the device was in operation for their safety considerations and immediately allowed the operator to check whether every component before the solvent container was properly operating (were there any loose fittings, was the N_2 tank empty, were there any breaks in the tubing, etc.). Thirdly, glass containers, even those custom-made, were more inexpensive then metal containers. Glass also has a higher thermal mass than metal, and can help stabilize temperatures of the solvent relative to the outside lab environment more readily than metal would be able to.

It can be enlightening to consider the path of a unit volume of N_2 carrier gas as it travels from the mass flow controller through the solvent liquid and out through the solvent container when considering the size of the solvent container to construct. As a N_2 bubble enters the solvent liquid it starts out as almost pure N_2. As the interfacial area between the N_2 bubble and the solvent liquid increases, the vapor pressure of the solvent in new bubble increases. By the time the bubble reaches the top surface and pops, ideally the bubble would be completely saturated with solvent. This was most likely not the case in this system due to the short path length (5-10 cm) of the traveling bubble, thus a large surface area of solvent liquid was desired. These solvent containers were approximately 13 cm in diameter, and given the high evaporation rates of the solvents that were used in this thesis, the size was sufficient for the creation of a saturated stream. (This was tested by comparing the swelling ratios of polymer films under a saturated flow and that of the simple system under equivalent solvent conditions.) One thing to note is that this analysis assumes a given

Figure 2-9: The ball and socket connection on the solvent container.

rate of introduction of N_2 bubbles. If the N_2 introduction rate was sufficiently high, it would be possible to have the exit gas flow have a negligible amount of solvent vapor and be far from the ideal conditions of the saturated solvent exit stream. This was one of the reasons that low volumetric flow rates between 0 - 10 sccm were used in this study. If faster rates are desired, then it would probably be be necessary to introduce heat into the solvent bath in order to increase evaporation rate. However, faster flow rates would also increase the pressures internal through the system as changes in cross-sectional area throughout the volumetric flow path would result in different flow rates and different pressures. A high flow rate would result in higher necessary pressures and would make some of the design choices much different. For example, in this system a simple ball and socket type of connection could be made on the glass chamber.

The low flow rates that were used in the system created total pressures internal to the system that were marginally above atmosphere pressure. This allowed for some simple and convenient connectors such as the ball and socket connector shown above. This allowed for the very quick release of the connecting pieces in order that solvents could be exchanged in and out of the container. The ball side has a 1.5 cm inner diameter hole and a 3 cm outer diameter. The socket is the standard complimenting piece and has an outlet of a 1/4 in. outer diameter glass tube about 3 cm in length. The clamp connecting the ball and socket was a type 'N28 INOX 18/8'. Also, the top of the solvent container was a 1/4 in. outer diameter glass tube. Again, taking advantage of the lower pressures inherent in the system, the tube from the flow controllers could

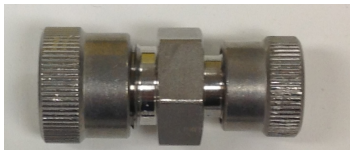

Figure 2-10: A Swagelok connector type that was used to connect each glass tubing to plastic tubing.

Figure 2-11: A diameter reduction of the saturated solvent vapor line was completed by using a 0.6 mm ID needle.

be heated and pressed around the outside to create a very tight fitting as shown in the glass chamber Figure 2.1.2.

To facilitate the connection between glass and plastic tubing, Swagelok connectors (SS4UT6400) were used. One end of this connector was able to permanently attached to the perfluorinated tubing, and the other side was able to be easily added and removed from the glass tubing. This was done by twisting action which tightened and loosened a small plastic O-ring around the outer diameter of the glass tubing.

To reiterate, the lower flow-rates used in the system were required in order that we could be more confident that a highly saturated stream of solvent vapor was leaving the solvent container. It was desirable though that the system had the capability to mix multiple solvents flows together simultaneously. We had first tried a simple T-junction type of connection that brought together multiple 1/4 in. perfluorinated tubing lines, however we noted experimentally that the results were not as reproducible as we had hoped. We found that the issue was most likely stemming from the fact that the velocity of exiting vapors from these larger diameter tubes was quite low, and that it quite was possible that neighboring gases that we were trying to mix together could diffuse up the neighboring lines. This would have made our assumption of a one-way stream invalid. In order to make better one-way gas streams, a diameter reduction strategy was introduced to take advantage of the Bernoulli effect where

Figure 2-12: A modified glass vial was used with a septum top to facilitate the mixing of multiple solvent streams.

lower cross-sectional travel areas under the same flux must result in higher velocity. These higher velocities were greater than the ambient diffusion rate of the different solvent streams, and gave us more confidence that different solvent streams were not contaminating each other. This diameter reduction was facilitated by the use of a luer lock attachment (Z118001, Perfektum Needle tubing connector male luer lock lock to tube) to the 1/4 in. OD perfluorinated tubing and a 20 gauge 30.5 cm long syringe (Deflected Point Septum Penetration Needles, Cadence Science, 20068590). This syringe had a nominal inner diameter of 0.6 mm, which a simple estimate based on the Bernoulli effect would suggest that the gas flow velocity was about one order of magnitude higher than in the plastic tubing.

The method of using syringes to mix different solvent streams also increased the ease of use of the device. This is because different streams could easily be added and removed through a PTFE septum which was resistant to the solvents used in the experiments. To produce this piece, G Finkenbeiner Inc. used a glass vial (Sigma Aldrich, 27379, 40 mL Clear Vial) that we provided and modified the glass to incorporate 3 cm of 1/4 in. OD glass tube. This could then be capped with readily available septa (Sigma Aldrich, 27022 PTFE/Silicone Septum), which would be replaced occasionally after multiple punctures. It is worth noting that this was where streams containing just N_2 were added in addition to the solvent streams in order to effectively lower the steady-state vapor pressures in the solvent annealing chambers. A typical experiment involved a stream of toluene, heptane, and N_2 each

Figure 2-13: The flow controlled solvent vapor annealing chamber.

with different flow rates.

After different streams were mixed together, they entered the solvent annealing chamber. The length of the tubing between each of the different Swagelok connectors was 0.5 m. This chamber was custom-designed and the glass piece was built by G Finkenbeiner. Glass was chosen to increase the visibility of the changes that the polymer film would undergo and to provide some thermal stability to temperature fluctuations in the room. The basic design consisted of a gas inlet port, a gas outlet port, and a loading port on top that gave one access to placing samples inside the chamber which was 5 cm in height. The loading port was fitted with a groove that allowed for a 2.5 in. nominal diameter solvent resistant plastic O-ring. It was (unfortunately) necessary to use plastic O-rings in this setup, because it was necessary to use a flat top type of closing piece (as opposed to simply having some sort of ball and socket type of clamp connection to close the chamber). A flat top was necessary because of the spectral reflectometer that made in-situ measurements of polymer film thicknesses through the top of the chamber. Having a large flat top allowed for the solvents chamber to be moved so that the reflectometer measurement spot could be moved between as many as six different samples inside the chamber during one experimental run. Although it was desirable to limit as much as possible the amount of plastic/rubber that were exposed to the different solvent vapor streams, we were able to find a custom o-ring (Marco Rubber, V1000331, 2-331 FKM (Viton) O-Ring

Figure 2-14: The solvent vapor annealing chamber underneath the spectral reflectometer which allowed for *in situ* film thickness measurements.

75D Black) specifically resistance to swelling in the presence of the solvents toluene and heptane. Pressure was applied to the quartz piece against the o-ring and solvent chamber by using clamps and was found to be high enough to not allow solvent to escape the chamber. Finally, the outlet port of the solvent chamber exited to the nearest fume hood.

All of the parts mention constituted the flow controlled solvent vapor annealing chamber which was used until a more recent upgrade was made where temperature control was intended. The following section describes in detail the alteration to the solvent vapor annealing chamber in order that Solvothermal annealing could be achieved.

2.1.3 Solvothermal Annealing

The key alteration was the insertion of a 0.5 in. ID port 0.75 in. from the base where a resistive heater could be inserted.

Figure 2-15: The glass chamber used for solvothermal annealing.

Figure 2-16: A silicon nitride hot surface igniter was used as the heating source for the solvothermal annealing.

The cantilever beam (Honeywell, Glowfly, Q3200U) that was placed inside the modified solvent annealing chamber acted as hot surface when a voltage was applied. When a voltage was applied and the resistor started heating, there was a hot spot located 0.5 cm from the tip of the cantilever, so this position was where samples were placed. The white colored ceramic outer piece was wrapped in PTFE thread sealant tape (MILSPEC T27730A) and pressed into the chamber port. The sealant tape was not completely stiff when the cantilever was placed into the chamber poor, and this allowed the cantilever beam to be adjusted while the system was closed. This was an important feature because it allowed for easy adjustment of the relative angle between the plane of the sample and the plane of the lens of reflectometer, which had to be minimized in order to get accurate film thickness measurements.

More details on the temperature response that the heating element would undergo under different voltages can be found in later in this chapter. Typically, ranges under 20 V were found to be the most useful in the solvothermal anneal. Before doing any solvothermal annealing, it was important to do safety testing first and find the conditions where, in the worst case scenario where O_2 was allowed inside the chamber with the solvents, one could find the temperature at which there was autoignition of the solvents. For the toluene and heptane solvent system that was explored in this

Figure 2-17: A variable voltage regulator was used to alter the AC voltage applied to the heating element.

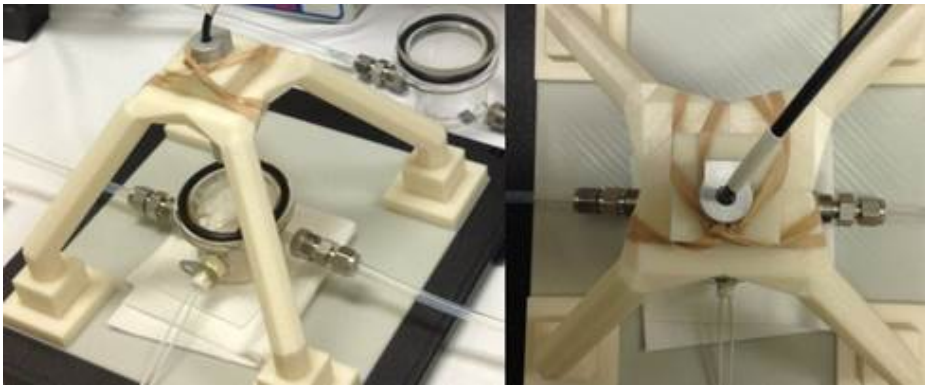

Figure 2-18: The operational setup (sans the quartz top) of the solvothermo annealing chamber.

thesis, autoignition occurred above 60 V or 800 °C. Note that this was higher than literature values for autoignition, because those testing conditions had a much more highly controlled environment of the constituent gases (solvents, O_2 and N_2, etc.).

Because the sample was raised while placed on the heating element, it was necessary to adjust the position of the optics. The 3-D printer was utilize to create a simple mount where the lens of the reflectometer could be inserted and held at the proper distance above the sample on the heating element. Rubber bands were found to be a very effective and simple way to reduce vibrational shifts that the beam spot might undergo during use.

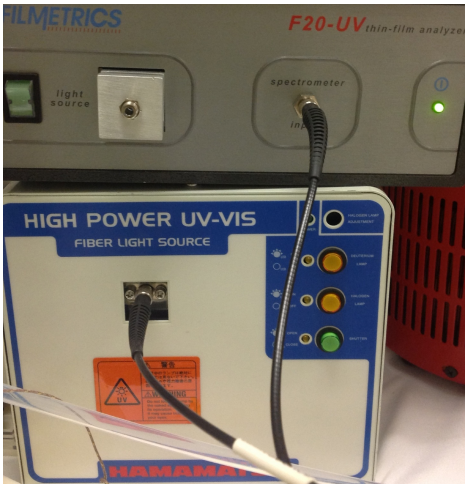

Figure 2-19: The light source and detector electronics used for spectral reflectometry measurements that allowed for *in situ* film thickness measurements.

The last component worth mentioning is the spectral reflectometer. This produced a broad range of light frequencies that could be reflected off of a planar substrate, after which the light would travel back from the sample up through the fiber optics into the detector. Then a reflectance vs. wavelength data plot was produced which would allow one to determine a film thickness based on known index of refraction data.

2.2 Experiment Operational Details

This section will give a detailed overview of how to operate the flow controlled solvent vapor annealing setup with relevant discussion, and the latter part of this section will add information on how to use the solvothermal annealing modification.

2.2.1 Flow Controlled Solvent Vapor Annealing

First, turn on the relevant gas line(s) that will be used for the anneal. For example, set flow rates of 10 sccm for channel 5 (e.g. toluene) and 0.5 sccm for channel 4 (e.g. nitrogen). Make sure that the solvent annealing chamber is completely closed so that solvent vapor does not leak into the working environment. This preparation step

is done in order for the system to reach steady-state in the gas lines preceding the solvent annealing chamber. If the system has not been utilized for a number of days it is necessary to saturate the inner walls of the tubing with the relevant solvents that will be flown through them. When a saturated solvent stream enters a pristine tube, the solvent molecules start absorbing to the tubing walls and initially this tends to decrease the vapor pressure of the solvent molecules in the gas. This continues until a steady state equilibrium is reached where the absorption rate of solvent molecules onto the tubing walls equals the desorption rates of solvent molecules off the walls and into the gas phase. The amount of time necessary to do this depends on how pristine the tubing walls are and how long the tubing line is from the solvent chamber to the annealing chamber. The system as currently set up typically was prepared with at least one hour of solvent vapor flow before the annealing commenced.

Turn on the spectral reflectometer to warm up its lamps, and then the gas flow can be turned off while the solvent vapor annealing chamber is prepared for experimentation. When initially opening the solvent annealing chamber, there will be solvent vapor inside that can be removed with a blast of nitrogen from a nearby nitrogen gun. This will release a small amount of solvent vapor into the air that can be swept away by the neighboring fume hood (there is a fan set up to run in the room that can be turned on during this step to ensure that the solvent vapor is directed towards the open fume hood).

Now that solvent vapor has been removed from the annealing chamber, preparation can begin. The first thing to do is to ensure that the quartz window is entirely clean in the center region where light from the spectral reflectometer will pass through. Any impurities on the quartz window can cause issues for users trying to use this device. This dust gets in the way of the light ray and absorbs different spectra needed for accurate measurements but the effect is subtle and sometimes the reflectometer will apparently give reasonable results that are actually off by tens of nm's. To clean, first rinse the window with soap and water and then dry with a kim wipe. Then, rinse off the top and bottom with acetone and dry with the nitrogen gun. Try not to touch the center region with anything but liquid. Also, allow the window to settle and

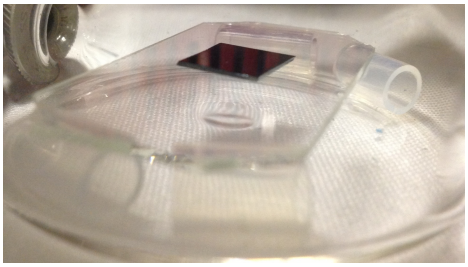

Figure 2-20: The substrate in the annealing chamber lies on a microscope slide supported by small PTFE tubing.

reach room temperature. Rinsing with acetone cools the window, and if the window is cooled and placed on an operating solvent annealing chamber, then solvent vapor will condense on the bottom of the window and the liquid will distorts reflectometry measurements.

Next, place a substrate of interest on the microscope slide suspended by PTFE tubing in the annealing chamber. With the quartz window off, open the raw signal measurement on the Filmetrics, and adjusts the microscope slide placement until a maximum signal intensity is shown. This ensures that the sample is normal to the ray of the measurement beam so that upon reflection a maximum amount of light is directed back to the reflectometer fiber optics for maximum measurement accuracy. An example of a good reflectivity measurement is shown in Figure 2.2.1. Note that the intensity across different wavelengths changes as the device is warming/starting up. This is why it is necessary to warm up the reflectometer before measurements are taken, so that each lamp can reach a steady-state intensity profile and not drift away from baseline measurements that go into modeling film thickness during actual experimental measurements.

With the raw signal still running, place the quartz window in the beam line to qualitatively see the effect on the intensity profile. If the window is clean, there should only be a slight drop in intensity on the low wavelength peak.

With the microscope slides now in proper placement relative to the beam, and the quartz window cleaned, place the samples onto the microscope slide. A minimum of three samples is required, but typically up to six are used as shown in Figure 2.2.1.

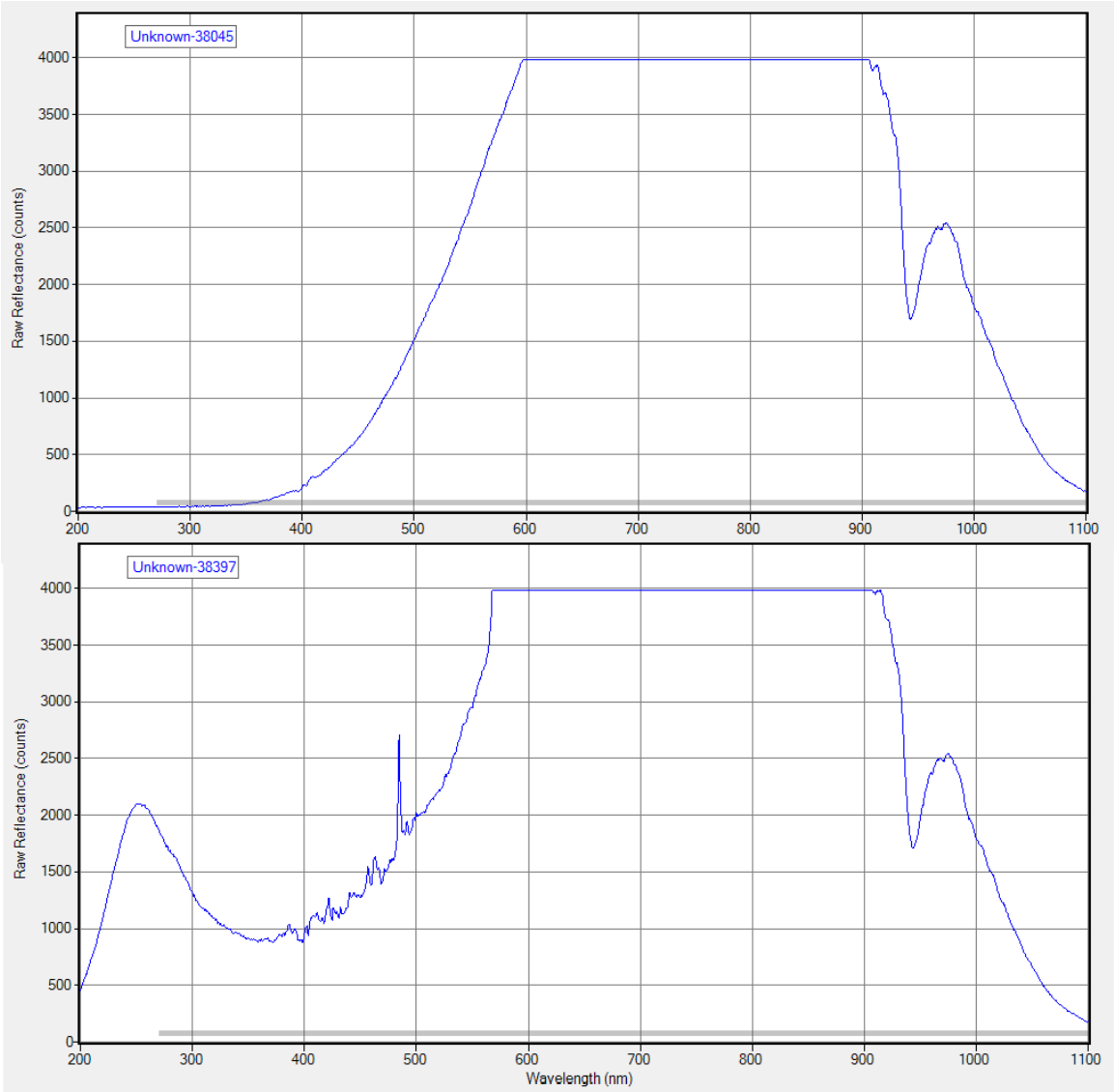

Figure 2-21: The raw signal intensity measurements before and after the deuterium bulb was lit. Initially, only the halogen bulb is on.

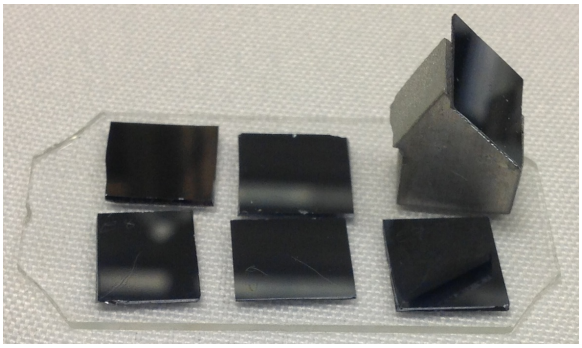

Figure 2-22: Typical sample layout in the annealing chamber. From top left to bottom right: PS film, blank Si, angled blank Si, PS, PS-b-PDMS, PDMS.

One must be the sample, which is the substrate with a polymer (e.g. polystyrene), one must be a blank substrate, and one must be a reflecting piece that directs light away from the direction of the fiber optics. The substrate with a polymer doesn't have to be the same polymer type as the other samples that will be measured.

With these samples in place and the quartz window on, the reflectometry is baselined. First, the polymer is measured to help the device find the nominal intensity range to expect during actual measurements, then the substrate is measured to baseline the maximum intensity and determine the bulb conditions, and then at the third sample, the light beam directed away from the fiber optics by holding the sample at an angle with the fabricated steel chuck. This is done in order to measure the ambient lighting conditions and remove background noise during actual measurements. Make an effort to have the shutter closed as much as possible. The low wavelength light can damage the polymer film, so measurements are typically done as fast as possible by opening the shutter, hitting the measurement button, and then closing the shutter. Typically this takes about four seconds. Measure the film thickness of all of the samples inside the chamber to get the initial film thickness (D_0) before the solvent vapor annealing begins. The chamber can gently slide around on the Filmetrics stage so that the beam spot can be placed on different samples for different measurements.

With the baseline steps completed, the annealing can start. Close the chamber tightly by using clamps that grip both the quartz window and the lip of the solvent annealing chamber. Turn on the mass flow controllers with the same settings that

were used to prepare the gas line and wait a given amount of time until the annealing is finished. Typically this amount of time was one hour. After this, slide the annealing chamber around and keep the fiber optics shutter open so that thickness measurements can be taken for multiple samples. Having a mobile solvent annealing chamber is very advantageous for this step, because it makes it very easy to measure multiple samples during one annealing run.

After the annealing step is complete, it is necessary to quench the system. Typically the window was opened slightly and the chamber was blasted from a distance with the nitrogen gun. Do not blast the nitrogen directly at samples though, or they can fly everywhere. For the thin films, where the BCP was <100 nm, it was assumed that the BCP collapsed quickly enough to freeze in the structure that formed during the anneal. For thicker films, the rate of solvent removal could have a large effect on the self-assembly characteristics found throughout the thickness of the film. These phenomena were explored in the work explained in following chapters. For this reason, it is important to take note of exactly how the films are quenched during the experimentation.

2.2.2 Solvothermal Annealing

The biggest difference between the aforementioned flow controlled solvent vapor annealing process methodology and solvothermo annealing is the sample stage positioning and the application of heat.

For positioning of the stage, the strategy is very similar. Track the raw signal and adjusts the silicon nitride cantilever and the annealing chamber glass base by placing ledges (microscope slides or lab wipes worked) below it until a maximum intensity signal is achieved. Because there is only room for one sample at a time, the baseline steps must be completed in series. First, place a polymer sample in (not the one that will be rapidly annealed) and measure, then place the blank substrate in and measure, and finally just let the beam hit the cantilever, as this does not have much reflection (like the glass platform does in the other setup) and can result in an acceptable baseline. Do these steps with the quartz window on, so that a proper

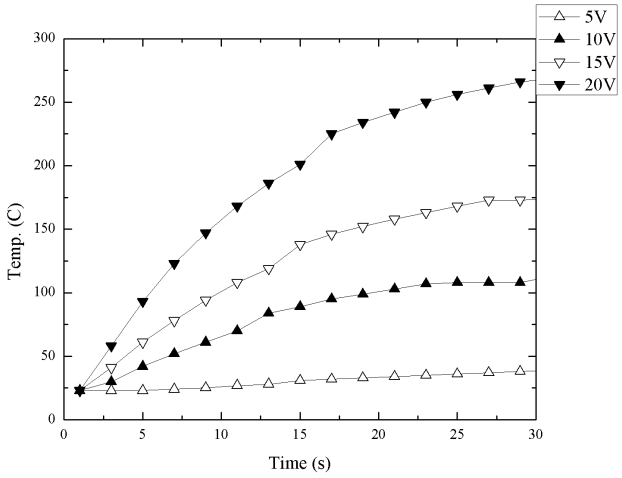

Figure 2-23: The temperature profiles of the tip of the silicon nitride cantilever at different AC voltage setpoints. These were the temperature profiles that the samples experienced during the thermal quenching step of a solvothermal anneal.

baseline is achieved similar to the conditions of the actual experiment.

Next, the saturated solvent environment should be prepared. Turn on the flow of the relevance solvent stream and wait. During my experiments, to ensure a highly saturated environment that would recover quickly after the chamber was opened shortly for the sample being introduced and placed on the cantilever, 2 mL of the solvent liquid (the same as the solvent vapor source liquid) was pooled in the bottom of the chamber. Typically it takes about 10 minutes at most for the annealing chamber to reach saturated conditions.

Set up the Filmetrics to continuously measure at 0.1 s intervals. Commence the measurements and open the shutter which should have the beam aligned with the end of the cantilever. Using a long tweezer holding the sample which will be rapidly annealed, tip the quartz window slightly upwards to create an opening and rapidly place the sample onto the end of the cantilever beam and close the chamber. The transfer should happen within one second and the Filmetrics should immediately start showing measurement displays on the screen. After this, wait for the film to reach a desired swelling ratio, and then initiate the thermal quench.

Turn on the voltage controller and heat the film until a sufficient amount of

solvent has left the sample. This can be tracked by the Filmetrics which will show a continuously decreasing thickness until the temperature raises to a point at which the thermal expansion of the polymer becomes the dominant effect, and the film starts swelling it again slightly. Typically the films where were removed from the chamber before this re-swelling commenced. The best results that I found during my thesis where at a set point of 5 V. It seemed that if the voltage setpoints were too high, heating removed the solvent so quickly that the polymer did not have enough time to anneal properly. The lower voltages allowed for a more relaxed solvents removal rate which gave better results. WARNING: If the voltage setpoint is too high, and oxygen has contaminated the vapor environment, there is a real risk of ignition and explosion. During my safety tests, under worst-case scenario conditions where both of the input and output ports were open to atmospheric conditions (and heptane was evaporating at the bottom of the chamber), this occurred at a 60 V setpoint or around 500 °C.

After the sample reaches the elevated temperatures and the solvent has been removed, the heat should be turned off and the sample should be removed. The elevated temperatures of the sample after the heater is turned off prevents the polymer film from reswelling. Therefore as long as the sample is removed quickly, there should be no danger of morphology changes due to re-swelling of the BCP film after the heater is turned off.

2.3 Digital Revolution

One fascinating aspect of change that has occurred during my time at MIT has been the observation of digital technology starting to profoundly affect how research is done in an academic setting. Due to recent changes in US patent law, where the first to file a patent has priority over the first person to discover a technology, the need to have paper based lab books has diminished. Ideally, but not typically true in practice, a paper research lab book was kept and signed occasionally with a date marking in order to keep track of intellectual property as it was discovered in the lab. But these recent changes to the law have completely negated any reason for keeping such legalistic

practices in place.

A lab notebook, ideally, should be a place where day to day research events and experiments are tabulated, but also a place where experimental processes can be digested and continuously reformulated and optimized. Additionally, a useful lab notebook would be easily accessible to an incoming researcher who is going to continue a given project. Traditional lab notebooks are clearly limited in many regards. For example, they simply journal the day to day happenings in a given project/experiment. If changes are made to the experimental flow, the process would technically have to be rewritten in its entirety every time that it is reformulated in order to always have the most detailed up-to-date process flow.

The ability to digitally record all of these events would have many advantages including options to search, copy and paste different process flows, and pass along the information seamlessly to another researcher without having to physically give away the entire 'lab notebook'. Typical desktop computers or laptops are not practically able to follow a researcher around as he or she attempts to document various steps of an experiment that are happening in real time, especially because researchers work in such disparate locations where it may be hard to bring in and set up such devices. The release of the Apple iPad tablet computer during my thesis may be considered a significant historical event as it ushered in a wave of hand-held tablet computers the size of traditional lab notebooks. (The Apple iPad was not the first tablet computer, there were many before it. However, the iPad was the first small practically-sized tablet (the others before it were the size of large laptops which are currently too bulky) that was released on a large scale that had the backing of thousands of developers helping to create useful applications that could be taken advantage of by a researcher looking to replace his or her lab notebook.)

I had the unique opportunity of possibly having the claim to fame of being the first researcher outside of Apple to use the iPad tablet as a lab notebook (and one of the first general users), as I received it in the mail earlier in the day before the stores were allowed to sell it to the general public. I had the intention of using it as a lab notebook replacement immediately, and I believe it served the purpose quite well. This section

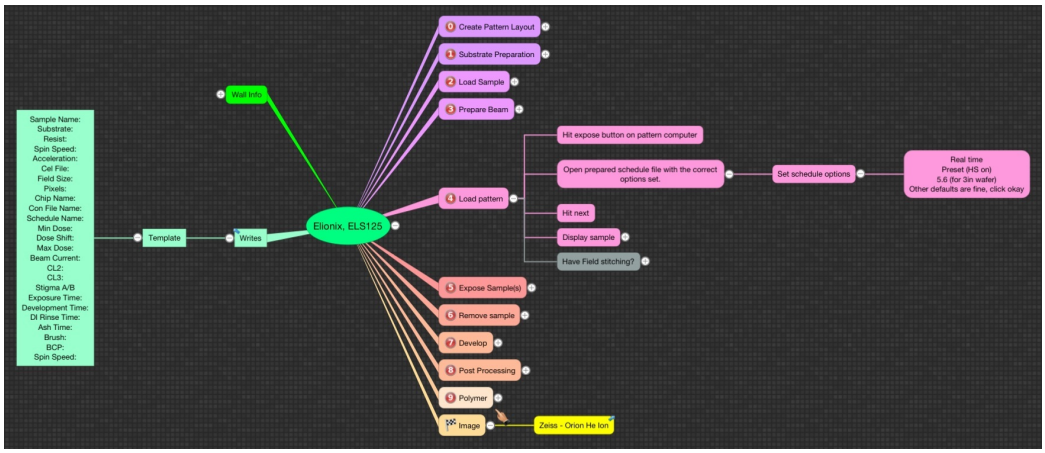

Figure 2-24: A mind map showing one instance of a process flow layout. Every icon with a + sign can be further expanded and the entire flow has over two hundred nodes of information not including links to other maps just as large.

is included in the thesis to pass along some of the methodology that I developed while trying to take advantage of this technology to replace the old-fashioned lab notebook. I do not imagine that it will be very long before every researcher is using digitalized tablets and universities have digital theses with attached tertiary files used by the researcher when doing the practical hands-on work.

2.3.1 Mind Mapping

One piece of software that I found particularly useful was iThoughtsHD. This application allows for one to create and continuously edit an interactive map that can be manipulated easily to reconfigure how and what information is displayed. This type of arrangement and manipulation is called mind mapping and there are many different applications that do this.

Mind mapping has traditionally been used by writers and thinkers as a way to organize thoughts, create outlines, and connect ideas. Recent studies have shown that this method of thought organization is superior to traditional note taking for an individuals ability to recall information[43]. Doing this digitally instead of with paper allows one to constantly change and reformulate the maps in real time without having to redraw the entire mind map. This makes it extremely useful for creating interactive

process flows that are far superior to simple step-by-step manuals, because it allows one to see the big picture and zoom in to find information about exactly what is of interest at the moment (while at the same time allowing for links to images, data files, PDFs, other maps, etc.).

As the process flow is continuously improved upon and modified the mind map becomes more and more streamlined and refined almost to the point of being a final product itself. This is advantageous because it is easily able to be passed along and digested by another researcher trying to reproduce the same process flow. Additionally, he or she is then also able to edit and modify the layout to suit his or her needs and make it exceptionally personal to the experience and explanation that they are familiar with. Being able to keep track of the steps taken in an experiment in extreme detail allows for one to go back and reproduce the results months or even years later just by following the documentation.

This was always theoretically possible in the past with traditional lab notebooks, but humans are inherently driven to minimize their effort for completing a task (hence the drive for developing technologies) and tend to create shortcuts for themselves whether it be by using new acronyms that only they know or by leaving out information that was obvious at the time. One of the advantages of using a computer tablet is that it is exceptionally easy to input text and information when compared to writing with the hand (a simple words per minute measure would suffice in the comparison). In fact, this entire chapter was 'written' by dictation of my voice into the iPads built-in voice recognition module built into the keyboard. When it is so easy to record information, it becomes that much more likely that the information that is relevant is actually going to be kept track of and added to the process flow. This is what I found to be the case to be when using mind mapping software to put together new experiment/process documentation.

2.3.2 Multimedia

Tablets have built-in cameras and this is very useful for keeping track of observations during experimentation. Any tablet application emulating a traditional lab notebook

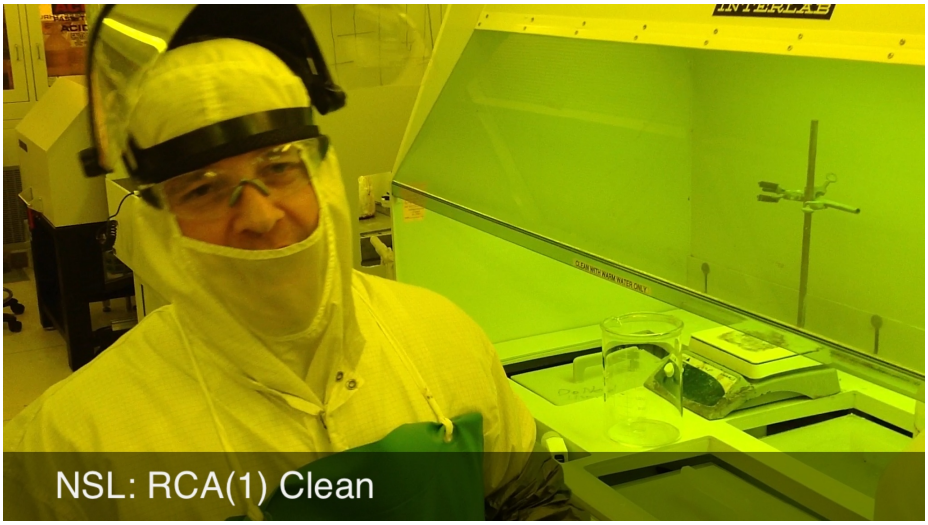

Figure 2-25: A screen cap of a tutorial training video recorded, directed, and edited just using the iPad to facilitate improved knowledge transfer.

(such as Note Taker HD) is already one step ahead of the usefulness of a paper-based notebook. This is simply due to the built-in camera. I found many times when recording information in my journal that I could simply take a picture and insert it as part of my documentation immediately without having to find a printer like was done with a paper lab book. By reducing the barrier for incorporation of digital photos and data into a lab notebook it was much more likely to be included in the first place.

These cameras can also be used to record and edit video productions. By simply using an application like iMovie, I was able to record many short and succinct videos explaining a particular process flow. These would be very useful in terms of time-saving and efficiency for the training of future students using these devices or processes. Pictures and videos take the place of hundreds of words of explanation and are almost always more valuable in terms of showing someone how a given process is actually done or clarifying particular concepts.

2.3.3 Digital Library

The whole of human knowledge can be accessed anytime of the day on a handheld tablet computer connected to the Internet. It almost goes without saying that it was

useful to have immediate access to the trove of scientific journals that were collected as references for this research. Being able to access these immediately while doing experimentation in order to cross check with what they were doing was of great value.

Chapter 3

Basic Solvent Vapor Annealing Applications

3.1 Introduction

This work takes advantage of one aspect of the basic SVA setup that is not possible with the current implementation of our flow controlled SVA setup, namely, the ability to simply allow the vapor pressure conditions to decrease gradually over large time scales (hours) and apply these gradients to high-χ BCP systems where the top of the BCP film is usually dominated by the lower surface energy block (PDMS). Slow-drying allows solvent vapor concentration gradients to form in the film and in this work resulted in perpendicular orientation of high-aspect-ratio polystyrene-block-polydimethylsiloxane (PS-b-PDMS) cylindrical and lamellar PDMS microdomains. Perpendicularly oriented microdomains occurred throughout the film thickness, except at the air interface, where a layer of in-plane microdomains formed due to the surface energy difference between PS and PDMS. In contrast, thermal annealing produced in-plane orientation throughout the film thickness. The solvent-annealed perpendicular orientation was observed for cylindrical morphology PS-b-PDMS of 16 and 45 kg/mol, where PDMS is the minority block, and lamellar PS-b-PDMS of 43 kg/mol. To obtain fully perpendicular microdomain patterns, a nonselective high-powered 450 W CF_4/O_2 reactive ion etching process was performed to remove the top layer of the films.

Substrate patterning using electron beam lithography produced local registration of 17 nm period hexagonal cylinder patterns.

3.2 Experimental Methods

Detailed experimental methods for achieving this follow, but discussion of the basic solvent annealing setup is explained and discussed in Chapter 2. Self-assembly of PS-b-PDMS films: PS-b-PDMS diblock copolymers with molecular weights of cylindrical 45.5 kg mol-1 (polydispersity index (PDI) 1.15, f_{PS} 0.68), 16 kg mol-1 (PDI 1.08, f_{PS} 0.69), and lamellar 43 kg mol-1 (PDI 1.08, f_{PS} 0.50) were purchased from Polymer Source, Inc. Supplier-provided size exclusion chromatography data indicated a single peak for the SD16, but a shoulder in the SD45 peak indicates the possible presence of homopolymer.

A total of 3-5 wt % of the PS-b-PDMS solution in cyclohexane was spin-coated on as-received Si substrates with thickness from 150 to 300 nm. Solvent annealing was carried out using acetone or chloroform in a 9.3 mL glass Petri disk with a cover until the solvent was fully evaporated, which took less than 4 h. The annealed BCP films were first treated with high power CF_4/O_2 RIE (30 s, 450 W) to etch the parallel oriented top layers (120 nm) and then O_2 RIE (30 s, 90 W) to selectively remove the PS domains and make high-aspect-ratio nanopatterns.

Template preparation: The nanopost templates were fabricated using electron beam patterning of hydrogen silsesquioxane (HSQ), a negative-tone electron beam resist. HSQ films (FOx 1% solids from Dow Corning) were spin-coated on silicon substrates. Hexagonally arranged single-pixel dots were exposed in a Raith 150 electron-beam lithography tool at 30 kV acceleration voltage. The samples were developed in 0.25 M NaOH/0.7 M NaCl in distilled water to remove unexposed resist and to reveal the topographical nanostructures.

Characterization: To observe the morphology of the films at the film-substrate interface, a Si wafer with 50 nm thick SiO_2 layer was used as the substrate. The films were partially immersed in 5 wt % HF aqueous solution to dissolve the SiO_2 sacrificial

layer and the released polymer film was flipped over to expose the bottom interface of the film. The morphology of the block copolymer patterns was observed by field emission-scanning electron microscope (FE-SEM, Zeiss/Leo Gemini 982) operated at 5 kV. The samples for FE-SEM were coated with a thin Au-Pd alloy film to avoid charging effects.

3.3 Results and Discussion

In microelectronic device manufacturing, a feature half-pitch of approximately 22 nm represents the limit of conventional photolithographic methods with 193 nm immersion photolithography. Alternative approaches for forming sub-22 nm features, such as electron beam lithography and extreme UV lithography, have drawbacks in terms of cost and throughput. In contrast, block copolymer microphase separation spontaneously generates microdomains with period of a few nm and above, and thin films of block copolymers can therefore be used to form nanoscale patterns over a large area in a fast, low cost process. Thus, many research groups have studied block copolymers for potential applications in nanolithography and device fabrication.[5,16,19,44–46]

To use a block copolymer film for sub-20 nm pattern generation, a high χ parameter and good etch selectivity between the blocks are required to allow small period features to be formed and for one block to be subsequently removed. In addition, a perpendicular orientation of cylindrical or lamellar microdomains forms high-aspect-ratio patterns which are convenient for certain methods of pattern transfer. Polystyrene-block-polymethylmethacrylate (PS-b-PMMA) has good etch selectivity[46], and it can readily form perpendicularly oriented microdomains by controlling the surface chemistry[14] and substrate roughness[47] or by using electric fields[46] or surfactants[48] because the two blocks have similar surface energies. However, $\chi_{\mathrm{PS-PMMA}} \sim 0.06$ at room temperature[49], which is modest, giving a lower bound to the size of microdomains that can be formed. Other block copolymer systems, such as PS-block-polyethylene oxide (PS-b-PEO)[50], polystyrene-block-polymethylmethacrylate-block-polyethylene oxide (PS-b-PMMA-b-PEO) triblock copolymer[51], and PS-b-PEO with organosilicate[52],

have been explored to obtain microdomains with smaller dimensions. Perpendicular orientation of the PS-b-PEO/organosilicate microdomains was produced in a solvent annealing process with humidity control or mixed solvents, but this system required subsequent high temperature processing to remove the organic components.

Polystyrene-block-polydimethylsiloxane (PS-b-PDMS) is attractive for nanolithography on the sub-10 nm length scale because it has a high χ parameter ($\chi_{\mathrm{PS-PDMS}} \sim 0.27$)[53] and high etch selectivity between the blocks[49]. Highly ordered sub-10 nm width lines[13,36,54], dots[9,13], and complex patterns[36,55,56] have been achieved from this block copolymer using trenches[13,13,54] and nanopost templates[9,36] to guide the self-assembly. However, it is a challenge to obtain a perpendicular orientation of cylindrical or lamellar microdomains because of the large difference in surface energy γ between PS (γ_{PS} 40.7 mN/m) and PDMS (γ_{PDMS} 20.4 mN/m)[57], which promotes formation of a layer of PDMS at the air interface.

We demonstrate high-aspect-ratio perpendicular orientation of cylindrical and lamellar microdomains in PS-b-PDMS block copolymer films using solvent annealing combined with reactive ion etching (RIE). We first describe the process for 16 kg/mol PS-b-PDMS with a volume fraction of PDMS of $f_{\mathrm{PDMS}} = 0.31$, designated SD16, which has a cylindrical morphology in bulk and a period $L_0 = 18$ nm. Films 300 nm thick were produced on either brush-coated or as-received silicon wafers from a 5 wt % solution of the block copolymer in cyclohexane. Films were annealed either by thermal annealing at 170 °C for 3 days or by solvent annealing in acetone vapor. The solvent anneal was performed by placing the samples into a glass Petri dish with glass or quartz plate lid[13] in which $V_s = 1$ cm^3 acetone was present. The leak is caused by a small gap between the chamber and its lid. The surface area of the liquid acetone was S = 4.8 cm^2 and the total chamber volume was 9.3 cm^3. The S/V ratio (V is the empty volume of the chamber = (9.3 - V_s) cm^3), which we used earlier to parametrize the solvent anneal process, took values of 0.54, 0.56, 0.58, 0.60, and 0.66 cm^{-1} for solvent volumes of $V_s = 0.5$, 0.75, 1.0, 1.25, and 2.0 cm^3, respectively. The acetone fully evaporated within 4 h, after which the samples were removed.

Figure 3.3 shows the results from SD16 films. The microdomains were imaged by

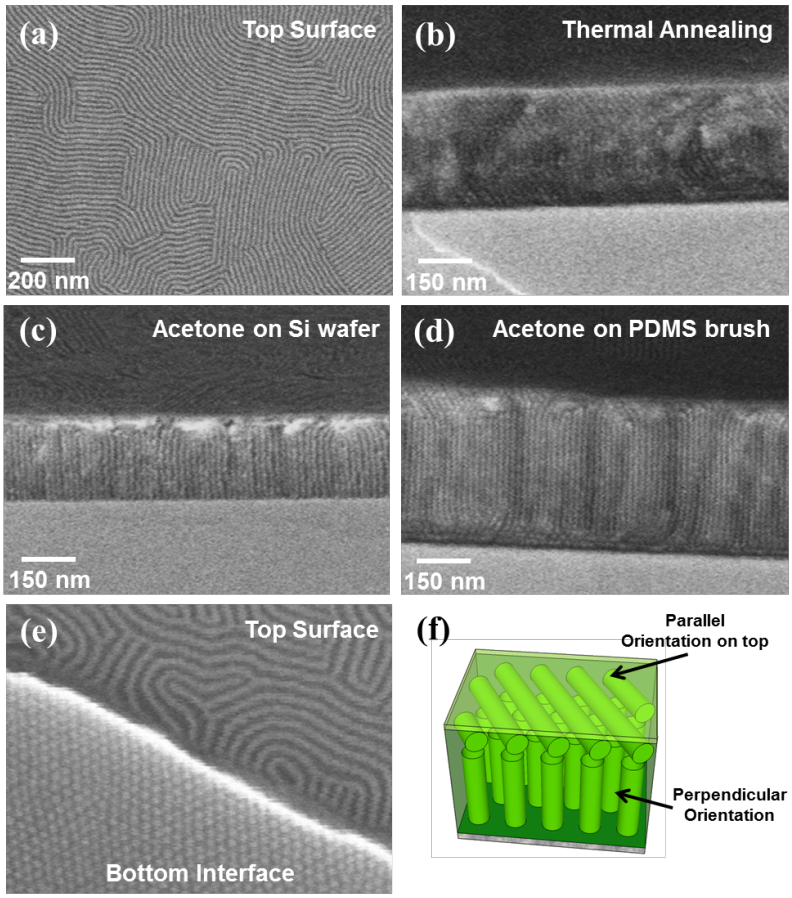

Figure 3-1: Microdomain orientation of 16 kg/mol PS-b-PDMS thick films (>200 nm). (a) Top surface of acetone-annealed BCP film. Cross-section SEM images of films (b) thermally annealed at 170 °C for 2 days, (c) acetone vapor annealed on pristine Si wafer, and (d) acetone annealed on a PDMS brush-coated wafer. (e) Acetone annealed BCP film deposited on a pristine 50 nm SiO_2 coated wafer, as in (c). The film was dissolved from the substrate and folded over when it was immersed in 5 wt % HF aqueous solution. The top-right region shows the morphology of the top surface, while the bottom-left region shows the morphology at the substrate/film interface. (f) A schematic of the solvent annealed PS-b-PDMS film in (e).

using a 50 W CF_4 RIE for 3 s to remove the thin PDMS wetting layer (4 nm) present at the top surface, followed by an O_2 RIE for 20 s to partly etch the exposed PS domains leaving oxidized PDMS visible as bright contrast. Both thermally annealed and solvent annealed films formed in-plane cylinders at the top surface of the films, seen in Figure 3.3a. However, in the cross-sectional SEM images, while the thermally annealed films showed in-plane hexagonally packed cylinders throughout the thickness (Figure 3.3b), the solvent annealed films showed perpendicular orientation in the bulk of the film (Figure 3.3c,d). For the untreated Si wafer, the perpendicular orientation was present at the substrate/film interface (Figure 3.3c, e, and f), while the films on a PDMS brush-coated Si wafer formed perpendicular orientation only in the middle of the film and parallel orientation at the substrate/film interface (Figure 3.3d). We showed previously that the surface chemistry of the substrate affects the self-assembly of thin films of PS-b-PDMS, with a PDMS brush enhancing the annealing kinetics.[49] However, the PDMS-coated substrate caused a PDMS layer to form at the interface, promoting an in-plane orientation at the substrate.

To obtain high-aspect-ratio cylinders throughout the film thickness, it is necessary to remove the in-plane oriented top layers of microdomains, shown schematically in Figure 2a. This was done with a high power 450 W CF_4/O_2 RIE which removes both PS and PDMS at a similar rate. The acetone-annealed films had in-plane cylinders at the top surface (Figure 3.3 b) but after removing the top 60 nm of the BCP films using 450 W CF_4/O_2 RIE for 15 s followed by a 20 s O_2 RIE to etch into the PS, a perpendicular cylinder orientation was seen over part of the film (Figure 3.3c). Further etching to a depth of 120 nm revealed a dominant perpendicular orientation (Figure 3.3d and 3.3e). Therefore, the in-plane cylinders were present in a top layer that had a thickness between 60 and 120 nm (3-6 L_0), and underlying this, the cylinders had a perpendicular orientation.

This perpendicular orientation could also be formed in PS-b-PDMS with other molecular weights and morphology. Figure 3.3 shows perpendicular orientation of lamellae from a 43 kg/mol $f_{\mathrm{PDMS}} = 0.50$ PS-b-PDMS (SD43) and cylinders from 45 kg/mol $f_{\mathrm{PDMS}} = 0.31$ PS-b-PDMS (SD45) films using solvent annealing followed by a

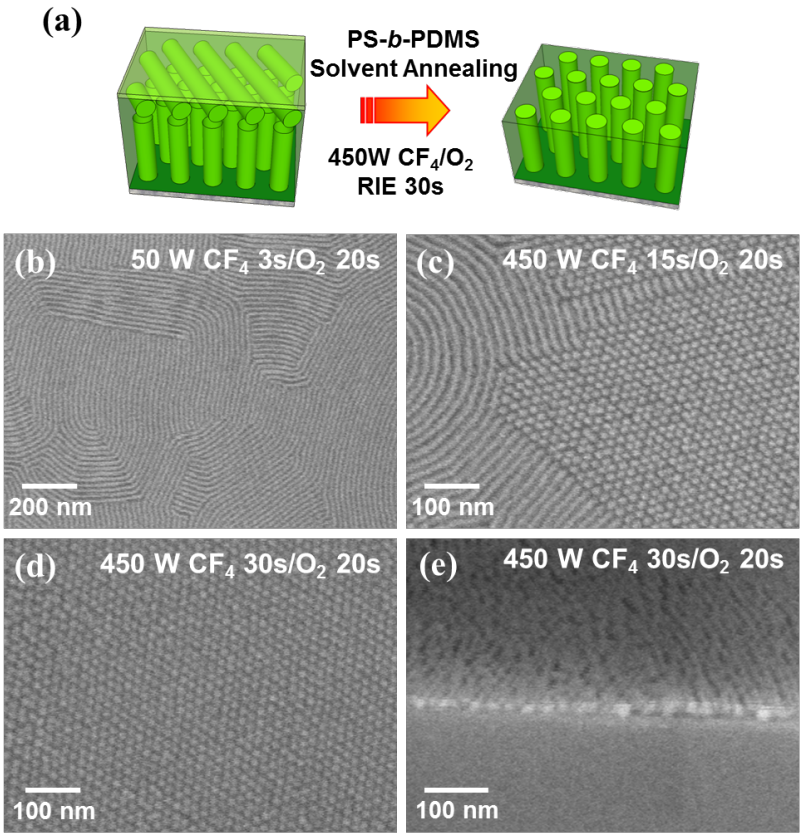

Figure 3-2: Reactive ion etching (RIE) process for removing top layers of 160 nm thick 16k PS-b-PDMS block copolymer film microdomains. (a) A schematic of the structure of PS-b-PDMS films on a Si wafer without a brush after solvent annealing then RIE. (b) Top surface morphology treated by 50 W CF_4 RIE for 3 s and then O_2 RIE for 20 s. (c) 60 nm etched morphology treated by 450 W CF_4/O_2 RIE for 15 s and then O_2 RIE for 20 s. (d) In-plane and (e) cross-section SEM images of 120 nm etched morphology treated by 450 W CF_4/O_2 RIE for 30 s and then O_2 RIE for 20 s.

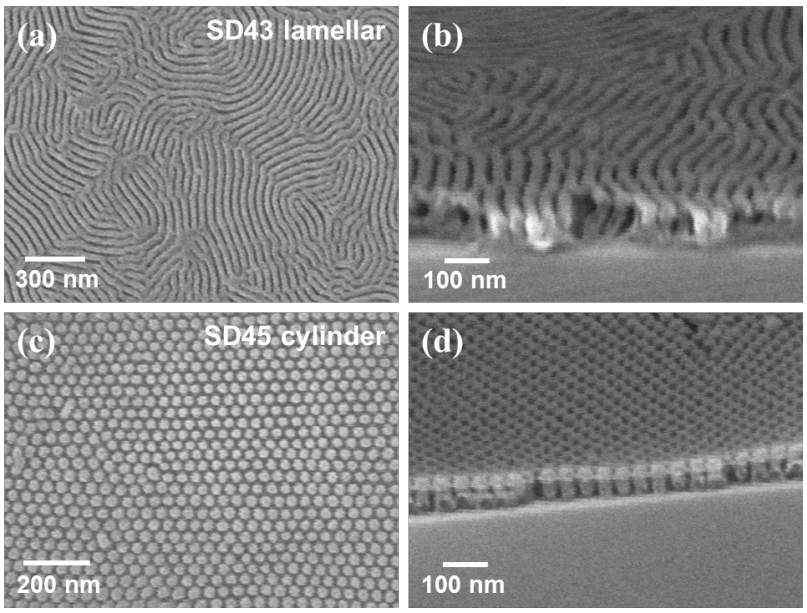

Figure 3-3: Perpendicular oriented lamellar and cylindrical PS-b-PDMS block copolymer thin films after 450 W CF_4/O_2 RIE etching and 90 W O_2 RIE. (a) In-plane and (b) cross-section FE-SEM images of perpendicular lamellar morphology from a 43k PS-b-PDMS thin film under acetone vapor annealing. (c, d) Perpendicular cylinder morphology from 45k PS-b-PDMS thin film under chloroform vapor annealing. The horizontal feature in the film in (d) is believed to be caused by partial removal of the PS from the top surface before sectioning and etching from the side.

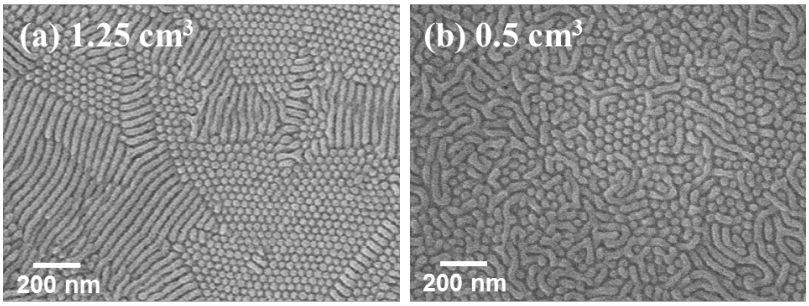

Figure 3-4: Solvent vapor pressure effects on the orientation of 45 kg/mol cylindrical PS-b-PDMS block copolymer. Films 300 nm thick were treated with 30 s of 450 W CF_4/O_2 RIE and then 30 s of 90 W O_2 RIE. Annealed with (a) 1.25 cm^3 and (b) 0.5 cm^3 of chloroform.

high power CF_4/O_2 RIE process. The 43 kg/mol film was 250 nm thick and was solvent annealed in acetone (V_s = 1.5 cm^3 acetone). Figure 3.3a,b shows high-aspect-ratio line-space patterns with 100 nm height and 42 nm period from SD43. SD45 formed perpendicular cylinders after annealing with chloroform. Figure 3.3c,d shows 80 nm high, 36 nm period close-packed cylinders with a 29 nm diameter.

The perpendicular orientation was sensitive to the vapor pressure of the solvent and annealing time, which was altered by changing the amount of solvent. In the case of the SD45, V_s = 0.75 cm^3 of chloroform was the optimum condition to obtain perpendicular orientation, Figures 3.3c and 3.3d. With 1.25 cm^3 of chloroform, there was a larger fraction of in-plane cylinders even after removing the top 120 nm of the film, while a lower vapor pressure (0.5 cm^3 of chloroform, Figure 3.3b) gave cylinders with greater curvature.

To understand the effects of the solvent on the microdomain morphology, it is necessary to determine the time evolution of the solvent vapor for different initial amounts of solvent. First, the weight loss of the annealing chamber was measured as the solvent evaporated for the case of 0.75 cm^3 chloroform (Figure 3.3a), 2 cm^3 chloroform, and 2 cm^3 acetone (not shown). From the density of the solvents, this indicated a flow rate of 5.16 mm^3/min for chloroform and 5.52 mm^3/min for acetone. The rate of weight loss was the same for the different initial amounts of chloroform, which showed that the leak rate was independent of the amount of solvent in the

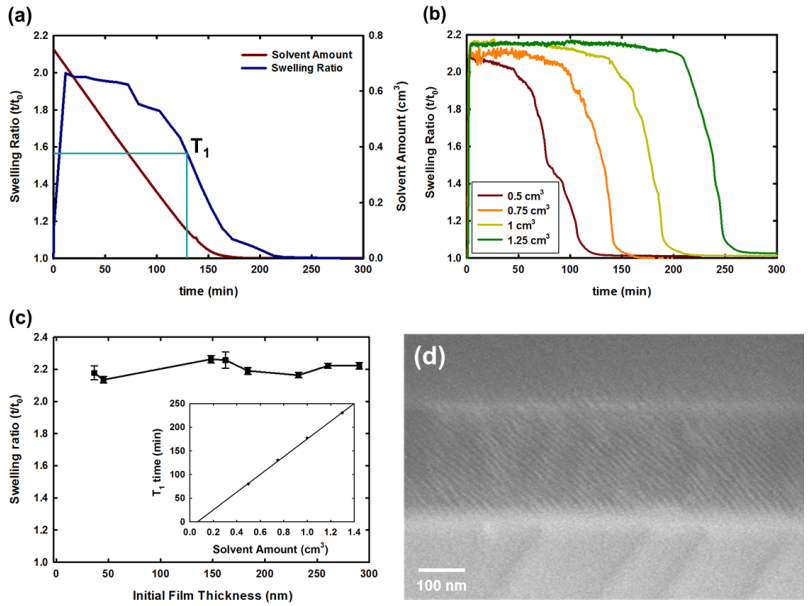

Figure 3-5: (a) Change in mass of solvent with time and swelling ratio of 380 nm thick SD45 annealed in 0.75 cm^3 chloroform. T1 is the time at which the swelling ratio is 1.55, half of the maximum swelling ratio observed. (b) *In situ* swelling ratio of SD45 thin films V_s time, corresponding to different initial solvent amounts. (c) Swelling ratio of SD45 film V_s initial film thickness after 15 min of solvent annealing with 1 cm^3 of chloroform. Inset: A plot of T1 V_s initial solvent volume determined from the data in (b). (d) SD16 film after rapid drying with a nitrogen gun showing tilted cylinders.

chamber, at least in the initial stages of the experiment while liquid solvent remained. The solvent was fully evaporated after 380 min for 2 cm^3 acetone or chloroform and 150 min for 0.75 cm^3 chloroform.

In separate experiments the swelling ratio of SD45 films was measured versus time for different solvent volumes. (To enable the *in situ* swelling ratio measurements, the glass lid of the chamber was replaced with a quartz plate, but this had only a small effect on the leak rate, decreasing it by a few percent.) Figure 3.3a,b shows the swelling ratio versus time for SD45 in chloroform. In each case the film swelled quickly to a swelling ratio of 2.1 and then deswelled over a period of up to 1 h. The maximum swelling ratio increased slightly with solvent volume, from 2.1 to 2.2. This is less than the swelling ratio of SD45 in a closed container of chloroform, which is 2.3-2.4, showing that the beaker with the leak exposed the sample to a solvent vapor pressure slightly smaller than the saturated vapor pressure (i.e., 198 Torr for chloroform at room temperature, 25 °C). Figure 3.3c shows that the maximum swelling ratio was independent of film thickness in the range of 30-300 nm.

To quantify the swelling behavior, we define time T1 as the time taken for the swelling ratio to drop to 1.55, that is, half way between 1 and the maximum swelling ratio of approximately 2.1. T1 = 130 min for 0.75 cm^3 chloroform, Figure 3.3a. By comparing the rate of loss of the solvent with the swelling ratio, T1 corresponded to the time at which only about 0.07 cm^3 of chloroform remained in the chamber. About 160 min was required for all the liquid chloroform to evaporate from the weight change. (The amount of saturated chloroform vapor present within the chamber corresponds to only 0.008 cm^3 liquid.)

Figure 3.3b shows swelling ratios for four different amounts of solvent. T1 increased almost linearly with the initial solvent amount, Figure 3.3c inset. These data indicate that the films swelled to their maximum value and remained at that value for a time approximately proportional to the initial amount of solvent. As the liquid solvent became exhausted, the vapor pressure dropped and the film dried and deswelled over about an hour, independent of the initial solvent amount.

In comparison to the slowly dried films described above, rapidly quenched films

showed a different microdomain orientation. Rapid quenching of films by exposing the sample to air led to a mixture of orientations of cylinders. Quenching using nitrogen blowing, as in Figure 3.3d, usually formed a tilted orientation in the bulk of the films and in-plane orientation at the top surface. When the film was initially swelled in a saturated vapor in a closed chamber and then rapidly quenched by exposing it to air, in-plane cylinders were observed.

We suggest that, in these thick films, a gradient in solvent concentration develops as solvent escapes from the top surface of the film, so the solidification boundary between block copolymer chains that are still mobile and those that have low diffusivity moves from the film surface to the substrate interface as drying proceeds[58]. *In situ* GISAXS measurements of BCP films[59] showed that films that swelled by a factor greater than about 2 can be well ordered in the swelled state, so it is likely that cylinders or lamellae were already present in the swelled films. Films initially swelled by 2.1-2.2 are assumed to have poorly ordered cylinders or lamellae, and slow drying allowed them to reorient perpendicular to the substrate. However, rapid quenching preserved a more random orientation or caused tilting, possibly from off-normal drying caused by the nitrogen jet. Films annealed at a higher swelling ratio (2.3-2.4) and a longer anneal time, or those thermally annealed, had already formed in-plane cylinders throughout the film thickness during the anneal, and this orientation was preserved during deswelling or rapid cooling.

Any tendency for perpendicular orientation promoted by the solvent anneal process had to compete with in-plane orientations promoted by the preferential wetting of PDMS at the air interface and at a PDMS-brushed substrate when the brush was used. In highly swelled films, or those annealed for a long time, this in-plane orientation propagated from the surface to the interior of the films, forming in-plane cylinders throughout the film thickness, whereas in the slowly dried films, the parallel orientation was only present at the surface(s). A related result was obtained from solvent-annealed PS-b-PEO with organosilicate films[52] in which an initial perpendicular orientation evolved into an in-plane orientation at the film surface with extended annealing time in a non-neutral solvent.

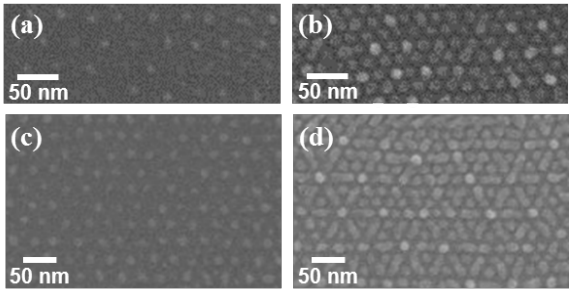

Figure 3-6: SEM images of (a) a 38 nm period of sparse hexagonal lattice of HSQ post templates and (b) a perpendicular oriented cylindrical morphology of solvent annealed 16 kg/mol PS-b-PDMS thin films on 38 nm period HSQ post arrays; (c) 30 nm period sparse hexagonal HSQ posts and (d) perpendicular oriented cylinder patterns from 16 kg/mol PS-b-PDMS on 30 nm period post arrays.

This simple picture is complicated by changes that may occur in the swelling ratio with film thickness[60] and a lower equilibrium solvent concentration near the substrate in thick films due to greater constraint of the polymer chains[61], but it indicates that the time dependence of the solvent vapor pressure is a key determinant of the microdomain orientation.

Long range order is necessary for device applications, for example, in semiconductor devices or patterned media. To template the perpendicular microdomains, the substrate was patterned with topographical features made using hydrogen silsesquioxane (HSQ) resist exposed using electron beam lithography. After development, the HSQ formed a silica-like material. The posts were 10 nm tall and had a period of 38 nm (Figure 3.3a) or 30 nm (Figure 3.3c), a diameter of 10 nm, and covered an area equal to 10 m^2. The SD16 cylindrical PS-b-PDMS block copolymer was spin-cast on the posts and solvent annealed, and then most of the film thickness was removed by etching so that the alignment of the perpendicular cylinders near the substrate surface could be seen. In the 38 nm post array, the spacing was commensurate with the BCP = 2 L_0, and it is clear in Figure 3.3b that the microdomains subdivided the spacing of the posts to form a 20 lattice analogous to the templating of spherical microdomains by a post lattice[9]. In Figure 3.3d, the post lattice is incommensurate with L_0 (Lpost/L_0 = 1.67), and commensurability arguments would suggest a 11 lattice would form.

Figure 3.3d shows instead some evidence for in-plane segments of cylinders forming in between the posts. The electron-beam-irradiated regions of the HSQ tended to promote an in-plane cylinder orientation even on a substrate where perpendicular cylinders formed at the film-substrate interface.

The proposed model for the slowly drying film would suggest that substrate patterning should be ineffective at templating the block copolymer because the film dries at the air interface first. However, it is likely that the substrate patterns influence the locations and orientations of the microdomains near the substrate leading to local registration of the microdomains. A more detailed cross-sectional study of the film would clarify the thickness of the film that is affected by the substrate pattern.

3.4 Summary

This work demonstrated how perpendicularly oriented microdomains could be achieved in PS-b-PDMS block copolymers of different molecular weights and morphologies using a slowly drying vapor solvent annealing process. This is important because high-aspect-ratio nanostructures were obtained after removal of the top layers of in-plane microdomains. The ability to vertically align high-χ BCPs improves pattern transfer prospects and adds to our understanding of the importance of solvent removal during BCP self-assembly. In the next chapter, the results of the flow controlled SVA setup are discussed and it should be noted that very fast quenches were used in these studies to freeze in the structure as much as possible. Theoretical studies predict that fast quenching can freeze in structures for sufficiently thin films[62], and this assumption holds for the polymer systems in Chapter 4.

Chapter 4

Flow Controlled Solvent Vapor Annealing

4.1 Introduction

This chapter discusses the results of the flow controlled solvent vapor annealing (SVA) setup which was discussed in Chapter 2. Due to the limitations of the basic solvent vapor annealing setup that were discussed in Chapters 2 and 3, this system was constructed to better understand the available experimental parameter space available to explore in a self-assembly BCP sytem. This work also led to a better understanding of how the different chemical solvent species in a cosolvent anneal interacted with the different polymer blocks.

SVA of block copolymer thin films can produce a range of morphologies different from the equilibrium bulk morphology. By systematically varying the flow rate of two different solvent vapors (toluene and n-heptane) and an inert gas, phase maps showing the morphology versus vapor pressure of the solvents were constructed for 45 kg/mol polystyrene-block-polydimethylsiloxane diblock copolymer films of different thicknesses. The final morphology was correlated with the swelling of the block copolymer and homopolymer films and the solvent vapor annealing conditions. Self-consistent field theory is used to model the effects of solvent swelling. These results provide a framework for predicting the range of morphologies available under different

solvent vapor conditions, which is important in lithographic applications where precise control of morphology and critical dimensions are essential.

The self-assembly of block copolymer (BCP) thin films has become increasingly important as a method for nanoscale patterning as the resolution limits of optical lithography are approached[3,6,8,32]. BCPs offer a bottom-up approach to nanolithography that is able to reach feature sizes of 5 nm and above, surpassing the resolution obtainable by conventional photolithography at lower cost than electron beam lithography. From a technological standpoint, the self-assembly of diblock copolymers presents a high-throughput method for making a variety of 2D periodic or complex patterns consisting of lines and dots from the self-assembly of cylindrical, spherical, or lamellar microdomains[10]. As mentioned in Chapter 1, the equilibrium morphology, periodicity, critical dimension size, interfacial width, and diffusivity depend on χ, N, and f of each block[10,11,34,63].

Microphase separation and/or significant reordering or morphology changes of microdomains can be achieved using thermal annealing, in which the temperature is raised to just below the orderdisorder temperature (ODT) in order to improve diffusivity[34,64]. The resulting microdomain morphology and orientation can be manipulated to some extent by altering the BCP film thickness[65] or substrate chemistry. Polystyrene-block-poly(methyl methacrylate) (PS-PMMA) is an exemplary BCP for nanolithography with an ODT of 200 °C for a molecular weight of 29 kg/mol and volume fraction 0.5[8,66], and readily forms microdomains oriented perpendicular to the film plane because PS and PMMA have similar surface energies at the annealing temperature[8,32]. However, its relatively low χ value (0.06 at room temperature)[67] limits the minimum microdomain period in this block copolymer system and therefore the minimum feature size. Higher χ BCP systems allow for smaller feature sizes but the theoretical ODT is often well above the polymers degradation temperature making thermal annealing less practical. For example, if the aforementioned 29 kg/mol block copolymer had a χ of 0.27, the theoretical ODT would exceed 10,000 °C, well above the degradation temperature of 450 °C[68,69].

In contrast, solvent vapor annealing (SVA)[13,50,59,70–78] can be carried out at ambient

temperatures. It improves the kinetics of self-assembly by plasticizing the polymer with the incorporation of solvent molecules. This increases the free volume available for polymer diffusion and decreases the glass transition temperature, T_g[79]. The choice of solvent(s) for SVA is based to first order on consideration of the relative Hildebrand solubility parameters, δ. For nonpolar materials the solubility parameter is a good indicator of solubility; in particular, a polymer and a solvent are typically miscible when $|\delta_{\text{poly}} - \delta_{\text{solvent}}| < 2.5\sqrt{\text{MPa}}$[80]. The chain conformation and flexibility also affect the energy required to unwind polymerpolymer segmental contacts and therefore the amount of solvent that a given polymer will absorb[81]. The amount of solvent incorporation during exposure to the solvent vapor can be tracked *in situ* by measuring film swelling using a number of optical spectroscopy techniques[12].

Exposure to a solvent vapor has several effects on the BCP, including an increase in volume and diffusivity, a decrease in the effective χ proportional to the amount of solvent present at the interface between the blocks[82,83], a change in relative surface energies of the blocks at the vapor/BCP interface, and a change in the effective f dependent on the swelling of each block by the solvent. SVA has the added advantage of reversibility, in which the microdomain morphology can be changed repeatedly by changing the solvent vapor conditions[13,49]. SVA therefore enables tuning of the periodicity and the morphology over a wide range[13,20,84,85], and by modifying the surface energy of the film/air interface, SVA can mitigate preferential wetting by one block which favors in-plane microdomain orientations. This is particularly important in high-χ BCPs which have greater differences between the surface energies of the blocks, making it more difficult to form the perpendicularly oriented microdomains desirable for nanolithography.

SVA has often been carried out using a simple experimental system in which thin BCP films are placed in a chamber which also contains a reservoir of liquid solvent(s), whose evaporation provides an atmosphere of solvent vapor[85]. This technique has been used to demonstrate tunability of the morphology in polystyrene-block-polydimethylsiloxane (PS-b-PDMS, $\chi = 0.27$) in a vapor produced from a liquid mixture of toluene and heptane[13], and even greater tunability of higher-χ poly(2-

vinylpyridine)-block-polydimethylsiloxane in a variety of solvents[86]. However, in the reservoir system it is difficult to independently control the partial vapor pressures of the solvents. In contrast, continuous flow systems provide simultaneous flow, mixing, and reactions of flowing species[87,88], and have been used for solvent annealing by exposing the sample to a saturated vapor stream produced by bubbling inert gas through a liquid solvent. This enables control over the vapor concentration[65,89] and has been used to investigate solvent vapor pressure and deswelling rate effects on microdomain morphology and orientation, for example, using a combinatorial microfluidic approach[70]. Vapor pressures can be varied by diluting the solvent vapor using a separate stream of N_2[58,76]. However, a systematic investigation of the morphological effects of independent control of the vapor pressures of two different solvents on a BCP film has not been presented.

This study demonstrates the effects of varying the flow rates of two different solvent vapors and a diluent gas on the microphase separation of a BCP film by showing how the morphology of the microdomains can be mapped as a function of vapor pressure and swelling ratio, and compare the results to those obtained on the same BCP annealed using a solvent reservoir. This provides a general framework for understanding the SVA process and for designing processing conditions that allow specific morphologies to be achieved in a BCP film. The next section describes detailed experimental methods for achieving these results.

4.2 Experimental Methods

Thin films of PS-b-PDMS ($D_0 \approx 38$ nm) and PDMS (≈70 nm) were spun-cast onto 1 cm 1 cm Si wafers that were pretreated with an hydroxyl-terminated PDMS brush layer (0.8 kg/mol, 14 h at 170 °C followed by a toluene rinse) to increase mobility for the BCP and to improve wetting for the PDMS, which is very prone to dewetting due to its low T_g (≈100 °C). PS (≈70 nm) films were spun-cast onto prime Si wafers. The thin films were placed inside the annealing chamber, and their thicknesses were recorded by spectral reflectometer. Because of the film thickness gradients that can

occur during spin coating on such small samples, only the most uniform areas of the center region of each sample was considered for this analysis. Different combinations of flow rates for each of the solvent lines and for the N_2 dilution line were swept. These flow rates resulted in the annealing chamber reaching steady state after 15 min. After 1 h, the reflectometer was rebaselined to take into account the presence of solvents which added absorption peaks in the UV and then the polymer film thicknesses were recorded. The BCP thin films reached their steady state equilibrium morphology after approximately 30 min, with longer annealing time effective in improving microdomain size and orientation. The BCP thin films were then reactive-ion etched by 5 s of CF_4 (10 mTorr, 90 W) and 22 s of O_2 (10 mTorr, 90 W) to remove the PS matrix and the PDMS surface layer to reveal the underlying oxidized PDMS morphology.

For the solvent vapor annealing, a N_2 (Airgas, Inc., 99.9997% purity) backpressure of 200 kPa was distributed to three high precision mass flow controllers (MKS Inc., M100B) which were rated to control flow rate to within 1% of the set point and had a total range of 0 to 10 sccm. Two of the flow lines were sent through custom glass solvent bubblers that contained toluene and heptane (VWR, >99.9%) at rates of 0 to 10 sccm. These solvent chambers were placed after the MFCs, to avoid solvent degradation of the MFCs. See Chapter 2 for more details. The solvent annealing was done using liquid solvents held at ambient temperature to minimize the effect of thermal gradients that could occur in the system where the solvent vapor is flowing. These thermal gradients can cause condensation of solvent on the polymer sample unless the polymer sample temperature is at least equal to the solvent temperature.

A 45.5 kg/mol (number average molecular weight) PS-b-PDMS (Polymer Source, Inc. P7517-SDMS, $f_{\mathrm{PDMS}} = 0.32$) BCP which forms a bulk cylindrical morphology with a domain spacing, L_0, of approximately 35 nm was used in this study. Homopolymers of 1390 kg/mol PDMS (100000 cSt Dow Corning 200 fluid) and 1350 kg/mol PS (Polymer Source, Inc. P620-S) were prepared as thin films for comparison. High molecular weights of the homopolymers were used to retard dewetting, because low molecular weight (<15 kg/mol) PS and PDMS dewetted at room temperature in minutes. The SVA system is shown in Figure 4.2 and includes three independently

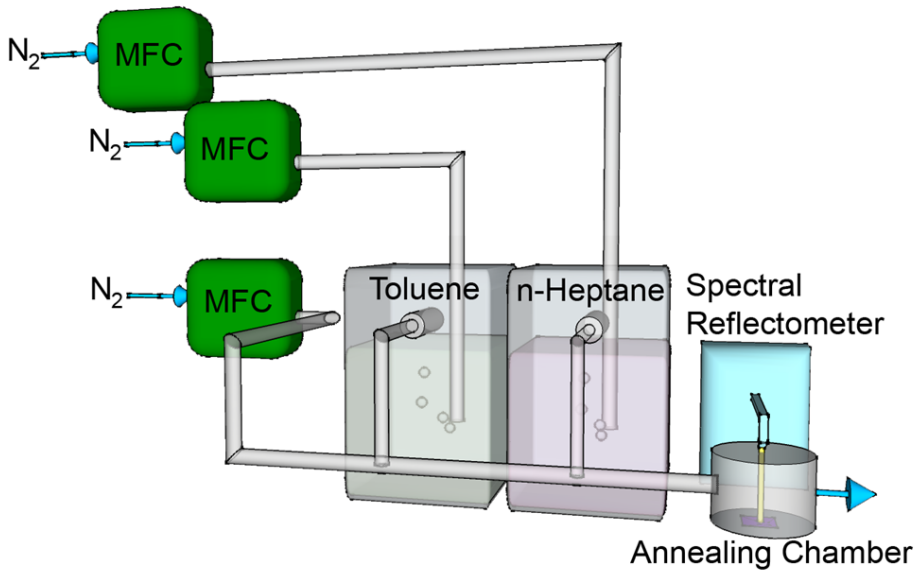

Figure 4-1: A schematic of the flow controlled solvent vapor annealing setup. Thin films of PS, PS-b-PDMS, and PDMS were spun-cast onto Si and were annealed in the chamber while the film swelling was tracked *in situ*.

Table 4.1: Solubility parameters of the solvents and polymers investigated.

Material	Solubility Parameter ($MPa^{1/2}$)
$n-$Heptane	15.3
PDMS	15.5
PS	18.5
Toluene	18.3

controlled vapor streams of saturated toluene, saturated heptane, and N_2. This differs from the reservoir system used in previous work on the same BCP and solvents where liquid mixtures of solvents were placed in a chamber with a small leak[75]. Relevant solubility parameters are given in Table 4.1.

For the BCP films, the substrate was coated with a PDMS brush to improve self-assembly kinetics. The samples were annealed under a range of vapor pressures while the film swelling was monitored *in situ* by spectral reflectometry. The vapor pressures in the chamber reached steady state after 15 min as measured from the changes in magnitude of the absorption peaks of toluene[90] in the UV region with the

spectral reflectometer, and the films were annealed for 1 h at room temperature (25 ± 1 °C). Microphase separation was complete by at most 30 min (shorter times were not examined) but the correlation length of the microdomain array increased if the annealing time was raised to 1 h. The films were quenched by exposure to a burst of N_2 which removed most of the solvent and deswelled the films within 1 s, according to the color change of the film. The BCP thin films were then reactive-ion etched to remove the surface layer of PDMS and then the PS matrix to reveal the underlying morphology of oxidized PDMS microdomains.

4.3 Results and Discussion

Considering the low flow rates of the solvent (<10 sccm), the high solvent evaporation rates, and the large cross-sectional area of the bubbler (>100 cm^2), this allows the assumption that each bubbler delivers solvent vapor at its room temperature saturated vapor pressure, $p^*_{\text{tol}} = 22$ Torr for toluene and $p^*_{\text{hep}} = 40$ Torr for heptane. The partial pressure of solvent i in the chamber is approximated by

$$p_i = p_i^* \left(\frac{q_i}{q_{tol}+q_{hep}+q_{N_2}} \right)$$

where q (mol/min) represents the total molar flow rate of the solvent plus N_2 from the bubbler. Calculations of these partial pressures are plotted as solid blue lines in Figure 4.3 for the case that $q_{\text{tol}}+ q_{\text{hep}} = 10$ sccm while q_{N_2} is allowed to vary from 0 to 20 sccm.

The dashed line shows the vapor pressure above a mixture of liquid toluene plus heptane at room temperature, which approximates the partial pressures available from a solvent anneal process using a liquid reservoir. The toluene/heptane mixture is moderately nonideal[91], and is described by the nonrandom two-liquid (NRTL) model, in which the activity coefficient (γ) of a solvent in a binary mixture is given by

$$ln\gamma_1 = x_2^2 \left[\frac{\tau_{12} e^{-\alpha_{12}\tau_{12}}}{\left(x_2+x_1 e^{-\alpha_{12}\tau_{12}}\right)^2} + \frac{\tau_{21} e^{-2\alpha_{12}\tau_{12}}}{\left(x_1+x_2 e^{-\alpha_{12}\tau_{21}}\right)^2} \right]$$

where (1,2) are the two solvents (toluene, heptane), x is the molar fraction in the liquid, and the coefficients α and τ are determined experimentally[92]. More information

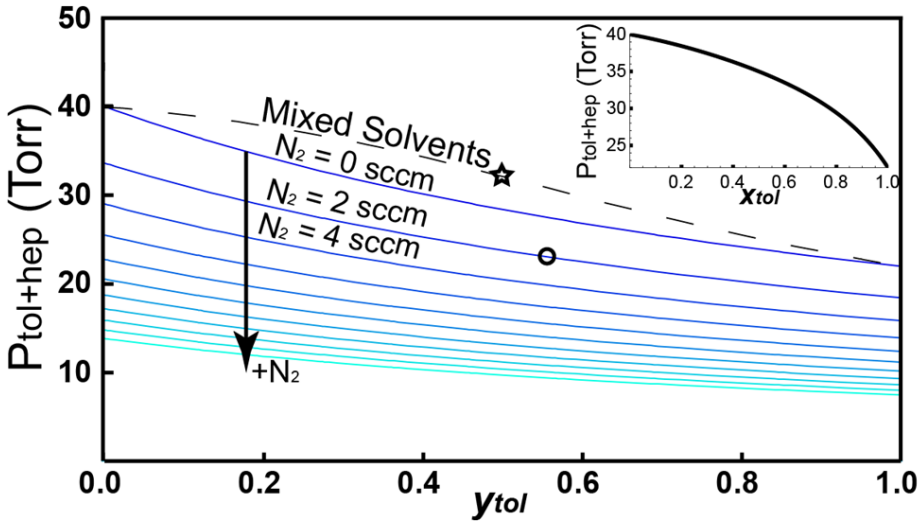

Figure 4-2: The range of cosolvent vapor conditions achievable in the solvent anneal process. The total partial pressure of toluene and heptane is plotted against y_{tol}, the molar fraction of toluene in the toluene plus heptane solvent vapor phase. The solid lines show the conditions achievable with two separate solvent flows ranging from 0 to 10 sccm with incorporation of various additional amounts of N_2. Circle: Example of a condition resulting from 7/3/2 sccm of tol/hep/N_2. The dashed line indicates the vapor pressure conditions available in proximity to a reservoir containing a mixed cosolvent liquid solution at room temperature. Star: Example of condition resulting from a cosolvent mixture where the molar fraction of toluene in the liquid $x_{\mathrm{tol}} = 0.67$. Inset: The relation between total solvent vapor pressure and the fraction of toluene in the liquid phase for a reservoir of mixed solvent, showing a positive deviation from ideality.

about this in shown in the following section. The partial pressure of solvent i is then given by $p_i = \gamma_i x_i p_i^*$. The resulting partial pressures are actually higher than those achieved from the mixing of saturated vapor flows in the annealing chamber of Figure 4.2. While the reservoir system can access these high partial pressures, the mixed-flow system is capable of reaching much lower partial pressures of solvents, which is important for annealing lower-molecular weight BCPs.

In homopolymer/solvent systems the film swelling, given by $\frac{D_0}{D}$ where D is the swollen film thickness and D_0 is the initial thickness, is related to the partial pressure of a solvent and the solventpolymer interaction parameter $\chi_s p$ according to[12]

$$ln\left[\frac{p}{p^*}\right] = \chi_{sp}\left(\frac{D_0}{D}\right)^2 + ln\left[1 - \frac{D_0}{D}\right] + \left(1 - \frac{1}{N}\right)\frac{D_0}{D}$$

where N is the degree of polymerization. This predicts the highest swelling at the saturated partial pressures, but the swelling ratios drop as the partial pressures decrease.

Figure 4.3a gives an example of the swelling of the BCP and the two homopolymer films after 1 h for the case of no N_2 flow, with various flow rates of toluene and heptane vapors, where y_{tol} is the molar fraction of toluene in the toluene plus heptane vapor. Figure 4.3 shows the predicted partial pressures of the solvent vapors under these conditions. At high heptane vapor pressure, the PDMS swelling ratio ($\frac{D_0}{D}$) approached 3 while the PS incorporated very little heptane. Toluene, however, exhibited less selectivity between PS and PDMS, which swelled by a factor of 2.2 and 1.8 respectively. Although toluene would be expected to swell PDMS very little based on the solubility parameters, the very low T_g and high chain flexibility of PDMS allows for a significant amount of toluene incorporation. The swelling ratio of the BCP was intermediate to that of the homopolymers, but was closer to that of PS, the majority block.

Figure 4.3 c shows the swelling ratios of the BCP and the homopolymers over the full range of toluene and heptane partial pressures available at room temperature from the continuous flow system, combined with data from annealing in a chamber containing a reservoir of mixed solvents. The two sets of data show consistent trends. Swelling increased with partial pressure, as expected, and showed a maximum for

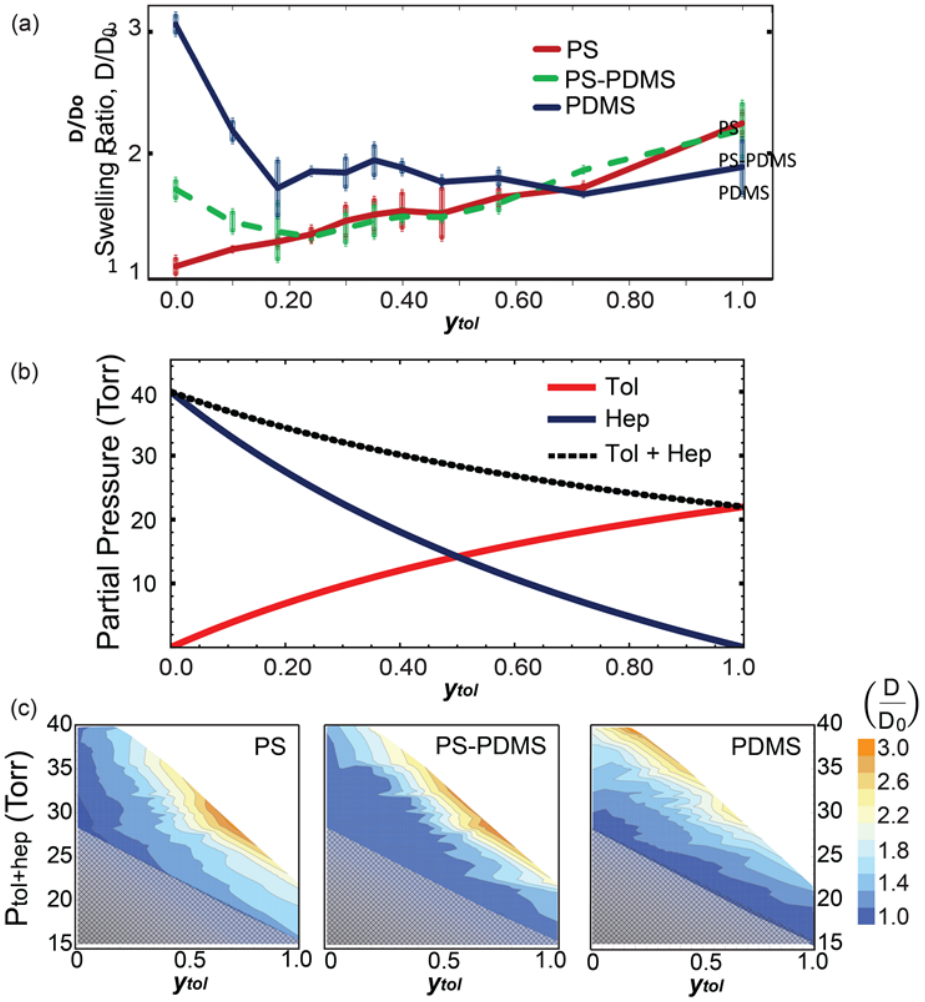

Figure 4-3: (a) Swelling ratios of PS, PS-b-PDMS, and PDMS for different flow rates of saturated toluene and heptane vapors with no additional N_2 diluent (upper horizontal scale). The corresponding mole fraction of toluene in the toluene plus heptane vapor is shown on the nonlinear lower horizontal scale. (b) The expected partial pressures of the solvents based on their flow ratios into the solvent vapor annealing chamber with no additional N_2 flow. (c) Contour plots of the swelling exhibited by the PS, PS-b-PDMS, and PDMS films under different vapor pressure conditions achievable by the controlled flow system and the mixed solvent solution reservoir system. The shaded regions at the bottom left resulted in very little swelling and morphologies were not investigated.

toluene fraction $y_{\text{tol}} < 0.2$ for the PDMS, and $y_{\text{tol}} \approx 0.7$ for the PS and the BCP. The swelling ratios of the polymer films at the upper limit of the vapor pressures achievable with the continuous vapor flow system (i.e., with no diluting N_2 flow) were less than those achievable from the reservoir system for a given $0 < y_{\text{tol}} < 1$, as expected from the nonideality of the liquid mixture.

After annealing, the BCP films were etched to reveal the PDMS microdomain morphology, and a representative selection of images is shown in Figure 4.3 a to i for initial film thicknesses of $D_0 \approx L_0$ and 1.5 L_0. The microdomain morphologies are summarized in Figure 4.3, showing the regimes of vapor pressures within which each morphology formed. In the high vapor pressure regime, films of initial thickness close to L_0 (38 nm) showed a transition from discontinuous in-plane lamellae (with lateral dimensions up to around 10 m) to perforated lamellae to in-plane cylinders of decreasing width and period as y_{tol} increased. The morphology control between perforated lamellae and cylinders was observed previously in samples processed using a reservoir of mixed liquid solvents[13]. However, the lower vapor pressures in the continuous flow system were also able to produce micelles and disordered structures not obtainable from the reservoir anneal. A significant overlap existed between some of the morphologies, especially between in-plane cylinders and lamellae, which formed together on the same substrate.

The thicker films, 1.5 L_0, showed several qualitative differences. Cylinders were formed over a wider range of vapor pressures, lamellae formed less readily, and the perforated lamellar morphology was suppressed. A bicontinuous morphology (Figure 4.3f) and a two-phase voided film caused by solvent aggregation within the film and subsequent removal leading to voids (Figure 4.3h) were found within limited ranges of vapor pressure. In particular, short vertical cylinders of PDMS, Figure 4.3e, occurred when $y_{\text{tol}} > 0.4$ at lower pressures, most likely resulting from a combination of film thickness incommensurability and a reduction in the surface energy difference between the blocks in the solvent atmosphere[93]. Cross sectional images, Figure 4.3i, confirmed the identification of vertical cylinders with an aspect ratio of 1.1. Vertical cylinders and in-plane cylinders coexisted at intermediate vapor pressures but the vertical cylinders

were suppressed as the partial pressure of toluene and heptane increased. To test whether these vertical cylinder structures had a surface layer of PDMS, another sample of the annealed film was etched omitting the first etch step which removes the PDMS layer. This had no noticeable effect on the observed morphology indicating that there is little or no PDMS surface layer under these annealing conditions, suggesting that the solvent vapor reduces the surface energy difference between the blocks. Additionally, the vertical cylinders of PDMS had good close-packed order with correlation lengths on the order of 500 nm. This is different from the micellar structures seen at low vapor pressures and low y_{tol} which had low correlation length and poor uniformity.

Varying levels of osmotic rupture were observed under conditions of high PDMS swelling and low PS swelling where cylinders of PDMS with interior voids were observed (Figure 4g). Osmotic rupture of PS-b-PDMS has been reported previously[94] but the process required full submersion of the BCP film in a PDMS-selective solvent. A two-phase region at high heptane pressure was characterized by voids in the film caused by regions of liquid solvent within the BCP that are removed rapidly during the quench (Figure 4.3h). These results show that the continuous flow system produced a much richer range of microphase-separated structures than the reservoir system, with the perpendicular cylinders being particularly interesting for lithographic applications.

To demonstrate the formation of mixed morphologies, a film was prepared on a substrate with trenches of depth $L_0/2$ such that the thickness was L_0 on the mesas and 1.5 L_0 in the trenches. This was solvent annealed (6:10 sccm flow ratio of Tol:Hep) to produce vertical cylinders with a few in plane cylinders in the trenches, and in-plane lamellae with a few cylinders on the mesas, Figure 4.3j,k.

Self-consistent field theory (SCFT) simulations were performed in order to model morphology changes during SVA. The equilibrium morphology of a film of diblock copolymer AB was modeled in the presence of two different solvents SA and SB, with SA fully selective to block A and SB to B. These simulations used a Langevin dynamics scheme seeded with an initial in-plane cylindrical structure[37,38] to reduce computation time. (The seeding explains why the various simulations of Figure 4.3 have the same cylinder orientation.) The model used $\chi_N = 18.0$ which is less than the

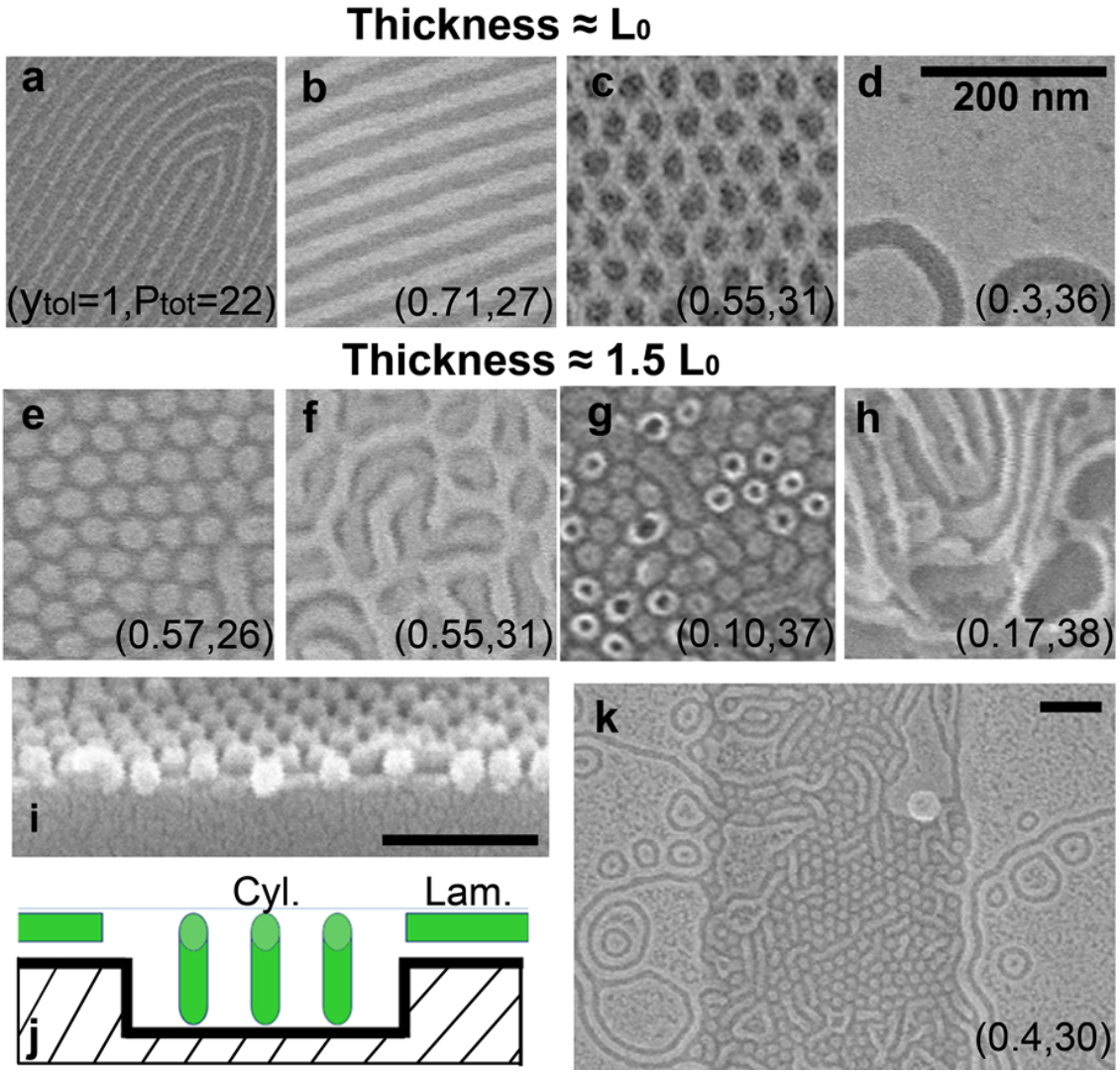

Figure 4-4: A sampling of morphologies seen in different film thicknesses of L_0 and 1.5 L_0 at different SVA conditions (fraction of toluene in vapor, total vapor pressure (Torr), is labeled on each image): (a,b) in-plane cylinders with different widths; (c) perforated lamella; (d) lamellae of limited width; (e) vertical cylinders; (f) bicontinuous; (g,h) two-phase coexistence of solvent and polymer which results in film voids of varying size upon quenching; (i) cross section of vertical cylinder formation; (j) schematic of self-assembly of a film deposited on a substrate with trenches; (k) experimental results of the experiment shown in image j, with vertical cylinders in the 1.5 L_0 thickness film in the trench and lamellae in the L_0 thickness film on the mesa.

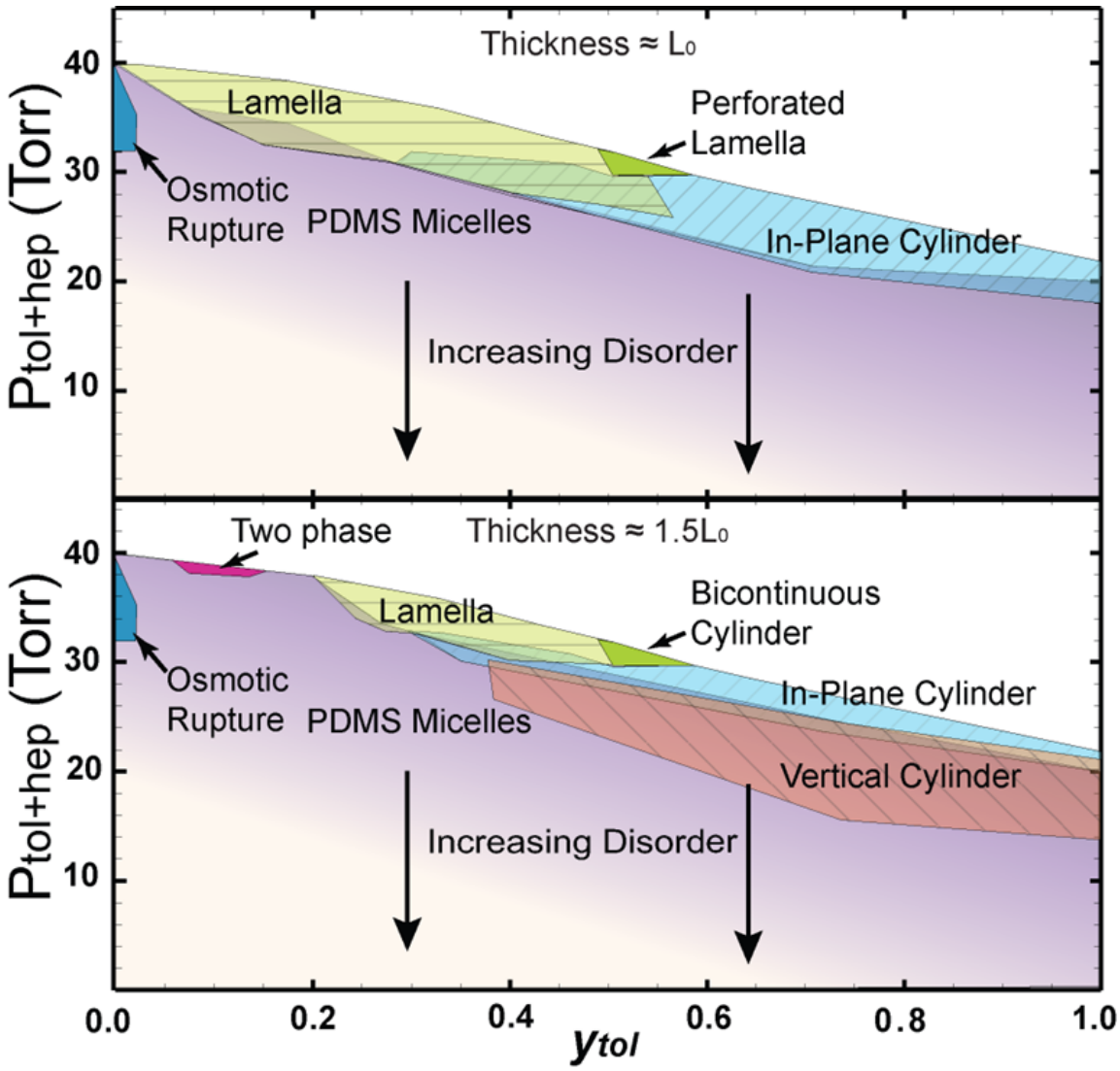

Figure 4-5: A phase diagram of the morphologies produced by solvent vapor annealing a 45 kg/mol PS-b-PDMS (f_PDMS = 0.32) film under different partial pressures of toluene and heptane at room temperature. BCP film thicknesses of L_0 (upper panel) and 1.5 L_0 (lower panel) were explored. At low solvent vapor pressures the BCP was kinetically trapped in the PDMS micelle morphology that formed during spin coating, and its ordering (i.e., the correlation length of the micelle array) improved as the vapor pressure increased.

χ_N of 100 that is expected in the PS-b-PDMS experimental system (which has $N \approx 485$) at room temperature without solvent incorporation. A lower χ_N was used because the statistical repeat unit (used in the simulations) is 2.8 times larger than a single experimental chemical monomer at the level of coarse-graining used, and because solvent incorporation is known to reduce the effective χ[82,83]. Solvent incorporation was modeled explicitly through the partitioning of the solvent as a monatomic fluid in addition to the traditional single chain partitioning of the block copolymer and implicitly through the choice of a lower χ value, and swelling evolution was modeled by keeping the overall copolymer volume constant during the addition of solvent volume.

The model showed that the density profile of SA closely overlapped the density profile of block A, and SB overlapped B. Within this formalism, toluene, which experimentally showed an almost neutral selectivity between PS and PDMS, would be modeled as a superposition of two different fully selective solvents with fractional amounts determined from the measured incorporation of toluene into each of the blocks.

The results of the simulations are shown in Figure 4.3. Each simulation bar one started with the same initial configuration of in-plane cylinders for $f = 0.32$ in a cell of dimensions 3 L_0 by $2\sqrt{3}L_0$ (commensurate with cylinders or a hexagonally packed perforated lamella) with periodic boundary conditions, then the simulation cell thickness was increased and the empty volume filled with SA and SB, and allowed to equilibrate. The initial thickness D_0 was chosen by simulating a range of film thicknesses to find the range that produced a monolayer of in plane cylinders. Swelling was modeled by increasing the cell thickness sequentially by one grid point, at the level of coarse-graining used. The ratio SA/(SA + SB) was varied from 50% to 100%, where A represents the minority block. The 50% ratio approximates pure toluene assuming toluene to be entirely neutral in its swelling of PS and PDMS, while the 100% ratio approximates annealing in pure heptane. Perforated lamellae were defined as states with a connection between neighboring in-plane cylinders while lamellae occurred when the entire plane of cylinders of minority polymer density connected.

As the solvent became more selective to the minority block, that is, increasing SA/(SA + SB), the morphology transitioned from narrow cylinders to wider cylinders to perforated lamellae and then to lamellae. This agrees qualitatively with the experiment, where the narrow cylinder-wide cylinder-perforated lamellalamella sequence occurs with increasing heptane (preferential to PDMS). The model also suggests that higher swelling (i.e., higher vapor pressure) for a given SA/(SA + SB) favors cylinders over lamellae, because proportionately more of the minority-selective solvent is required to increase f into the lamellar regime. In agreement, comparing Figure 4.3b for the BCP and the upper panel of Figure 4.3, the highest swelling ratios corresponded to cylindrical morphologies. Considering that adding solvent SA has the effect of increasing f_A, these trends are comparable to other studies relating BCP morphology to f. The agreement between the observed and modeled morphological transitions suggests that the drying of the swollen film was fast enough to preserve the morphology present during the solvent anneal as has been suggested for thin films[78]. The simulation did not generate the perpendicular cylinder morphology, presumably due to the preferential wetting of the top surface by the minority block in the simulation, and because the swelling ratios modeled were smaller than those which generated perpendicular cylinders.

4.4 Non-Random Two Liquid Model

The non-random two liquid model (NRTL) model can accurately describe activity coefficients for liquid mixtures of binary solvents which allows for the calculation of partial pressures:

$$p_1 = \gamma_1 x_1 p_1^*$$

where p_1 is the partial pressure of component 1 which has a saturated partial pressure in its pure state of p_1^*, x_1 is the mole fraction of component 1 in the liquid mixture, and $_1$ is the activity coefficient of component 1. The NRTL equations are shown in Table 4.2. For the toluene and n-heptane binary system used in this thesis, the NRTL constants are shown in 4.3.

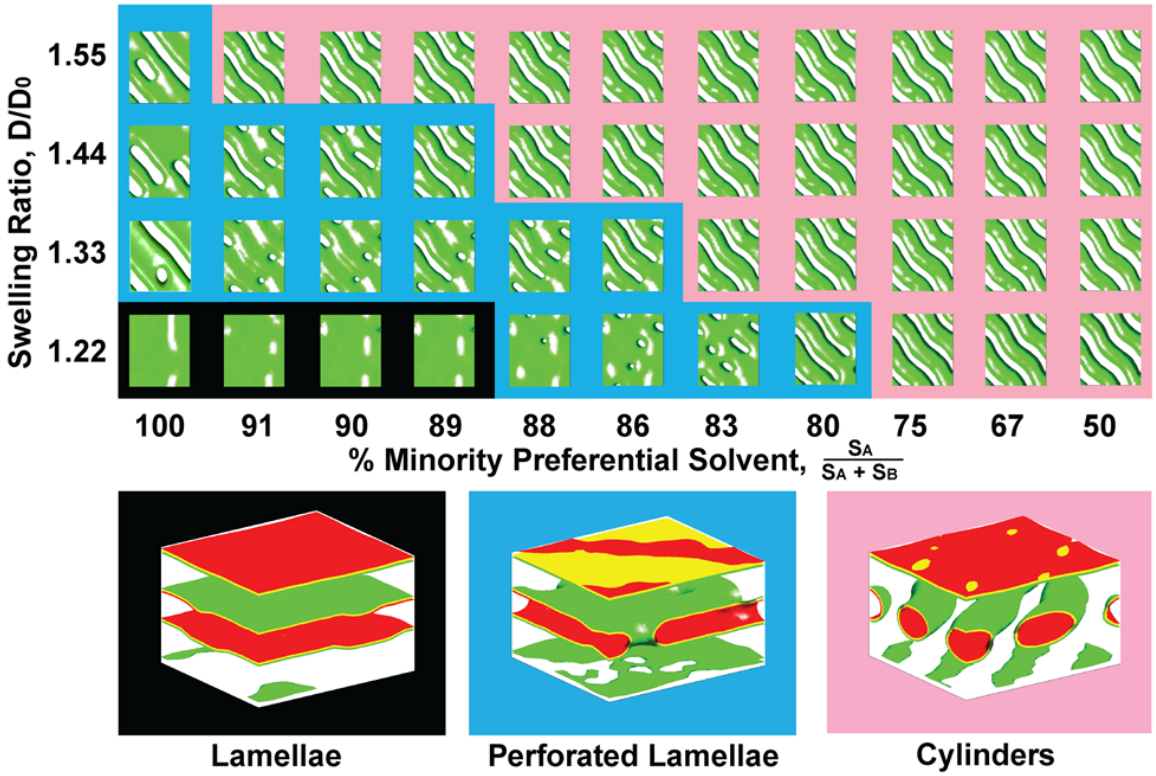

Figure 4-6: SCFT simulations of a cylinder phase BCP (f = 0.32, $\chi_N = 18.0$) thin films ($D_0 = 1.7\ L_0$) with varying volume expansions D/D_0 caused by the incorporation of solvents selective to each block A and B. The images show the isosurface in green at which the density of the minority polymer plus its solvent SA was $\varphi = 50$. In the representative lower 3D images, additional surfaces are shown for $\varphi = 60$ (yellow) and 70 (red). The green isosurface is shown as a reflective surface to give an idea of its flatness. In images with a black background, the minority block forms a lamella without any perforations; blue background indicates a perforated lamella or bridged cylinders, and a pink background indicates separated cylinders.

Table 4.2: The non-random two liquid (NRTL) equations

$ln\gamma_1 = x_2^2\left(\frac{\tau_{12}e^{(-\alpha_{12}\tau_{12})}}{(x_2+x_1e^{(-\alpha_{12}\tau_{12})})^2} + \frac{\tau_{21}e^{(-2\alpha_{12}\tau_{21})}}{(x_1+x_2e^{(-\alpha_{12}\tau_{21})})^2}\right)$	$\tau_{21} = \left(\frac{1}{RT}\right)(C_1 + D_1(273.15 - T))$
$ln\gamma_2 = x_1^2\left(\frac{\tau_{12}e^{(-2\alpha_{12}\tau_{12})}}{(x_2+x_1e^{(-\alpha_{12}\tau_{12})})^2} + \frac{\tau_{21}e^{(-\alpha_{12}\tau_{21})}}{(x_1+x_2e^{(-\alpha_{12}\tau_{21})})^2}\right)$	$\tau_{12} = \left(\frac{1}{RT}\right)(C_2 + D_2(273.15 - T))$
	$\alpha_{12} = C_3 + D_3(273.15 - T)$

Table 4.3: The NRTL constants for the toluene + heptane binary solvent mixture.

$C_1 = -690.2$	$D_1 = 2.903$
$C_2 = 2188.3$	$D_2 = -9.478$
$C_3 = 0.3$	$D_3 = 0$

4.5 Summary

Solvent annealing using continuous flows of saturated solvent vapors and an inert gas diluent can access regimes of solvent partial pressure which are not available from a simple solvent anneal system that uses a reservoir of mixed liquid solvents, in which nonidealities in cosolvent mixtures govern the available partial pressures of the solvents. The independent control of vapor pressures in the continuous flow system provides a powerful and general method for mapping the swelling ratio and morphology as a function of the partial pressures of the solvents, and provides access to a wide variety of morphologies from a block copolymer. For example, perpendicular cylinders were demonstrated in 45 kg/mol PS-b-PDMS which are inaccessible from a reservoir anneal. Further, a continuous flow system can provide low vapor pressures of solvent which are necessary for microphase separation in low molecular weight BCPs required for small period patterns without dewetting or formation of two-phase structures. Self-consistent field theory modeling of solvent incorporation showed morphological transitions that correspond qualitatively to the experiment. Morphology control, including manipulation of periodicity, critical dimension and geometry, are critical for the application of BCPs to nanolithography, and solvent annealing is a key enabling process step. The continuous flow solvent anneal system can be adapted to include larger numbers of solvent vapor streams, which may be appropriate for triblock terpolymers or other more complex polymers. The next chapters take the knowledge gained from SVA shown here and in Chapter 2 and applies to templated self-assembly whereby top down electron beam lithography is used to create precise boundary conditions to guide the self-assembly of BCPs.

Chapter 5

Templated Self-Assembly

This chapter describes the work done on templated self-assembly utilizing solvent vapor annealing. SVA was required for these studies for a variety of reasons. Firstly, PS-PDMS is a high-χ BCP system which have high barriers for diffusion[10,11,95]. These diffusion barriers depend additionally on the minority block fraction with higher block fractions resulting in higher diffusion barriers. In our past work[9], thermal annealing was sufficient for sphere forming PS-b-PDMS, but was untenable for the larger MW cylinder forming 45 kg/mol PS-b-PDMS used in this chapter. Additionally, for the 3D self-assembly explored below, thermal annealing was found to not result in this structure hinting at complex dynamics during the self-assembly process that are only beginning to be understood and are discussed in Chapter 6.

5.1 Enforcing Rectangular Symmetry

5.1.1 Introduction

Templated self-assembly of block copolymer (BCP) thin films can enhance the resolution and throughput of nanoscale lithography processes. This method has been used to produce large-area defect-free lamellar, cylindrical, or spherical microdomain patterns through chemical[7,8,32,96–98] or topographical[6,16,22,36,55,99–101] templating. However, the formation of complex patterns with multiple morphologies in one BCP film (e.g.,

coexisting cylinders and spheres) requires additional process steps such as sequential cross-linking and solvent anneals[55,102]. The period of the patterns is determined by the BCP chain length, and sub-10-nm-period (sub-5-nm half-pitch) patterns have been reported from low molecular weight BCPs.[6] While a hexagonal lattice of microdomains is readily obtained from a diblock copolymer, obtaining a square symmetry pattern requires 1:1 templating of a diblock copolymer,[33] or use of a triblock terpolymer,[55] or a blend of diblock copolymers[103]. This work shows that by using an array of majority-block-functionalized posts, it is possible to locally control the morphology of a diblock copolymer, achieve several morphologies simultaneously on a single substrate, and create patterns with square or rectangular symmetry. As a side benefit of this method, because the topographic template features are incorporated into the final pattern, the resulting spacing between the template features and the minority microdomains is smaller than the BCP period, i.e., the areal density of features is increased. Three-dimensional self-consistent-field-theory (SCFT) simulations were performed to calculate equilibrium morphologies and to explore a wider parameter space than that of the experiments. The following section describes detailed experimental methodology for achieving these results.

5.1.2 Experimental Methods

Template Fabrication: The templates were fabricated by EBL of HSQ (Dow Corning XR-1541 2% solids), a negative-tone electron resist. HSQ was spin-coated on Si (100) wafers at different thicknesses (21 nm, 27 nm, and 38 nm) depending on the BCP being used. The thickness of the spin-coated HSQ was measured using an ellipsometer. A Raith 150 EBL tool at 30 kV acceleration voltage and 300 pA beam current was used for the exposure of the resist. Arrays of HSQ posts with diameters ranging from 10 nm to 30 nm (measured by image processing software) were obtained by using different doses ranging from 10 fC to 70 fC. After exposure, samples were developed in a salty developer for 4 minutes followed by a rinse in de-ionized water for 2 minutes. Subsequently, O_2 plasma asher (50 W, 0.35 Torr) was used to remove possible organic residues and to change the HSQ patterns to silica.

Block Copolymer Self-assembly: The templates were chemically functionalized with a hydroxyl-terminated PS brush (3 kg/mol and 1 kg/mol for high and low molecular weight of BCPs, respectively) by first spinning the PS solution onto the templates and then placing them in a vacuum oven (∼20 Torr) at 170 °C for 16 hours and subsequently rinsing with toluene to remove ungrafted polymer chains. Then poly(styrene-b-dimethylsiloxane) (PS-b-PDMS) (high MW: 45.5 kg/mol, $f_{\mathrm{PDMS}} = 32\%$ or low MW: 16 kg/mol, $f_{\mathrm{PDMS}} = 31\%$) was spun onto the HSQ templates to a thickness of 29 nm or 25 nm, respectively. Annealing of the high MW BCP thin film was done by placing the samples in a chamber in the presence of a cosolvent vapor resulting from a mixture of heptane and toluene liquids ($V_{\mathrm{tol}}/V_{\mathrm{hep}} = 5$) which swelled both blocks of the copolymer and improved the kinetics of self-assembly. After 3 h anneal followed by quenching in air and etching, the film period was around 35 nm. For the low MW BCP, a saturated vapor of acetone was used in a closed dish for 5 h resulting in a BCP period of around 17 nm. A 5 s (high MW) or 2 s (low MW) CF_4 RIE (50 W, 15 mTorr) was done to remove the top PDMS surface wetting layer, immediately followed by a 22 s (high MW) and 12 s (low MW) O_2 RIE (6 mTorr, 90 W) to remove the PS matrix and leave the ox-PDMS patterns. Scanning electron micrographs (SEMs) were obtained using a Raith 150 scanning electron microscope operated with an acceleration voltage of 10 kV.

Simulation Methods: Using the same methods as presented by Mickiewicz et al[42], three-dimensional SCFT simulations were done to compare the equilibrium morphologies found in the experiment with those in the simulations. The simulations were used to explore a wider parameter space than allowed in the experiments in order to predict the commensurability conditions for the various morphologies. In the simulations, the system was modeled using three dimensional unit cells with periodic boundary conditions in the x- and y-directions. The posts were modeled by constraining the fields in the region of the posts to a large value that prevents polymer density from evolving in that region. The brush layer was modeled using a field constraint around the boundary of the post region that was attractive to the majority block (PS) and repulsive to the minority block (PDMS). The top air interface

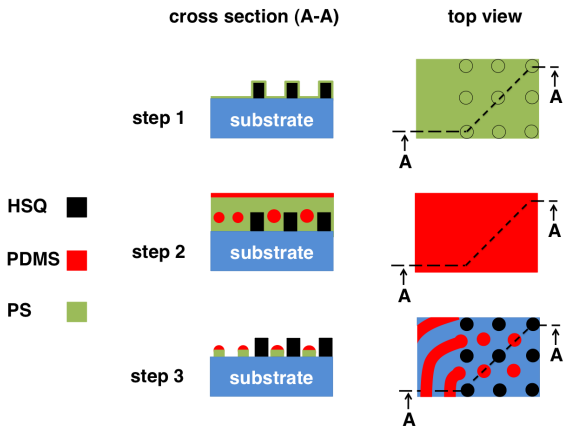

Figure 5-1: Schematic diagram showing the major steps of the fabrication process. Step 1: defining the post template by EBL and chemically functionalizing with a PS brush; step 2: spin-coating and annealing of the BCP; step 3: removing the PDMS top wetting layer by CF_4 RIE and then the PS matrix by O_2 RIE, then imaging in SEM. The height of the oxidized PDMS cylinders in step 3 is expected to be lower than that of the as-annealed PDMS cylinders in step 2 due to the etch process.

was modeled similar to the brush layer but preferentially attractive to the PDMS as experimental observation shows PDMS to have a lower surface energy with air than PS. To match experimental parameters, the model used a value of $\chi_N = 30.0$ and $f_{\mathrm{PDMS}} = 0.32$ where N in the simulation is the number of coarse-grained statistical monomers. The system was evolved starting with random initial field conditions until a saddle point solution to the field equations was obtained that was either an equilibrium or metastable morphology.

5.1.3 Results and Discussion

Figure 5.1.3 shows a schematic diagram of the major steps of the experimental method. In the first step, the templates were fabricated by means of electron-beam-lithography (EBL) exposure of hydrogen silsesquioxane (HSQ) resist, then chemically functionalized with the majority-block brush, hydroxyl- terminated-polystyrene by grafting the hydroxyl-terminated ends onto the silica substrate. Next, poly(styrene-b-dimethylsiloxane) (PS-b-PDMS, 45.5 kg/mol) was spin-coated onto the template substrates. The BCP used in this experiment had a bulk morphology consisting of

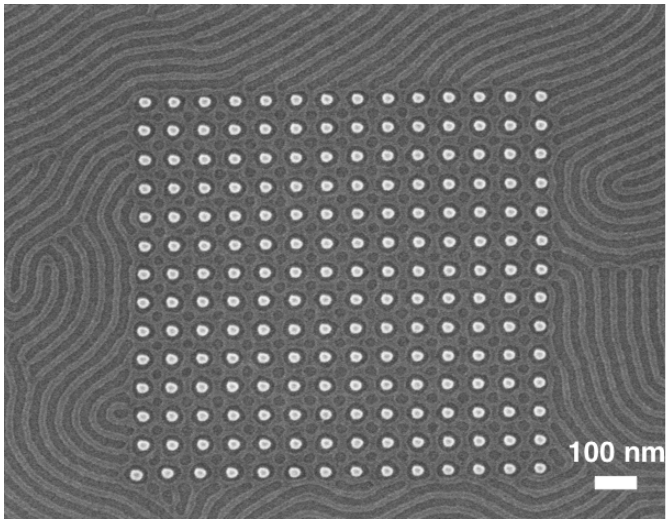

Figure 5-2: SEM of a hybrid BCP pattern on a substrate. White and light grey shades represent HSQ and ox-PDMS, respectively. Inside the templated region, the ox-PDMS formed a perforated lamella and outside of it, it formed cylinders.

PDMS cylinders in a PS matrix with an equilibrium periodicity of ∼35 nm. Annealing of the BCP thin film was done at room temperature using solvent vapor. A CF_4 reactive-ion etch (RIE) was done to remove the top PDMS surface layer and immediately followed by an O_2 RIE to remove the PS matrix and leave the oxidized-PDMS (ox-PDMS) patterns on the substrates.

Figure 5.1.3 shows a scanning electron micrograph of a hybrid BCP pattern on a substrate. The square array of PS-functionalized posts had 27-nm diameter and 73-nm period in both the x- and y-directions. Two different BCP morphologies, cylinders outside the template region and a square symmetry perforated lamella within it, appeared on the substrate.

By using different template conditions, other morphologies could be achieved. Figure 5.1.3 a-h shows SEMs of the morphologies of the BCP for different post periods. By varying the post period from less than L_0 (the equilibrium BCP period) to more than 2 L_0, different morphologies were observed, such as cylinders (Figure 5.1.3a,h), undulated cylinders (Figure 5.1.3b), spheres (Figure 5.1.3c), ellipsoids (Figure 5.1.3d), periodic superstructures (Figure 5.1.3e), perforated lamellae with a perforation at each post (denoted by L1) (Figure 5.1.3f) and perforated lamellae with additional

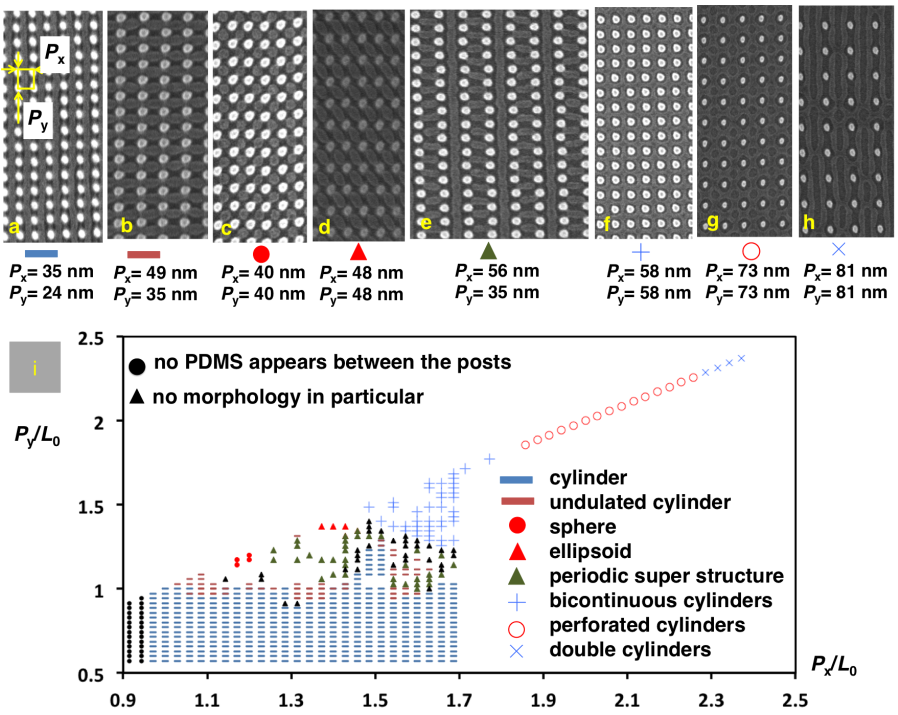

Figure 5-3: a-h) SEMs of different morphologies of PDMS microdomains. The HSQ appears white and the ox-PDMS light grey. The observed morphologies are: a) cylinders, b) undulated cylinders, c) spheres, d) ellipsoids, e) periodic superstructures, f) perforated lamellae L1, g) perforated lamellae L2, h) double cylinders. i) A phase diagram showing a summary with each data point representing one sample. j) Phase diagram using 3D SCFT modeling. The horizontal axis is the reduced post spacing distance in the x-direction P_x/L_0 and the vertical axis is the reduced post spacing distance in the y-direction P_y/L_0. The structures are shown from the top after removing the PDMS surface layer, with only the $\phi = 0.5$ surfaces shown in green. k) 3D SCFT simulation results showing contours of $\phi = 0.5$ (green), 0.6 (yellow) and 0.7 (red), where ϕ represents the normalized density of the PDMS.

perforations between the posts (denoted by L2) (Figure 5.1.3g). Most of these morphologies were observed at a particular post period in the x- and y-directions; as the period varied around these values, the uniformity of the structures decreased. The periods where each of these morphologies occurred depended on the post diameters. Figure 5.1.3i shows the experimental phase diagram plotted against post period Px and Py varying from 0.5 L_0 to 2.5 L_0 for a post diameter of 10 nm to 20 nm. We label Py as the smaller period in rectangular lattices. In this figure, each data point represents a sample in which one morphology covering more than 70% of the templated area. A black triangle represents a sample with no dominant morphology.

SCFT was used to model the morphology resulting from post periods of 0.7 L_0 to 2.0 L_0. A phase diagram of the simulation results is shown in Figure 5.1.3j. The general trends of the simulations showed the same morphologies observed in experiments, including cylinders (yellow region in Figure 5.1.3j), spheres (blue region in Figure 5.1.3j), ellipsoids (green region in Figure 5.1.3j), perforated lamellae L1 (pink region in Figure 5.1.3j), and L2 (orange region in Figure 5.1.3j), all near the same post period ranges seen experimentally. The simulations can yield both equilibrium and metastable structures, so if the model results differed from those observed experimentally, multiple simulations were performed to determine the energy minimum. The phase diagram shows the state with lowest energy. Additional larger unit cell simulations were done with a post period of Px = Py = 2.29 L_0 for comparison with Figure 5.1.3h. The simulations showed that both L2 and double cylinders had similar energies for these post periods (inset image in Figure 5.1.3j).

The simulations assume periodic boundary conditions, whereas the real systems have a finite post lattice area and the equilibrium cylinder structures surrounding the post lattice boundaries might influence the morphologies in the templated region. Also, the simulation does not address local film thickness changes caused by solvent annealing, and since the simulations only yield saddle point solutions and do not reproduce realistic kinetics, these structures will not correspond exactly to the experiment in cases where kinetically trapped structures form. Despite this, the simulations give a very good qualitative agreement with the experiment, and could therefore be predictively useful.

Two major discrepancies occurred between the model and experiment. First, in cases where experimentally the cylinders oriented parallel to the axis with larger period with Px $> L_0$ and Py$< L_0$, the model predicted that this was a higher energy state than alignment parallel to the axis with smaller period. Second, the model could not reproduce the superstructures because it included only one lattice period.

We now describe the various morphologies in more detail. When Px was similar to or greater than L_0 and Py $< L_0$, the PDMS cylinders oriented along the y-direction, Figure 5.1.3a. The cylinders in the templated region showed a small amount of necking or undulation near the posts, and a different width compared to those in the untemplated region: when Px $> L_0$ the width of the cylinders was larger than the untemplated case. When Px was similar to or greater than L_0 and Py $= \sim L_0$, the PDMS cylinders oriented along the x-direction, Figure 5.1.3b. The cylinders showed distinct undulations caused by the PS-coated posts. These cylinder morphologies occurred over a wide range of Px in both experiment and model. The SCFT examples in Figure 5.1.3j show only small fluctuations in the cylinder width, but cylinders with larger undulations oriented along the commensurate direction appeared for shorter or thinner posts or a thicker BCP film.

Figure 5.1.3c shows a spherical morphology with a square symmetry that occurred when Px = Py and the post period was incommensurate with L_0. By increasing the post period in both directions, a condition was reached in which the BCP was commensurate with the lattice under a rotation of 45 degrees, which resulted in an elliptical morphology for the PDMS, as seen in Figure 5.1.3d. Figure 5.1.3i shows that the simulated spherical and ellipsoidal morphologies occurred within a small range of post periods, and the ellipsoidal structures were oblate ellipsoids rather than the 45-degree-oriented prolate ellipsoids observed in the experiment. The higher symmetry in the simulation may result from the periodic boundary conditions which do not provide a preferential in-plane direction for the ellipsoids to orient.

Figure 5.1.3e shows a periodic superstructure of cylinders and ellipsoids. Periodic superstructures of cylinders and ellipsoids or cylinders and spheres were observed within a large region of post periodicity, in between template periods that generated

either cylinders or perforated lamellae, as shown in Figure 5.1.3i. These superstructures appear to be metastable combinations of the ellipsoidal and cylindrical morphologies. Such periodic patterns were only produced in SCFT simulations of double cells in which one of the cells was seeded with initial conditions consisting of a sphere of PDMS. The simulations suggest that spheres or ellipsoids have similar energies to cylinders (cylinders have a slightly higher energy) in this regime of post period, and this indicates that the superstructure represents a combination of these states. Formation of a cylinder may promote formation of ellipsoids in the adjacent unit cells, which then favors formation of another cylinder, etc., building up the superstructure. Energy differences between the superstructure and cylinder-only morphologies are small, for example the superstructure had 0.034% higher energy for Px = 1.0 L_0 and Py $\sim$ 1.5 L_0 in the simulations.

Figure 5.1.3f shows a perforated lamellar morphology L1 which occurred when the post periods in the x-, y-, and diagonal directions were between L_0 and 2 L_0. The volume of the ox-PDMS between the posts was intermediate between that of one cylinder and two cylinders.

Figure 5.1.3g shows perforated lamellae with additional perforations between the posts (L2) which formed for Px = Py = 1.8-2.3 L_0; for larger period, the structure transitioned to pairs of cylinders lying between the posts, Figure 5.1.3h. The SCFT simulations showed perforated lamellae L2 for Px = Py $>$ 1.7 L_0, but the model did not reproduce the gradual transition between morphologies. Larger multi-cell simulations may show such transitional structures. Larger unit cells (e.g. Px = Py = 2.29 L_0) generated either double parallel cylinders or perforated lamellae L2, Figure 5.1.3j (inset), and these two structures had degenerate energies.

Considering that both the HSQ template features and the ox-PDMS are silica-based structures with high etch resistance, they both constitute the final pattern produced by the templated BCP. The areal density of HSQ plus ox-PDMS features in the final pattern was therefore higher compared to the density of ox-PDMS features in an untemplated film. For example, the feature spacing along the x-axis in Figure 5.1.3a, or the y-axis in Figure 5.1.3b, is 17 nm, half of L_0. This process therefore achieves

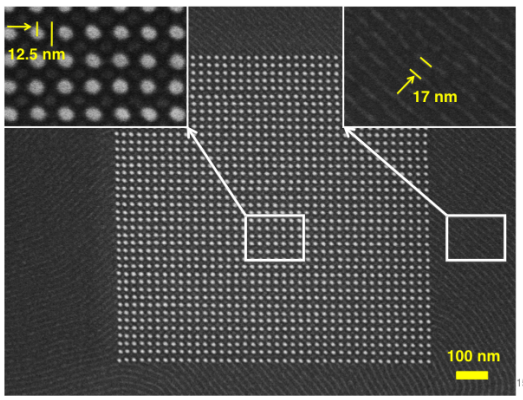

Figure 5-4: SEM of a high-resolution hybrid BCP pattern on a substrate. White and light grey colors represent HSQ and ox-PDMS, respectively. In the template region, ox-PDMS microdomains are spheres and outside of it, they are cylinders.Insets: Zoomed-in images of areas inside and outside the template.

not only control over the film morphology and formation of square and rectangular symmetry patterns, but a denser set of etch-resistant features than is possible from the BCP alone.

The morphological control was further illustrated by templating a PS-b-PDMS BCP with low molecular weight (16 kg/mol). This material formed in-plane cylinders with spacing 17 nm on a smooth substrate, but a square array of posts with 25 nm period templated a square symmetry pattern of ox-PDMS spheres between the posts, Figure 5.1.3. The ox-PDMS spheres and the posts together formed a square pattern with feature spacing of $25/2 = 17$ nm, similar to Figure 5.1.3c but smaller in dimensions.

We next show how the size of the ox-PDMS microdomains can be predicted analytically based on the geometry of the template and volume fraction of the BCP. Consider first a film, which forms a single layer of cylindrical PDMS microdomains with radius R0 on a smooth substrate. When templated into spherical microdomains of radius Rs by an array of posts (as in Figure 5.1.3c or 5.1.3),

$$R_s = \left(\frac{3R_0^2}{4L_0} \left[P_x P_y - \pi (r+T)^2 \right] \right)^{\frac{1}{3}}$$

where r is the radius of the posts, and T the thickness of the PS brush layer on the posts.

For the case of a bilayer BCP film which forms two layers of cylinders on a smooth substrate, if R_{01} and R_{02} are the radii of the ox-PDMS cylinders in the top and bottom layers of microdomains, then in cases where post templating forms a monolayer of spheres of radius Rs,

$$R_s = \left(\frac{3\pi\left(R_{01}^2+R_{02}^2\right)}{4L_0} \left[P_x P_y - \pi(r+T)^2\right] \right)^{\frac{1}{3}}$$

These results show that the radius R_s of the templated spherical PDMS microdomains depends on both the volume fraction of PDMS (which determines R_0 for a given L_0) and the geometry of the template. Figure 5.1.3a-c shows the experimental verification of this analysis for three different conditions, in which different post geometries, film thicknesses and molecular weights (45 kg/mol and 16 kg/mol) are used. Figure 5.1.3a shows a film consisting of a monolayer of cylinders on a smooth substrate, and Figures 5.1.3b and 5.1.3c are from bilayers of cylinders. In Figures 5.1.3a-c, the square post lattice yielded PDMS spheres whose predicted diameters from equations shown above were 24 nm, 11 nm and 31.5 nm respectively, which compares well with the measured values of 24 nm, 11 nm, and 32 nm. The agreement supports the interpretation of the templated morphologies as consisting of a monolayer of PDMS spheres, consistent with the SCFT model.

5.1.4 Summary

The central result in this section is the use of an array of majority-block-functionalized topographical posts to control the self-assembly of a BCP, allowing a variety of morphologies to be produced, including arrays of spheres, ellipsoids, cylinders, undulating cylinders, perforated lamellae, and superstructures, by varying the geometrical parameters of the post array which is enabled by an understanding of the solvent vapor annealing of higher minority block fraction PS-b-PDMS. This understanding of the effects of the SVA assisted self-assembly of a monolayer of BCP in an array of posts functionalized with minority block PS help lay the foundations for enabling bilayer self-assembly as discussed in the next section.

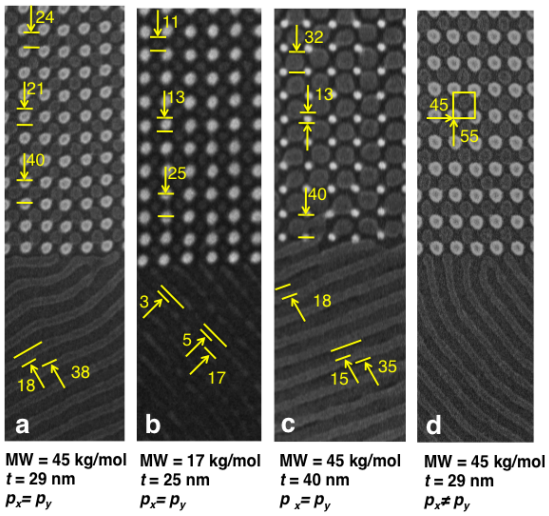

Figure 5-5: SEMs illustrating the change of the morphology of ox-PDMS cylinders to spheres using a PS-functionalized template. White and light grey colors indicate HSQ posts and ox-PDMS microdomains, respectively. The unit of numbers in all images is nm and a square lattice template was used for images (a-c). These images are the results of: a) a single layer BCP with a molecular weight of 45 kg/mol, b) a bilayer BCP with a molecular weight of 16 kg/mol, c) a bilayer BCP with a molecular weight of 45 kg/mol, and d) a single layer BCP with a molecular weight of 45 kg/mol and a rectangular lattice template.

5.2 3D Self-Assembly

5.2.1 Introduction

The registration and alignment of a monolayer of microdomains in a self-assembled block copolymer thin film can be controlled by chemical or physical templating methods. Although planar patterns are useful for nanoscale device fabrication, three-dimensional multilevel structures are required for some applications. This section shows that a bilayer film of a cylindrical-morphology block copolymer, templated by an array of posts functionalized with a brush attractive to the majority block, can form a rich variety of three-dimensional structures consisting of cylinder arrays with controllable angles, bends, and junctions whose geometry is controlled by the template periodicity and arrangement and their formation is enabled through the use of solvent vapor annealing. The following section explains the experimental methods used in details to achieve this.

5.2.2 Experimental Methods

Template fabrication. The templates were fabricated by using electron-beam lithography (EBL) of HSQ (Dow Corning XR-1541 2 solids), a negative-tone electron resist. HSQ has several advantages such as high resolution, high etching resistance, and easy imaging of its patterns by a scanning electron microscope without using a conductive coating. The last advantage is useful for checking the templates before the self-assembly of the BCP patterns. HSQ was spin-coated at 40 $\pm$ 2 nm thickness (determined by ellipsometry) on Si substrates. Sample sizes were typically around 2 cm squares obtained by cleaving Si (100) wafers. The resist was exposed in a Raith 150 EBL tool at 30-kV acceleration voltage, 300-pA beam current, 40-fC to 116-fC dot doses and 0.13-ms to 0.39-ms dot-dwell-time to obtain arrays of HSQ posts. After exposure, samples were developed in a high-contrast salty developer[36] of 4 NaCl and 1 NaOH in DI water at room temperature for 4 min followed by a rinse in de-ionized water for 2 min and drying with N_2 gas. The samples were further treated with an

O_2 plasma asher (50 W, 0.35 Torr) for 2 min to remove possible organic residues and to convert the HSQ patterns to silica. The height of HSQ posts after exposure and O_2 plasma was less than the initial thickness of the HSQ resist. The decrease in the thickness of the HSQ resist after exposure and O_2 plasma is about 20% of the initial film thickness.

Block copolymer self-assembly. After fabrication, the templates were chemically functionalized with a hydroxyl-terminated-PS brush (1 kg mol−1, PolymerSource) by first spinning the PS-OH solution onto the templates and then placing them in a vacuum oven (20 Torr) at °170 C for 16 h and subsequently rinsing with toluene. Then, PS-b-PDMS (45.5 kg/mol, $f_{\mathrm{PDMS}} = 32$) was spin-coated onto the substrates with the HSQ templates to a thickness of 42 ± 1 nm (measured using spectral reflectometry). PS-b-PDMS was chosen for its high Flory-Huggins interaction parameter (χ is approximately 0.226 at 25 °C) and its ability to act as a robust etch mask[7]. Solvent annealing was done using a crystallization dish geometry (5 cm diameter, 1.5 cm height) where the substrates were placed on a glass platform 0.6 cm from the base of the crystallization dish. 1.5 ml of a toluene and heptane mixture with a 5:1 volume ratio of toluene:heptane (toluene mole fraction = 0.874) was placed in the chamber and the chamber was capped by placing a 10-cm diameter glass petri dish over it. This toleuene/heptane mixture has been shown to correspond to toluene and heptane partial pressures of 19.5 Torr and 7.8 Torr respectively at 25 C assuming saturated pressure conditions[24]. The actual partial pressures directly adjacent to the BCP film were not measured. The solvent leaked our of the chamber at a rate of 590 μg/ min. However, the annealing conditions can be further understood by considering the amount of solvent incorporation into the BCP film.

The initial film thickness was measured to be 42 ± 1 nm and the BCP film was swollen to 101 ± 3 upon solvent exposure as measured by in-situ spectral reflectometry (F20, Filmetrics). This corresponds to a swelling ratio of 2.4 and was reached within 10 min. After 3 hrs of solvent annealing, the chamber was rapidly evacuated with N_2 and the BCP film visibly collapsed within 1s. During the course of the solvent annealing, the BCP film underwent hole and island formation which is expected in

films containing in-plane cylinders in which the film thickness is intermediate between that required to form 1 and 2 layers of microdomains. However, the HSQ post patterns were nucleation sites for island formation which resulted in bilayer films in the region of the substrate near the post arrays. When thicker initial film thicknesses were used (e.g. 70 nm thick film, corresponding to approximately twice the periodicity of the BCP), the HSQ posts would often act as nucleation points for > 2 layer films which were not the focus of this study, hence thinner initial film thicknesses were utilized. A 5-s CF_4 RIE (50 W, 15 mTorr) was done to remove the top PDMS wetting layer and immediately followed by a 22-s O_2 RIE (6 mTorr, 90 W) to remove the PS matrix and leave the ox-PDMS patterns. SEM images were obtained using a Raith 150 scanning electron microscope operated with an acceleration voltage of 10 kV at 6-mm working distance.

Cross-section image. For cross-section imaging, a sample was made with a large area (1 micron by 600 micron) on a Si substrate, which was then was cleaved across the templated area. Cross-section images were taken at 10-kV acceleration voltage with an immersion lens and a 30-pA beam current using a Helios D521 dual beam system. The working distance was 4 mm. Dynamic focus was enabled, which allows the depth of focus to be automatically changed during imaging. The sample had no metal coating. The sample was rotated by 38 degrees for imaging.

5.2.3 SCFT Methods

Simulation. Using the same methods as presented by Mickiewicz et al.[42], 3D SCFT simulations were performed to permit improved insight into the 3D structure of the features. In addition, the simulations allowed for the exploration of the inherent metastabilities in the system between the competing morphologies. The system was modeled using 3D unit cells with periodic boundary conditions in the x- and y-directions as depicted schematically in Fig. 5.2.310. The posts were modeled by constraining the fields in the region of the posts to be a large value so that polymer density could not evolve in that region. To best match the model with experiment, a preliminary screening of the patterns obtained with various post diameters and heights

was done for the post spacings where the mesh structure occurred in experiment, as the dimensions of the field boundary conditions used to model the posts in the simulation do not match exactly to the experimental post diameters from the images. This led to the use of a simulation post diameter and height which are larger than the experimentally measured post dimensions. The brush layer was modeled using a field constraint around the boundary of the post area that was 100 preferentially attractive to the larger block (PS) and thus 100 repulsive to the smaller block (PDMS). The top air interface was modeled similar to the brush layer but 100% preferentially attractive to the PDMS, because experimental observation shows PDMS to have a lower surface energy with air than PS. System parameters to match experimental parameters were modeled using a value of $\chi N = 30.0$ and $f_{\mathrm{PDMS}} = 0.32$. This value for χN is determined by considering two factors. The first factor is the coarse graining of the simulation where an effective statistical monomer is about twice the size of the chemical PDMS and PS monomers such that $N_S = \frac{N_{\mathrm{Experiment}}}{2}$. The other factor is that the solvent is implicitly modeled in the simulation using the assumption that toluene and heptane selectively swell both blocks equally and thus the volume fraction of the BCP during the anneal is unchanged but that $\chi_{\mathrm{eff}} \sim \chi\,(1 - f_s)$, with f_s the total fraction of solvent). An alternative approach would be to explicitly model the solvent as a separate species with its own partitioning within the total partition function, but since the equilibrium structures do not appear to depend on dynamic effects of solvent evaporation, only implicitly modeling the solvent was deemed necessary by having an effective interaction parameter. Since the films swell to a final thickness of ∼3.00 L_0 from an original thickness of ∼1.20 L_0, this gives an approximate solvent fraction in the fully swollen film of 60%. For the 45.5 kg/mol polymer used χN is ∼100 near room temperature, thus a value of ChiN = 30.0 was taken for the modeling. The system initial field conditions were random and the system was evolved until a saddle point solution to the field equations was obtained that was either an equilibrium or metastable morphology. Since the solutions obtained by simulation can be metastable, multiple simulations had to be performed to first see if the system converged on a different saddle point solution, and then the energies of the resulting structures had

to be compared to determine that was the lower energy structure (these structures should correspond to the global energy minimum structures). Since these simulations typically took several days to run, additional simulations were only done for select cases where metastability was an apparent issue with the resulting structures having defects that were most likely due to a metastable saddle point solution being reached. Thus, some structures observed in the simulation may actually be metastable defects.

Metastable State Energy Comparison

In the SCFT simulations, the simulation is considered complete once the SCFT condition is satisfied which corresponds to an unchanging total energy Hamiltonian, H,with continued iterations. For the 3D model of size NX by NY by NZ = ∼20 by 20 by 42 cells, the number of iterations required to reach this condition is ∼300,000. Since the state converged upon starting with a random field configuration may not be a true global minimum, multiple simulations may be necessary to find the actual equilibrium structure without a priori knowledge of the resultant morphologies. If a general idea of the resultant morphology is known, the process of finding the actual equilibrium structure can be expedited by creating an initial field configuration of the expected morphology and seeding the simulation with those fields. For the case of the mesh structure, random initialization conditions always converged on a structure with the two layers connected. To study whether this represented a metastable defect, a set of fields without the connection was created and a simulation ran from the seeded state for the same 300,000 iterations as the randomly seeded simulations. The seeded state evolved to create a slight bulge in the top PDMS microdomain but did not connect to the bottom layer cylinder. From the energy curves, the final energy of the seeded system converged to approximately the same energy as the randomly initialized system to within 0.15%. Combined with the experimental evidence of connections in SEMs, the states are thus likely metastable and we expect the connectivity between the layers may be influenced by small changes in boundary or processing conditions.

Complex nanoscale pattern formation on two-dimensional (2D) surfaces can be achieved using template-assisted self-assembly of block copolymer (BCP) thin films. Approaches that depend on sparse patterns of lithographically defined chemical

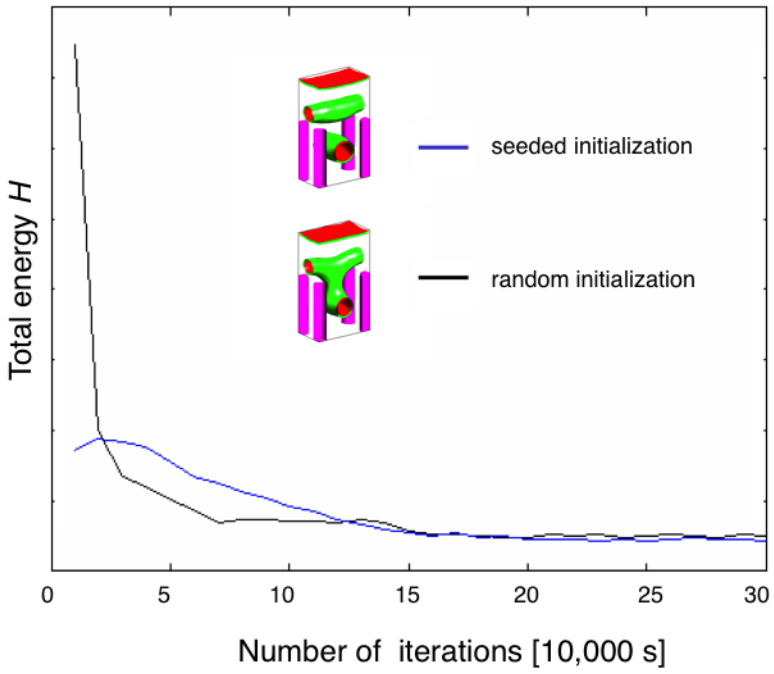

Figure 5-6: Total energy, H, versus iterations for seeded and randomly initialized mesh shaped-structures for an x-direction post periodicity of 1.71 L_0 and a y-direction post periodicity of 2.00 L_0. The inset shows 3D side view SCFT simulation of the PDMS density images with $\phi = 0.5$ green and $\phi = 0.7$ red at 300,000 iterations.

templates[8,32,96,97] or physical templates[6,9,16,99–101] have focused on controlling a single layer of BCP microdomains. This layer is then used as a mask, in combination with conventional planar processing techniques such as liftoff and etching, to fabricate devices including patterned magnetic recording media, nanowire transistors, flash memory, and gas sensors[18,46,104–107].

The inherent 3D nature of self-assembled BCPs suggests their possible use in fabricating 3D devices such as cross-point structures in a single step, rather than building up the structure sequentially. There have been reports of the fabrication of 3D structures by self-assembly of thicker BCP films or by sequential stacking and cross-linking of BCP films[21,29,108–114], but stacking methods have disadvantages for the fabrication of 3D structures because of the difficulty of aligning multiple layers, the large number of processing steps required, and the poor order of the resulting patterns. In the absence of templating, the achievable geometries of bilayer BCPs are limited; for example, in a bilayer cylindrical-morphology BCP thin film, the cylinders in each layer share the same orientation, whereas in a spherical-morphology BCP the spheres form two offset close-packed layers[115].

Chemical templating of bilayers of spherical microdomains[29,108,109] and lamellae[110] has been shown to yield square symmetry patterns and coupled perforated lamellae, respectively. A wider range of 3D BCP structures can be achieved by confinement of the BCP within parallel surfaces, narrow pores, or spherical cavities, which produce structures such as helices, cylindrical shells, and stacked disks or tori not found in bulk[21,114,116]. However, these processes do not enable the formation of interconnected structures in which the microdomains can be routed or connected arbitrarily over a large area.

In this section, experiment and self-consistent field theory show that simple periodic arrays of posts can give control over the orientation of each layer of cylinders in a bilayer BCP film, enabling the orientation of each of the two layers of cylinders to be controlled independently, simultaneously, and locally. This was accomplished by functionalizing the posts with a majority-block homopolymer brush, which rendered the posts attractive to the majority-block matrix and repulsive to the minority-block

cylindrical microdomains. The resulting self-assembled structures are understood by considering the commensurability between the post period and the equilibrium BCP period, as well as the energy costs associated with in-phase stacking of alternate layers of cylindrical microdomains. Connections between cylinders in different layers can form a cross-point-like architecture, and by locally controlling the post periodicity and arrangement, one can create specific defects, bends, and junctions in the top and bottom layers independently. Moreover, noncylindrical structures such as perforated lamellae, as well as periodic superstructures with double the period of the template, can be created. These results provide an approach for making 3D structures useful in applications (e.g., cross-point memory devices) that require the precise placement of nanowires in three dimensions. As an additional advantage, this process can produce rectangular or square-symmetric structures, which are useful in applications such as fabricating integrated circuit interconnects or bit-patterned media[117].

5.2.4 Results and Discussion

Both layers of cylinders are clearly visible in scanning electron micrographs (SEMs) after etching (Fig. 5.2.4, B and C) and are oriented with respect to the lattice vectors of the post lattice. The PDMS cylinders typically lie between the PS-coated posts (Fig. 5.2.4A, step 4) because of the PS brush, unlike the case of PDMS-coated posts where the PDMS cylinders lie atop rows of posts[36]. To describe the resulting morphologies systematically, we introduce a notation [(a b),(c d)] in which (a b) refers to the top layer and (c d) refers to the bottom layer of cylinders; (a b) and (c d) are analogous to the 2D Miller indexing of crystal lattice planes. For example, if a = 2, then for the top layer the spacing between cylinders in the x direction is half the spacing between the posts (here, the y direction is that with the smaller periodicity). In cases where the cylinders lie on top of the posts, a prime [e.g., (a b)] is included in the notation. Some post lattices generate noncylinder morphologies, which are designated S, E, or B for spheres, ellipsoids, or square-symmetry perforated lamellae, respectively, in place of the Miller indices.

Figure 5.2.4B shows a bilayer film templated by a rectangular array of PS-

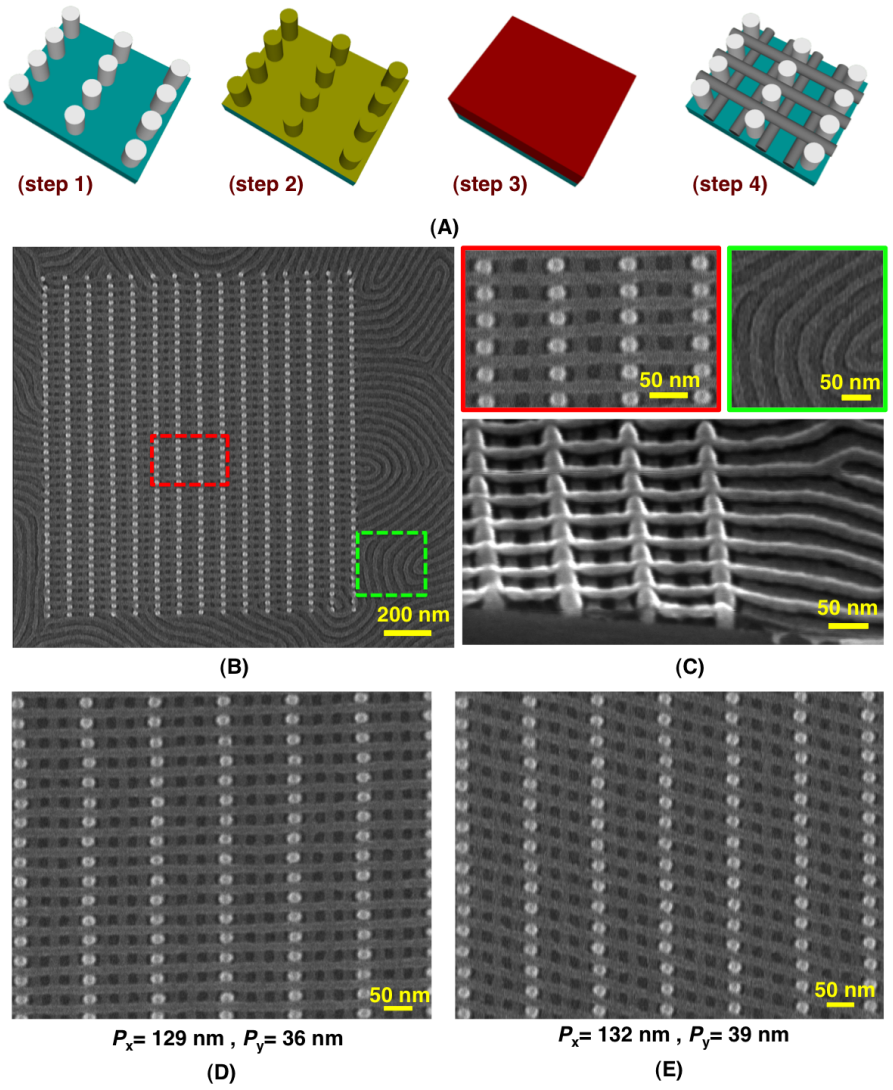

Figure 5-7: Fabrication of 3D structures. (A) The major steps of the fabrication process for the 3D structures: step 1, fabricating the post templates by electron-beam lithography; step 2, chemically functionalizing posts with a PS brush; step 3, spin coating and solvent annealing of the BCP; step 4, removing the PS matrix by an O_2 reactive-ion etch and leaving the ox-PDMS patterns on the substrate. (B) SEM of an etched [(0 1),(2 0)] bilayer structure on a substrate. (C) Upper magnified SEMs (red and green borders refer to Fig. 1B) and lower cross-sectional (lower inset) SEM of the regions inside and outside the template. (D and E) SEMs of a [(0 1),(3 0)] perpendicular structure (D) and a [(1 1),(3 0)] angled mesh-shaped structure (E) formed from two layers of ox-PDMS cylinder arrays. The bright dots and the light gray linear features represent HSQ and ox-PDMS, respectively.

functionalized posts 21 nm in diameter and 33 nm in height, with x direction periodicity of 100 nm and y direction periodicity of 36 nm. Figure 5.2.4C shows magnified and cross-sectional SEMs of regions inside and outside the templated region. Outside the templated region, the top and bottom layers of ox-PDMS cylinders shared local orientation, with the cylinders in the top layer lying in between those of the bottom layer without showing long-range order. Inside the templated region, the cylinders in the top and bottom layers did not generally share local orientation between the posts because of the energetic cost associated with incommensurability. As a result, the top cylinders instead self-assembled into a meshlike array that covered the entire templated region. Figure 5.2.4, D and E, shows another example of templated bilayer films in which additional columns of square or parallelogram-shaped holes were generated between the posts. These results demonstrate the ability to control the orientation of the individual layers of microdomains within a bilayer.

By changing the post periodicities in the x and y directions, we achieved a wide range of orientations and morphologies of both the top and bottom layers of microdomains. Figure 5.2.4 shows examples, including parallel top and bottom PDMS cylinders (Fig. 5.2.4, A and B); meshlike structures (Fig. 5.2.4, C to F); structures containing a layer of ellipsoids, spheres, or square perforated lamellae (Fig. 5.2.4, G to I); and periodic superstructures (Fig. 5.2.4, J and K). Each of these 3D structures was observed within specific ranges of post periodicities in the x and y directions, and the cylinders were oriented perpendicular to the direction in which the post periodicity was commensurate with the BCP period. In general, the top layer of cylinders formed the more commensurate arrangement. These structures are consistent with the equilibrium morphologies observed in the self-consistent field theory (SCFT) simulations, which modeled the morphologies present when the film was fully swollen (before quenching).

Figure 5.2.4, A and B, shows cases where the cylinders in both layers were oriented parallel (in the y direction, Fig. 5.2.4A; in the diagonal direction, Fig. 5.2.4B) and the cylinders in the top layer were offset from those of the bottom layer, as seen in the untemplated bilayer film. The offset stabilizes the parallel arrangement, but it incurs an energy penalty if there is contact between the cylinders and posts. The top

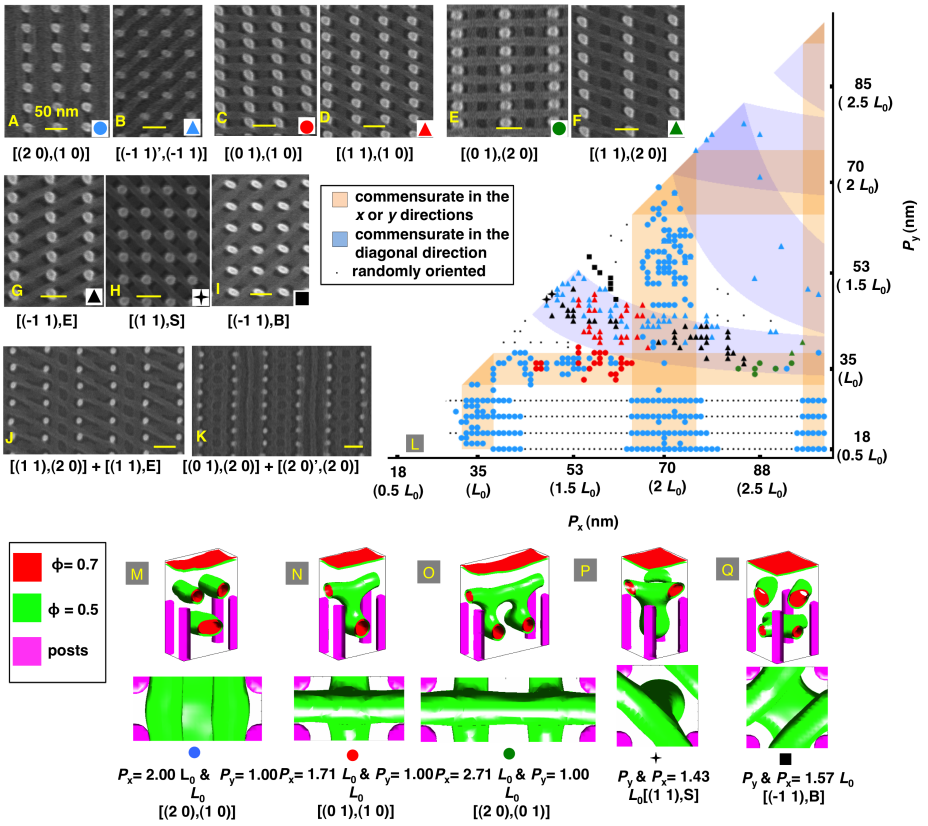

Figure 5-8: Templating and modeling 3D self-assembled structures. (A to K) SEMs of the ox-PDMS microdomains templated by post arrays. White and light gray areas represent HSQ posts and ox-PDMS, respectively. Ox-PDMS microdomains were commensurate in the same direction [(A) and (B)] or formed perpendicular and angled mesh-shaped structures [(C) to (F)], cylinders on top of ellipsoids (G), cylinders on top of spheres (H), cylinders on top of perforated lamellae (I), and periodic superstructures [(J) and (K)]. Circles denote cylinders oriented along x or y; triangles, stars, and squares denote cylinders oriented in a diagonal direction. (M to Q) SCFT simulation results for representative post periods. Top images, isometric views; bottom images, top-down views. Surface contours of constant minority-block (PDMS) density ϕ are plotted; $\phi = 0.5$ represents the boundary between the PS and PDMS blocks.

layer of cylinders could overlay the posts (Fig. 5.2.4B), but in cases where the bottom layer lay along a line of posts, it was interrupted to form dash shapes.

In Fig. 5.2.4, C to F, the cylinders in the two layers became oriented in two different directions and made a mesh-shaped structure. Mesh-shaped structures occurred when the post period in the y or diagonal direction was equal to the BCP period, favoring alignment of one layer of cylinders perpendicular to the y or diagonal direction, but the period in the x direction was slightly less than an integer multiple of the BCP period. In this case, the parallel alignment seen in Fig. 5.2.4, A and B, is less favorable than a mesh structure. Depending on the commensurability of the post lattice, the angle of the mesh was 90° (Fig. 5.2.4, C and E) or more (Fig. 5.2.4, D and F).

The mesh structures of Fig. 5.2.4, C to F, can be generalized to include larger numbers of cylinders subdividing the x-axis period, as shown in Fig. 5.2.4, D and E, where the post periods in the x direction were less than 4 times the BCP period. The dimensions of the square and parallelogram holes in all the mesh-shaped patterns were 18 by 18 nm, and their periods in the y direction were ∼36 nm, matching the BCP period. The resulting parallelogram and square holes demonstrated sharp corners relative to those fabricated using conventional lithography, which suggests a role for such structures in the generation of nanoscale square or rhombic features or pits.

Figure 5.2.4, G to I, shows examples in which the bottom layer of microdomains formed ellipsoids (Fig. 5.2.4G) or spheres (Fig. 5.2.4H) between the posts, and square perforated lamellae in which the holes in the PDMS surrounded the posts (Fig. 5.2.4I). These structures occurred when the BCP period was not commensurate with either the x or y direction spacing. We also observed periodic superstructures in which the structure alternated between two morphologies between adjacent columns of posts, resulting in twice the period of the post lattice. Examples are shown in Fig. 5.2.4, J and K.

To analyze the experimental morphologies, a phase diagram (Fig. 5.2.4L) was made in which the various morphologies are plotted as a function of post period Px and Py in the x and y directions, respectively. The periods are expressed as multiples of L_0, the equilibrium period of cylinders in an untemplated film annealed under the

same conditions. Superposed on this graph are vertical and horizontal colored bands representing approximate commensurate conditions (i.e., when Px and Py are within ±9% of an integer multiple of L_0). Curved colored bands represent commensurate conditions for the diagonal spacing. A value of 9% was chosen because BCP films have been found to adjust their period in response to a template by up to approximately this amount[7,36]. Examination of Fig. 5.2.4L shows that the observed morphologies correspond well with the commensurate template conditions. The correspondence indicates that commensurability in both x and y directions plays a dominant role in determining which morphology forms.

SCFT simulations were carried out to investigate the 3D structure of the features, as well as the metastability of the structures observed. The thickness of the unit cell was set to the swelled BCP thickness observed during the solvent annealing, which was ∼3.00 L_0; the post diameter and height were 0.71 L_0 and 1.64 L_0, respectively. The simulation results showed the same general trends as the experiments. Parallel cylinders were predicted by the SCFT simulation for x direction post periods equal to integer multiples of L_0 (Fig. 5.2.4M). Perpendicular mesh-shaped structures were predicted for x direction periods less than an integer multiple of L_0 (2 L_0, 3 L_0) and y direction periods equal to L_0, as was seen in the experiments (Fig. 5.2.4, N and O). Different morphologies in the two layers were predicted by SCFT, such as cylinders over spheres (Fig. 5.2.4P) and cylinders over perforated lamellae (Fig. 5.2.4Q). However, simulations of two unit cells did not predict the observed superstructures. Consideration of factors not included in the SCFT, such as bending of the posts or non-equilibrium formation during the solvent vapor annealing, may be required to explain these structures. Crossed cylinders have been predicted in a BCP confined between parallel surfaces with highly incommensurate spacing[116].

In the simulations, the cylinders in the two layers were often connected (Fig. 5.2.4, N to P). These connections between the two layers may be metastable defects. However, there is also experimental evidence in the mesh-shaped structures for these connections. By seeding the simulation with a field configuration that represented a mesh-shaped structure without a connection, it was determined that the energies of

the connected versus unconnected systems were too close to distinguish a lower-energy state. Thus, local connections between cylinders are likely to be present in the system and should be considered in postprocessing applications for these patterns.

In addition to controlling the alignment and morphology of the PDMS microdomains in two different layers, we were also able to locally control the alignment of the microdomains to form more complicated patterns with specific defects, bends, and neighboring junctions. In particular, junctions and bends were placed in either of the layers of cylindrical microdomains. Two approaches were used, separately or in combination, to fabricate such aperiodic structures: (i) a post array with a variation in the post periodicity in one or both directions to fabricate bends and junctions (T and angled junctions) in the top layer; and (ii) a post lattice whose orientation varied while the period was constant to fabricate bends and junctions (T, angled, and Y junctions) in the bottom layer. These types of bends and junctions could potentially be used to fabricate integrated-circuit elements[24]. Figure 5.2.4A shows a structure made by the first approach in which, by increasing the post periodicity in the x direction, a [(0 1),(2 0)] structure joined with a [(3 0),(2 0)] structure and, by increasing the post periodicity in the y direction and decreasing it in the x direction, the [(3 0),(2 0)] structure joined with a [(1 1),(2 0)] structure. Thus, the bottom layer of cylinders had a fixed direction (y direction) and only the direction of the top cylinders was varied; structures such as T junctions formed where the different orientations met. Figure 5.2.4B shows a structure made using the second approach in which, by changing the post arrangement, the [(-1 1),(2 0)] structure contained a mirror plane parallel to the [1 1] direction of the lower post lattice. The top layer of cylinders had a fixed direction (x direction), and only the direction of the bottom cylinders was varied.

SCFT simulations were carried out to investigate both the 3D structure of the features as well as the metastability of the structures observed[114]. The thickness of the unit cell was set to the swelled BCP thickness observed during the solvent annealing, which was $\sim$3.00 L_0, and the post diameter and height were 0.71 L_0 and 1.64 L_0, respectively.The simulation showed the same general trends as the experiments. Parallel cylinders were predicted by the SCFT simulation for x-direction post periods

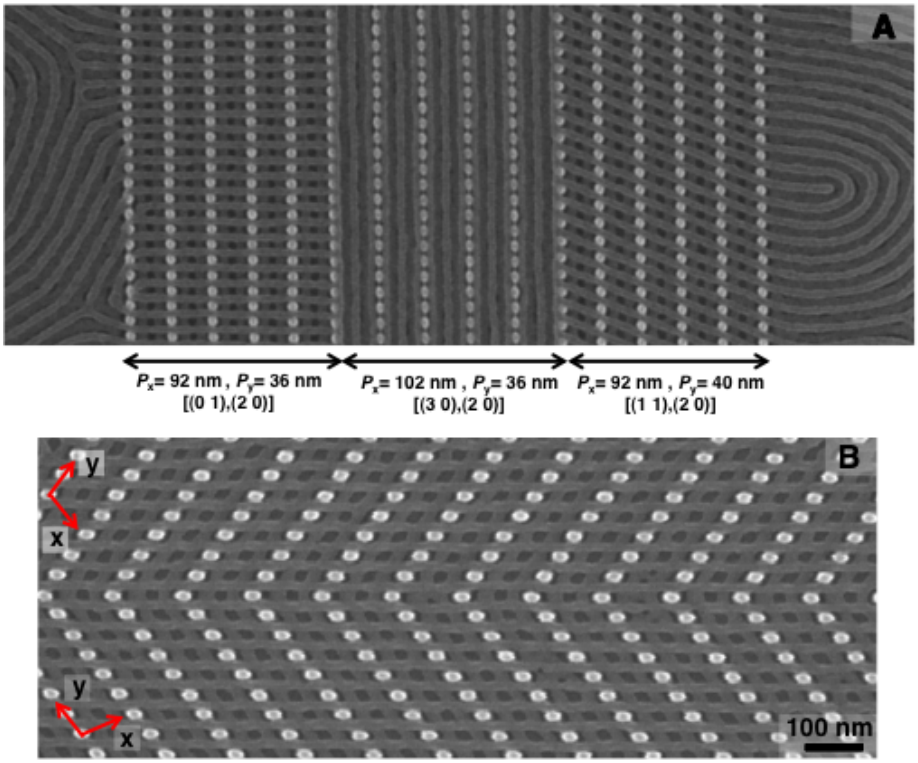

Figure 5-9: Templated 3D bends and junctions. (A) SEM of a locally controlled structure fabricated by changing the post periodicity in the x and y directions. From left to right, the structures changed from [(0 1),(2 0)] to [(3 0),(2 0)] and then to [(1 1),(2 0)]. (B) SEM of a locally controlled structure fabricated by changing the post lattice orientation. Top to bottom, the [(-1 1),(2 0)] structure contained a mirror plane parallel to the [1 1] direction of the lower post lattice. The x and y axes make an angle of 107°. White and light gray areas represent HSQ and ox-PDMS, respectively.

equal to integer multiples of L_0 (Fig. 5.2.4M). Perpendicular mesh-shaped structures were predicted for x-direction periods less than an integer multiple of L_0 (2 L_0, 3 L_0) and y-direction periods equal to L_0, as was seen in the experiments (Fig. 5.2.4N,O). Different morphologies in the two layers were predicted by SCFT such as cylinders over spheres (Fig. 5.2.4P) and cylinders over bicontinuous cylinders (Fig. 5.2.4Q). However, simulations of two unit cells did not predict the observed superstructures. To explain these structures, factors not included in the SCFT such as bending of the posts or non-equilibrium formation during the solvent vapor annealing may be important. In the simulations, the bottom cylinders did not orient along the commensurate direction due to the confinement of the posts while the top cylinders were able to orient along the commensurate direction due to the increased swelling thickness of 3.00 L_0. Recently, crossed cylinders were also predicted in a BCP confined between parallel surfaces with highly incommensurate spacing[113]. In the simulations, the cylinders in the two layers were often connected, as shown in Fig. 5.2.4N-P. These connections between the two layers may be metastable defects. However, there is also experimental evidence in the mesh shaped-structures for these connections. By seeding the simulation with a field configuration that represented a mesh shaped-structure without a connection, we found that the energies of the connected vs. unconnected systems were too close to distinguish a lower energy state[114]. Thus, local connections between cylinders are likely to be present in the system and should be considered in post-processing applications for these patterns.

It was also possible to locally control the post periodicity and arrangement to form more complicated patterns with specific defects, bends and neighboring junctions. In particular, junctions and bends were placed in either of the layers of cylindrical microdomains. Two strategies or a combination of them were used to fabricate such aperiodic structures: (1) a rectangular post array with a variation in the post periodicity in one or both directions to fabricate bends and junctions (T- and angled-junctions) in the top layer; and (2) a post lattice whose orientation varied while constant period to fabricate bends and junctions (T-, angled- and Y-junctions) in the bottom layer. These types of bends and junctions could potentially be used to

fabricate integrated-circuit elements. Fig. 5.2.4A shows a structure made by the first strategy in which, by increasing the post periodicity in the x-direction, a [(0 1),(2 0)] structure joined with a [(3 0),(2 0)] structure and, by increasing the post periodicity in the y-direction and decreasing it in the x-direction, the [(3 0),(2 0)] structure joined with a [(1 1),(2 0)] structure. Thus the bottom layer of cylinders had a fixed direction (y-direction) and only the direction of the top cylinders was varied; structures such as T-junctions formed where the different orientations meet. Fig. 5.2.4B shows a structure made using the second strategy in which, by changing the post arrangement, the [(-1 1),(2 0)] structure contained a mirror-plane. The top layer of cylinders had a fixed direction (x-direction) and only the direction of the bottom cylinders was varied.

5.2.5 Summary

The central result of this work is the independent and simultaneous control of the morphology and orientation of two layers of BCP microdomains guided by an array of functionalized posts. This forms the basis for the creation of more complicated structures such as cylinders with specific defects, bends, and junctions, as well as noncylindrical morphologies, and connections between the top and bottom layers of cylinders can be made. These results were only found to be possible with SVA and were not found to be possible with thermal annealing. The strategies demonstrated here for the 3D routing of dense nanoscale cylindrical features using a single self-assembly step could facilitate new methods for nanoscale device manufacturing when combined, for example, with processes that convert microdomains selectively into functional materials such as oxides or metals[118]. The next section is a continuation of the previous two sections where HSQ posts were replaced with PMMA posts and were found to also be viable candidates for nano scale bondary conditions.

5.3 Removable Templates

5.3.1 Introduction

A sacrificial-post templating method is presented in this section for directing block copolymer self-assembly to form nanostructures consisting of monolayers and bilayers of microdomains. In this approach, the topographical post template was removed after self-assembly and therefore was not incorporated into the final microdomain pattern. Arrays of nanoscale holes of different shapes and symmetries, including mesh structures and perforated lamellae with a bimodal pore size distribution were produced and only viable with solvent vapor annealing.

In general, for topographical templating the template becomes incorporated into the BCP microdomain array. Sacrificial methods have therefore been developed to direct BCP self-assembly in trenches made from an etchable material, allowing the subsequent removal of the template to result in a template-free final arrangement of microdomains[119,120]. This section presents a sacrificial-post templating method for block copolymer self-assembly which combines the capabilities of post templating with the sacrificial templating methods developed for trench topographies. The method described here produces geometries previously not realized by physical or chemical templating such as 3-D grid patterns and arrays of holes with bimodal size distributions. Furthermore, sacrificial-post templating is expected to be integrable with semiconductor manufacturing processes because the templates could potentially be made using optical lithography and trim etching (instead of the electron-beam lithography presented in this work). The use of a removable template could mitigate potential pattern transfer difficulties caused by the dissimilar etch rates for physical templates compared to the BCP nanopatterns. Prior work has demonstrated the use of removable templates with feature sizes that are coarse compared with the period of the BCP. Ilievski et al.[119] used trenches made from an anti-reflective coating (ARC) for graphoepitaxy of spherical-morphology poly(styrene-block-ferrocenyldimethylsilane). The ARC was subsequently removed by O_2 plasma etching along with the polystyrene block to leave only the templated polyferrocenyldimethylsilane microdomains. Moon

et al.[120] made removable templates using deep-UV lithography to template lamellar poly(styrene-block-methyl methacrylate), then followed the template removal by infilling the spaces formerly occupied by the template with a second BCP thin film templated by the first BCP pattern. Several reports[121–123] showed the fabrication of BCP nanopatterns from reusable nanoimprint trench templates. These imprint processes generated highly oriented patterns, and the patternless regions could subsequently be filled by additional steps[120,124]. Post templating makes use of arrays of posts with lateral dimensions on the order of the half the period of the block copolymer to create a range of complex microdomain patterns including several morphologies on a single substrate[125] and bilayer meshes[126] , but to date, the posts have been made from an inorganic resist material, hydrogen silsesquioxane (HSQ), which is etch resistant. By making the posts from an organic resist, polymethylmethacrylate (PMMA), the posts can be removed along with the polystyrene block of a polystyrene-polydimethylsiloxane (PS-b-PDMS) BCP in an O_2 etch, leaving only the PDMS microdomains behind. This section demonstrates the templating of PDMS nanostructures including in-plane cylinders, spheres, ellipsoids, and superstructures; perforated lamellae and rectangular meshes with holes of different diameters, symmetries (square and hexagonal), shapes (square, circular, rectangular and hexagonal) and bimodal hole sizes; and with two- and three-fold pattern multiplication, expanding on previous results[125]. The experimental results for the bimodal size distribution and pattern multiplication gave excellent agreement with self-consistent field theory (SCFT) models used. For applications such as stepper mask generation and high-density magnetic memory which rely on electron-beam lithography for pattern generation, this technology is a direct complement for increasing throughput, process latitude, and pattern variety. Furthermore, BCP directed self-assembly is potentially applicable in areas such as integrated circuits, nanowire transistors, cell analysis, gas sensing, magnetic nanopatterns.

5.3.2 Experimental Methods

Figure 5.3.2 shows the major steps of the sacrificial-post templating method for the fabrication of monolayers (Figure 5.3.2, top) and bilayers (Figure 5.3.2, bottom) of

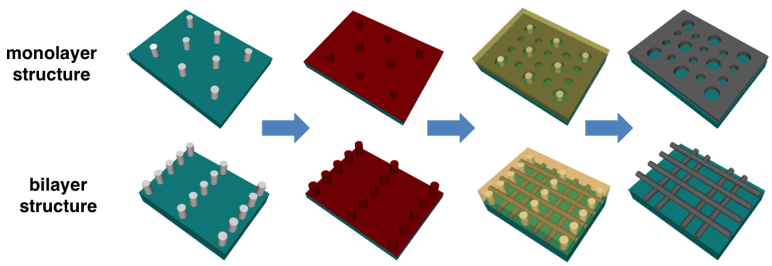

Figure 5-10: Schematic diagram of the major steps in fabrication of monolayer (top) and bilayer (bottom) microdomain arrays using the sacrificial-post templating method. (Step 1) electron beam lithography fabrication of arrays of posts of negative-tone PMMA resist, (Step 2) functionalization of posts and substrates with a PS brush, (Step 3) spin coating and solvent annealing of the PS-b-PDMS BCP thin film, and (Step 4) RIE removal of the top PDMS layer with CF_4 then the PS matrix and PMMA posts with O_2. The ox-PDMS nanostructure remained on the substrates as the final nanopatterns.

microdomains from a PS-b-PDMS BCP in which the bulk morphology consisted of cylinders of PDMS in a PS matrix. In the first step, the templates were fabricated using electron-beam-lithography (EBL) exposure of PMMA resist on a silicon substrate. Next, the templates were chemically functionalized with a hydroxyl-terminated PS brush and the PS-b-PDMS was spin-coated onto the substrates and annealed at room temperature in a cosolvent vapor resulting from a 5:1 ratio mixture of toluene and heptane (by volume). An O_2 reactive ion etch was used to remove the PS block and leave the oxidized-PDMS patterns on the substrates. A variety of mono- and bilayer structures was achieved using template patterns with different lattices, periods, and diameters of the posts.

The templates were fabricated using EBL of 40 nm thick films of PMMA as a negative-tone resist (Figure 5.3.2, Step 1). PMMA is typically a positive-tone resist but previous studies have shown that this resist acts as a negative-tone due a carbonization process when exposed to doses about 30 times the positive-tone dose and developed with methyl isobutyl ketone (MIBK)[127]. When PMMA is exposed to high dose, there are three regions with respect to the beam spot: a highly exposed region near the beam spot from the primary beam and secondary electrons; a lightly exposed region in proximity to the beam spot from the back-scattered electrons; and an unexposed region

far from the beam spot. Development with MIBK only removed the PMMA from the lightly exposed region[127], and failed to remove the PMMA from the unexposed region, so the process was modified by sonicating the samples in acetone for 2 min after development. Acetone sonication removed the unexposed PMMA and left the posts on the substrates. After the exposure and development, the diameter and the height of the posts were about 17-30 nm and 30 nm, respectively. Next, the samples were functionalized with hydroxyl-terminated PS brush, PS-OH (1 kg/mol, purchased from PolymerSource) by spin-coating the PS-OH then annealing for 14 hrs under vacuum at 170°C (Figure 5.3.2, Step 2), which made the posts repulsive to the minority block (PDMS) and attractive to the majority block (PS). PS-b-PDMS (MW=45.5 kg/mol, f_{PDMS}=0.32, equilibrium period approximately 35 nm, purchased from PolymerSource) was spin-coated onto substrates to average 30 nm thickness in order to achieve a single-layer of in-plane PDMS cylindrical microdomains on untemplated substrates, and 42 nm thick to obtain bilayers of cylinders. Solvent annealing was carried out using the vapor from a volumetric mixture of toluene and heptane (5:1) for 1.5 hrs at room temperature (Figure 5.3.2, Step 3)[128]. A CF_4 RIE was used to remove the PDMS surface wetting layer, immediately followed by an O_2 RIE to simultaneously remove the PS matrix and the PMMA posts and to oxidize the PDMS, leaving the final ox-PDMS nanopatterns on the surface (Figure 5.3.2, Step 4).

5.3.3 Results and Discussion

Figures 5.3.3 show the experimental results of the fabrication of monolayer structures using the sacrificial-post templating method. The middle of the image shows regions where the sacrificial-posts were present whereas the left and right sides of the images, which were covered with randomly oriented in-plane cylinders, are representative of unpatterned areas. Insets in these figures show the locations of PMMA posts before removal by the O_2 RIE. The microdomains of the BCP transitioned between multiple morphologies as a function of the post pitch. For example, increasing the pitch for a square or rectangular symmetry post array resulted in in-plane cylinders transitioning to spheres (Figure 5.3.3a), ellipsoids, periodic superstructures, perforated

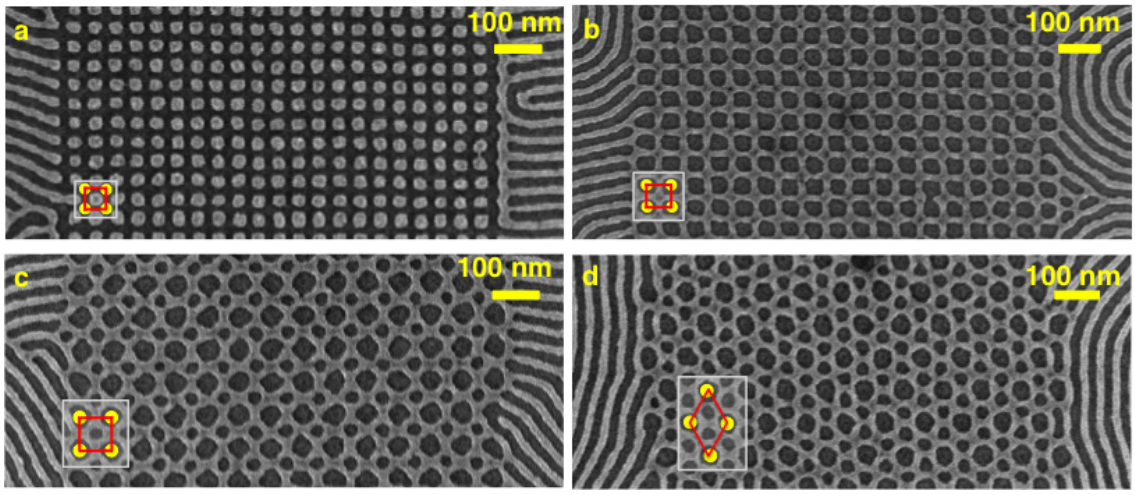

Figure 5-11: SEMs of monolayer nanostructures fabricated by the sacrificial-post templating method. Shown are a (a) square array of spheres, (b) a square symmetry L1 perforated lamella, (c) square symmetry L2 perforated lamella with one hole generated between each group of four posts and (d) hexagonal symmetry L2 perforated lamella of nanoholes with one hole generated between each group of three posts. Light grey and dark grey colors represent ox-PDMS and the substrate, respectively. Insets show the pre-removal locations of negative-tone PMMA posts in yellow. Red outlines represent unit cells for the final nanostructures.

lamellae labelled L1 where each post corresponds to one hole (Figures 5.3.3b) and perforated lamellae with additional generated pores that appeared in between the posts, labelled L2 (Figure 5.3.3c,d). In the sphere array, Fig. 5.3.3a, the PDMS spheres had similar diameter to the PMMA posts. The holes in the perforated lamellae were not necessarily circular, e.g. Figs. 5.3.3b and 5.3.3c show holes with a rounded square shape. Hexagonal post arrays also led to L1 and L2 perforated lamellae with hexagonal symmetry (Fig. 5.3.3d). These transitions are driven by changes in commensurability between the post spacing and BCP period, and are the same as those obtained from HSQ posts[125]. This shows that the PS-brush effectively grafted onto the PMMA posts and provided the same boundary conditions as those obtained from PS-functionalized HSQ posts.

3D SCFT simulations[125] were performed to gain insight into the effect of post pitch on the morphology, shape and size of the experimental nanostructures. Figure 5.3.3 shows simulation results analogous to the nanopatterns achieved in Figure 5.3.3

which were produced by changing the ratio between the post spacing and L_0, the BCP equilibrium period. These simulation results are based on a unit cell containing one or two posts and periodic boundary conditions, in which the posts and substrate surfaces are attractive to the majority block and the top (air) surface to the minority block. In the case of the structures in Figure 5.3.3a, b, and c, the square symmetry of the PDMS microdomains is driven by the square symmetry of the post array with period $<2\ L_0$, which provides a strong templating effect similar to previous work with square symmetry chemical patterns[109,125] that promoted square symmetry arrays of cylindrical microdomains. The SCFT reproduced the trend in morphology from spheres to L1 and then L2 as seen experimentally with increasing template pitch, and also showed that the curvature and the shape of the hole produced around the posts was non-circular.

Perforated lamellar morphologies (L2). The perforated lamellar structures L2 are of particular interest because of the density multiplication of the holes compared to the posts, and because bimodal hole sizes can be produced. This structure was observed in prior work using HSQ posts[125], but the trends in hole size were not analyzed. The L2 structures produced from HSQ posts are similar to Figure 5.3.3c,d produced from PMMA posts. In each case, two types of holes were identified: post-holes, which surround the posts, and generated-holes which formed between the posts. In Figure 5.3.3.c,d, each post generated an additional one and two holes, respectively. Figure 5.3.3 shows how the sizes of the post-holes and generated-holes varied with the post pitch and diameter for the hexagonal symmetry L2 perforated lamella of Fig. 5.3.3d. Here the post pitch is the center-to-center distance between posts. A Matlab computer program was used to extract the experimental data points presented in Figure 5.3.3 from SEM images. The simulated data points were determined from only those simulations which formed the L2 structure. The coarse-graining limited the values of post spacing and diameter that could be modeled. The post diameter in the simulation was changed by increments of $\sim$3 nm. However, the simulations examined a wider range of post pitches and post diameters than the experiment, up to 110 nm ($\sim$3.2 L_0) and 43 nm ($\sim$1.2 L_0), respectively, where L_0 is the cylinder spacing in the

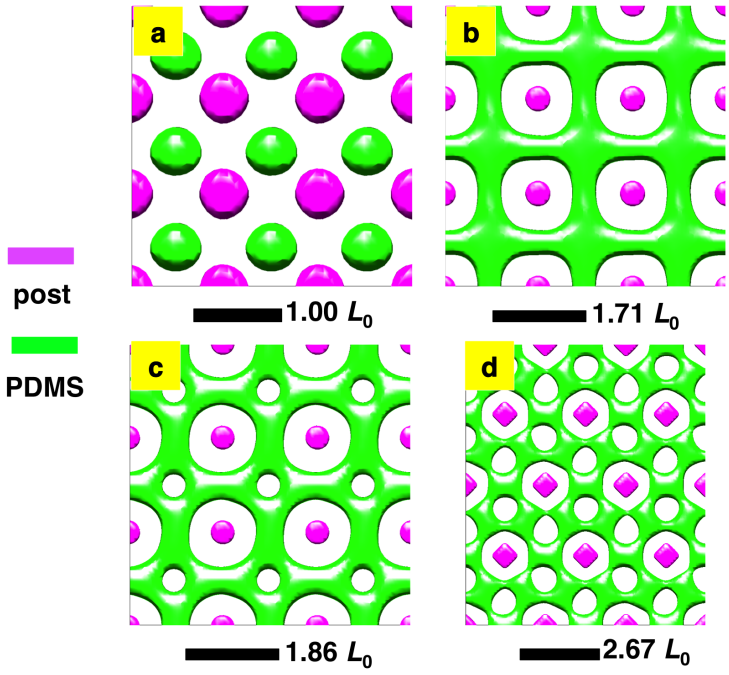

Figure 5-12: Top-down 3D view of self-consistent field theory simulation results of PS-b-PDMS single-layer thin film equilibrium structures with PS-coated posts of different pitch. (a) A square array of spheres at pitch L_0, (b) a square symmetry perforated lamella L1 for post pitch of 1.71 L_0, (c) a square symmetry perforated lamella L2 for pitch 1.86 L_0, and (d) a hexagonal symmetry perforated lamella L2 for pitch 2.67 L_0. Each image is made as a composite of 9 (a-c) or 6 (d) identical images to show the geometry more clearly. L_0 is the cylinder pitch in the untemplated BCP.

untemplated BCP, ∼35 nm. Out of 12 simulations, 4 had defects in which two of the generated-holes connected. These data points are shown with a hollow triangle or diamond in the plot, and such defects were observed experimentally as well. The L2 structure formed in templates with an interpost spacing (i.e. the difference between post pitch and post diameter) of approximately 2 L_0 over a range of post pitches and diameters. The general experimental observation was that the generated-holes had an approximately constant diameter, whereas the post-hole diameter increased with post pitch and post diameter, giving a bimodal hole size distribution. The post-holes were formed by the PS chains which surrounded each post, and their diameter therefore increased (linearly) as the posts became larger. In contrast, the generated-holes had an almost invariant diameter similar to that formed in an untemplated perforated lamella, and there would be a large entropic penalty for the chain extension needed to increase their size. The SCFT results agreed very well with the experimental results, and suggested that the trends in hole size extended to larger template pitch and diameter than the experimentally investigated range.

The minimum post pitch where the L2 perforated lamella was observed was ∼80 nm. If a cylindrical BCP of period L_0 were to transition into a perforated lamella, the row spacing of the holes would be L_0 and the center-to-center distance between holes would be $\frac{\sqrt{3}}{2}L_0$, meaning a post pitch of at least 2 L_0 (70 nm) is necessary to allow two rows of holes to fit between each pair of posts and thus stabilize the normally metastable perforated lamellae structure. This commensurate condition stabilized the hexagonal L2 structure, which persisted to post pitches of at least 3.2 L_0 (in the model) = 110 nm by accommodating the strain through increases in the post-hole diameter. The post template helps to stabilize the normally metastable perforated lamella due to the confinement effects[39,129–131]. Bilayer microdomain arrays. Figure 5.3.3 shows the results of the bilayer mesh-shaped nanostructures after post removal (Figure 5.3.2, step 4). The mesh-shaped structures formed from a film that was thick enough to produce a bilayer of in-plane cylinders over the region of the substrate containing posts. The mesh formed when the post pitch in the diagonal or y-direction was equal to L_0, favoring alignment of one layer of cylinders perpendicular to the

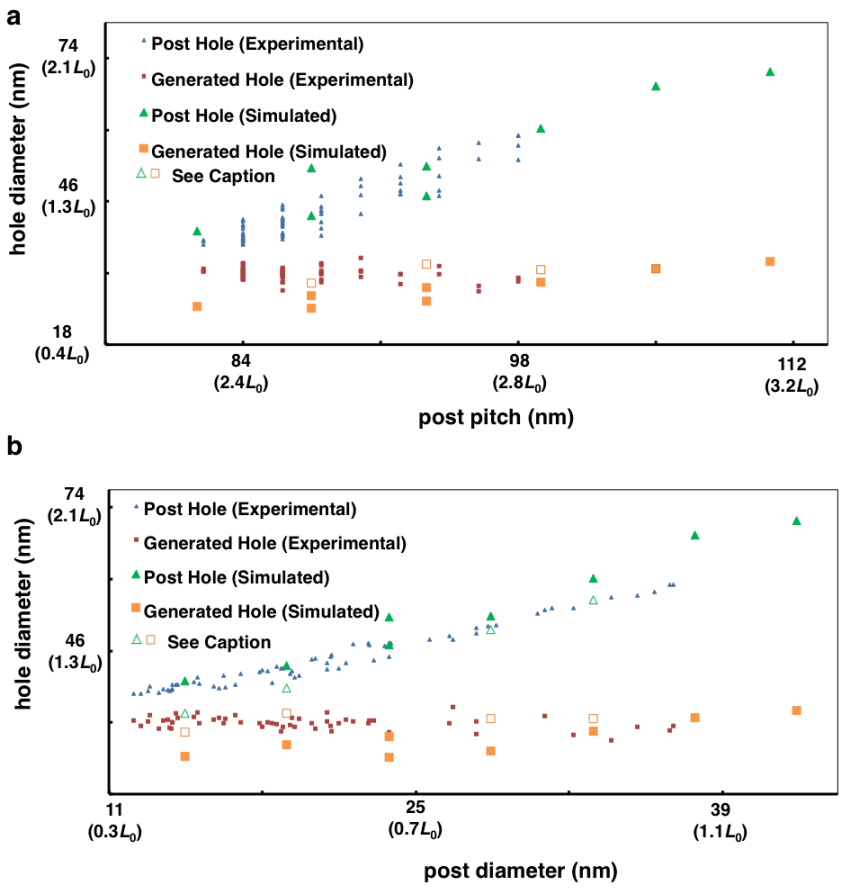

Figure 5-13: Experimental and simulation graphs of the post-hole and generated-hole diameter versus the (a) post pitch and (b) post diameter. In (a), multiple data points for a given post pitch represent templates with different post diameters. In (b), multiple data points for a given post diameter represent templates with different post pitch. In both simulation and experimental results, the generated-hole diameter does not vary much with post pitch and diameter, whereas the post-hole diameter increases linearly with post pitch and diameter. For experimental data, HSQ posts were used instead of PMMA posts. Open triangles and squares represent structures with defects.

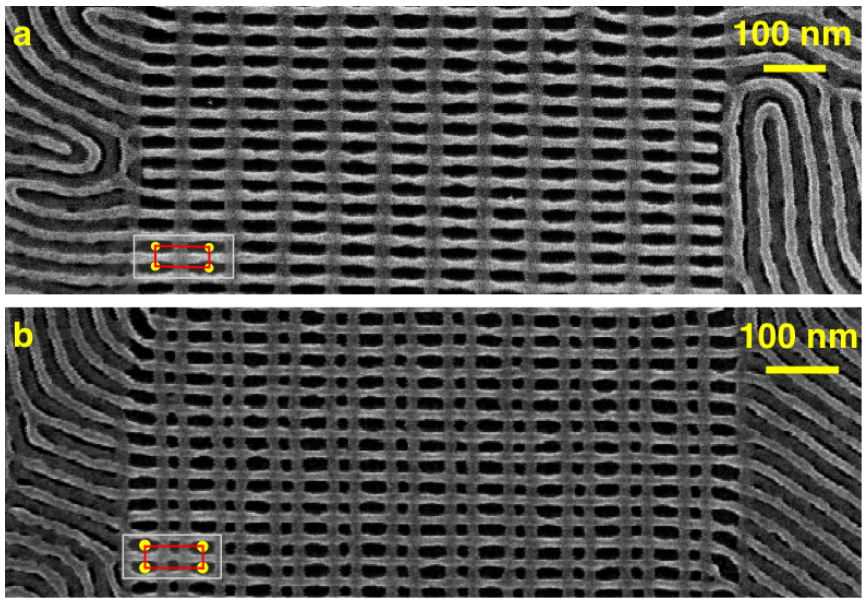

Figure 5-14: SEMs of mesh structures fabricated by the sacrificial-post templating method. (a) Mesh of rectangular holes from a template with period 35 and 96 nm along the y and x-directions, respectively; (b) mesh of bimodal rectangular holes from a template with period 36 and 136 nm along the y and x-directions, respectively. Light grey is the ox-PDMS and dark grey colors the substrate. Insets show the locations of negative-tone PMMA posts in yellow. Red outlines represent unit cells for the nanostructures.

diagonal or y-direction, and the post period in the x-direction was slightly less than an integer multiple of L_0 [126]. The PMMA posts produced the same structures as the HSQ posts of Tavakkoli et al. [126], but post removal left rectangular holes. This is in contrast to the untemplated regions of the substrate in which the upper and lower layers of cylinders were parallel without long range order. Insets in these figures show the locations of posts before removal. Figure 5.3.3.b shows bimodal rectangular holes after etching bilayer structures, templated by posts with a larger x-spacing.

5.3.4 Summary

In summary, this work demonstrates a sacrificial post-templating method which avoided the incorporation of the physical templates into final BCP nanopatterns. These carbon based posts may be more susceptible to damage induced by higher temperatures which would be required for a thermal anneal of this high-χ system

thus necessitating the use of solvent vapor annealing. The removable PMMA post array templated structures similar to those formed from an HSQ post array with the same geometry, because the majority brush layer on the posts led to the same boundary conditions on the self-assembly of the BCP irrespective of the post material. This method was successfully used for the fabrication of both monolayers of in-plane microdomains, including spheres, cylinders and perforated lamellae, and bilayers of cylinders forming a mesh structure, and pattern density multiplication was achieved. Perforated lamellae with bimodal hole sizes were analysed in detail, showing that one set of holes had a diameter that was almost independent of template geometry while the other set of holes had a diameter that increased with post diameter. These results are expected to simplify pattern transfer in block copolymer lithography, and provide a route to making hole arrays with bimodal size distribution and square, rectangular or hexagonal symmetries and exemplify the importance of SVA for directing the self-assembly of PS-b-PDMS.

Chapter 6

Solvothermal Annealing

6.1 Introduction

As has been discussed in the previous chapters, solvent vapor annealing requires the control of many parameters to be done effectively. Chapter 3 discussed the basic solvent annealing setup and showed how important the solvent removal rate was to the final self-assembled system. Chapter 4 discussed how properly controlling vapor pressures allows for more reproducible and systematic studies of the self-assembly. Chapter 5 discussed the possibilities of patterns that can result from combining the knowledge of self-assembly with templates to guide them and also reinforced the flexibility shown in this PS-b-PDMS system which requires SVA for reasonable time scales of self-assembly to be met. I consider this chapter to be the capstone of my thesis work, where all of this knowledge was combined to enable fast and controlled self-assembly by properly heating the BCP system during a time after introduction to solvent vapors. By combining the knowledge of the importance of swelling ratios, annealing time, solvent removal rate, and the effects of temperature, dramatic improvements to self-assembly could be achieved.

After a BCP film is applied to a surface the polymers will have varying degrees of kinetically trapped states that need to be removed before self-assembled patterns can form. Thermal annealing is often used where the BCP films are heated above the T_g but below the order-disorder transition temperature (ODT) to promote microphase

separation. This can pose a problem for high-χ BCPs as they can have ODTs far above the temperatures at which degradation or chain scission can occur[68]. Solvent vapor annealing[50] can help high-χ BCPs overcome this problem by allowing solvent molecules to interact and swell a BCP film thereby reducing the diffusive energy barrier[11] and shortening annealing times. It is important to note that the solvent removal rate can effect orientation and annealing quality within a BCP film allowing an additional lever of variability not available to thermal annealing[70,132–134] as was mentioned in Chapter 3.

SVA and thermal annealing studies have typically allowed the BCP films to self-assemble for many hours, and these timescales have been sufficient for producing highly-ordered periodic structure over large area with low defectivity[135]. However, in order for BCP self-assembly to be a viable alternative for next-generation lithography, these annealing times have to be dramatically reduced to the seconds or minutes timescales to keep pace with the stringent wafer/hour metrics required by industry. To approach this problem, researchers have recently begun to try to combine the best characteristics of SVA (morphology control, control over effective T_g, etc.) with thermal annealing (higher diffusivities rates, ease of temperature control, etc.) so that shorter annealing times can be achieved. Zhang et al. showed that microwave heating combined with a solvent rich environment enabled templated self-assembly of BCPs within minutes[136]. Park et al. found that by applying heat to a metal SVA chamber, templated self-assembly could be achieved within minutes with very high resolution (sub-10 nm half pitch) using the PS-b-PDMS system[137]. These studies proved that by combining both solvent and thermal methods, annealing times can be dramatically reduced.

The direct effects that the temperature and the solvent annealing have on the self-assembly when the methods are combined is unclear. Heating a SVA chamber increases the overall system temperature and allows solvents to reach higher vapor pressures which may allow the BCPs to reach higher swelling ratios (final/initial thickness, D/D_0) and thus increase the BCP mobility. In this work we add clarification to understanding the different effects that the application of solvent vapor and heat have

on BCP thin-films by decoupling the temperature of the BCP from the temperature of the surrounding solvent vapor environment and by tracking *in situ* swelling ratios of templated thin films of PS-b-PDMS and monitoring the quality of the self-assembled films. The following section provides experimental details to achieving the results of this work.

6.2 Experimental Methods

Template fabrication. The periodic post templates were made with an Elionix F-125 SEBL system using HSQ (Dow Corning XR-1541 2% solids), a negative-tone electron resist. HSQ was spun with 402 nm thickness on top of prime Si wafers. HSQ was exposed with a 1 nA beam with 125-kV acceleration voltage. The posts were made by a point exposure where the beam would dwell at each coordinate for 70 to 100 μs. Following this, the exposed samples were developed with a high-contrast salty developer solution of 4% NaCl and 1% NaOH in DI water at room temperature for 4 min. This was followed by a 2 min rinse in de-ionized water, a 10 s IPA rinse, and then dried with N_2 gas. Next, the samples were ashed with an O_2 plasma (50 W, 0.35 Torr) for 2 min to clean the surface and harden the HSQ patterns resulting in HSQ posts 38 $\pm$ 2 nm in height

Block copolymer self-assembly. After the template was made, they were chemically functionalized with either hydroxyl-terminated PS (11 kg/mol, PolymerSource) or PDMS brush (0.8 kg/mol, PolymerSource) by spinning the brush solutions onto the templated substrates and then heating in a vacuum oven (approximately 20 Torr) at 170°C for 16 h and rinsing with toluene. The PS brush coated substrates were coated with thin films of 45.5 kg/mol PS-b-PDMS (Polymer Source, Inc. P7517-SDMS, $f_{\mathrm{PDMS}} = .32$, $D_0 = 45$ nm, 2% PGMEA solution at 2650 RPM or approximately 1.5% cyclohexane solution at 8000 RPM) and a homopolymer of 1,350 kg/mol PS (Polymer Source, Inc. P620-S, 3% toluene solution at 7000 RPM) . The PDMS brush coated substrates were coated with thin films of 51.5 kg/mol PS-b-PDMS (Polymer Source, Inc., $f_{\mathrm{PDMS}} = .17$, 3% PGMEA solution at 6000 RPM) and a homopolymer

of 1,390 kg/mol PDMS (100,000 cSt Dow Corning 200 fluid 3% toluene solution at 7000 RPM).The solvothermal annealing chamber was saturated with a vapor resulting from a 5:1 by wt. mixture of toluene and n-heptane before the thermal quench initiated. The temperature profiles were monitored with a K-type thermocouple (Omega MWTC-A-K-915). Then a 5 s CF_4 RIE (50 W, 15 mTorr) was completed to remove the top PDMS wetting layer and was followed by a 22 s O_2 RIE (6 mTorr, 90 W) to remove the PS matrix and oxidize the underlying in-plane cylinder sphere forming ox-PDMS patterns. SEM images were obtained using the Elionix F125 at 125 kV accelerating voltage.

The device depicted in Figure 6.2 was built to track the changes that occurred in thin films of BCPs that were exposed to solvent vapors and then heated in this vapor environment. A N_2 carrier gas was bubbled through a mixture of toluene and n-heptane (5:1 by volume) to create a saturated vapor stream in the annealing chamber at ambient temperatures of 23°C which created vapor pressures of approximately 19.5 and 7.8 Torr of toluene and n-heptane respectively[92]. These were conditions that we previously found to not change the characteristic thin-film morphologies of in-plane cylinders for 45 kg/mol PS-b-PDMS (f_{PDMS}= 0.32) or close-packed spheres for 52 kg/mol PS-b-PDMS (f_{PDMS}= 0.16). A Si substrate coated with a polymer thin-film (45-70 nm) was placed in the solvent rich annealing chamber on top of an initially-off hot surface igniter and the swelling behavior of the polymer films was tracked within 1 s of introduction. After a time of 30 to 300 s a voltage was applied to the hot surface igniter which heated the films and then the effects of the heating was monitored with spectral reflectometry which supplied *in situ* film thickness measurements every 0.1 s.

The advantage of this system was the sequential two step nature of the process it enabled, where the thin film was first exposed to a saturated solvent vapor at ambient temperatures (23°C) and then exposed locally to heat, which helped determine the effects that each annealing step had on the final BCP morphology. Steps were taken to achieve *in situ* film thickness measurements relatively quickly (within 1 s) after the films were exposed to sufficiently saturated solvent vapors.

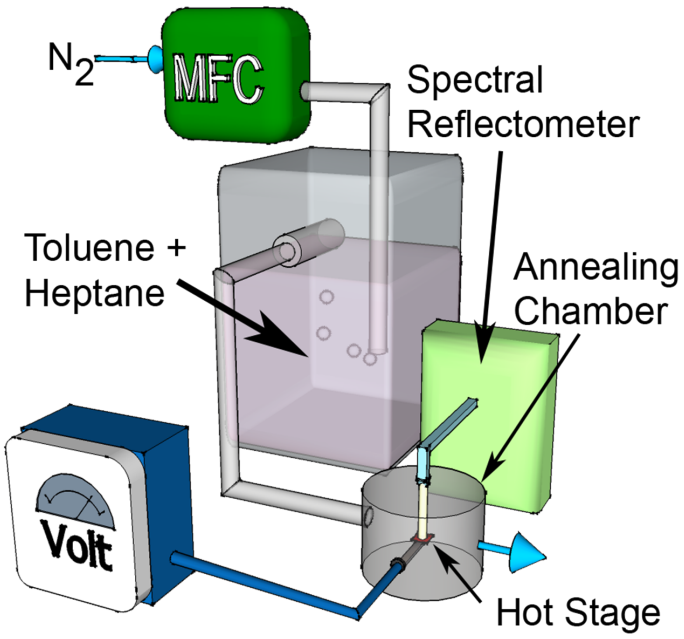

Figure 6-1: A schematic of the system constructed to study solvothermal annealing, which consists of a SVA followed by a thermal quench to remove the solvent in the film. A N_2 carrier gas passed through a solvent bubbler sending a saturated stream of solvent vapor to an annealing chamber where a Si substrate coated with a BCP rested on a silicon nitride resistor controlled by a variable voltage regulator. *In situ* spectral reflectometry monitored film thickness changes throughout the entire anneal.

6.3 Results and Discussion

Firstly, the transient swelling behavior of the thin films was explored. In Figure 6.3a, non-monotonic swelling behavior resulted after the polymer films were exposed to a high vapor pressure of solvents. The initial linear regime in this log-log plot indicated a fast mass uptake typical of case 1 diffusion, where there is no mechanical resistance of the polymer to the travelling solvent[138]. The higher rates of solvent incorporation and swelling found in the PDMS was expected due to its low Tg (-90°C) and correspondingly higher free volume available for diffusion at these ambient temperatures. The initial drop in swelling ratio likely corresponded to case 2 diffusion, where, after a critical amount of solvent entered the film and the polymers became plasticized and started to relax away from their previously kinetically trapped conditions that resulted from the spin casting, the polymers decreased the total amounts of kinetically-trapped free volume (similar to the specific volume behavior of an annealed metallic glass). Others have observed initial drops in solvent mass after the initial mass uptake and swelling of thin films[139], so it is possible that strain relaxation in the polymers might have temporarily released some amount of absorbed solvent. After the rate of free volume removal decreased and was counterbalanced by solvent incorporation, the film monotonically swelled until a desired swelling ratio, determined experimentally, was achieved. These three regions of initial mass uptake, polymer relaxation, and steady-state swelling behavior have been observed during *in situ* studies of toluene incorporation into polystyrene-block-poly(ethlyene oxide) system[140]. The initial dip in the swelling ratio was not observable if the thin films were inserted into a solvent-vapor-free annealing chamber before the flow-controlled SVA setup was turned on, as Chapter 2 detailed that this system took approximately 15 min to reach steady-state vapor conditions starting from ambient air conditions as the solvent vapor streams were introduced. Rather, the polymer thin films would gradually and monotonically swell as the vapor pressures increased and reached steady state conditions.

The difference in the magnitude of the dip in swelling ratio between the different polymer films qualitatively correlated with the T_g of the films and their total MW.

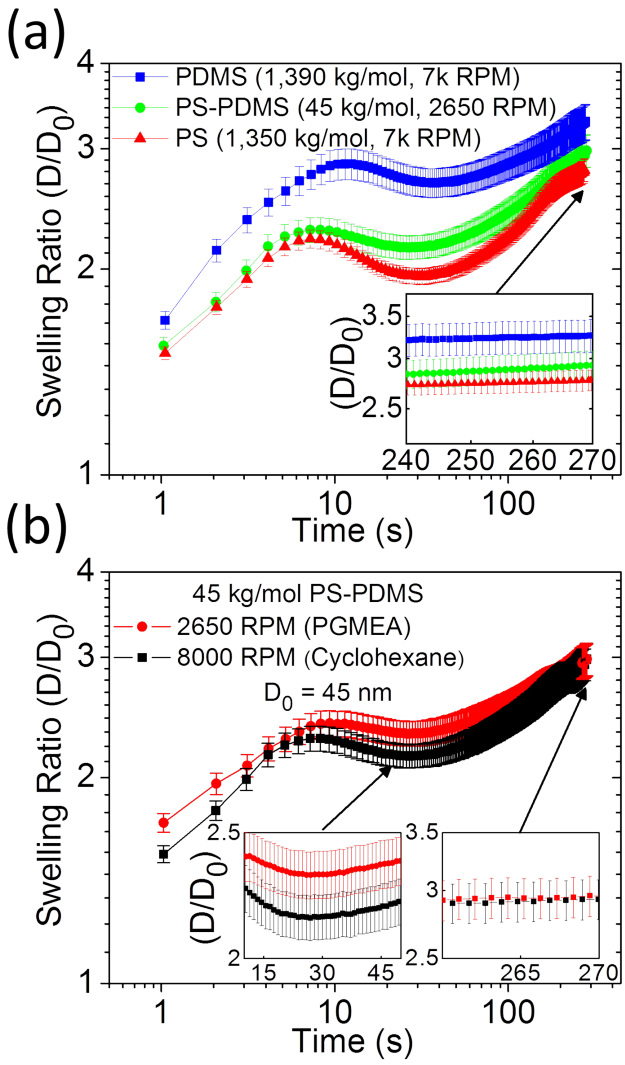

Figure 6-2: Swelling behavior of polymer thin films (PS-b-PDMS, PS, PDMS of D0 = 45, 82, 72 nm) after they were exposure to saturated solvent vapors consisting of a mixture of toluene and n-heptane. (a) Each film underwent a temporary drop in swelling ratio after the initial solvent uptake with the higher-MW higher-T_g PS experiencing the largest drop. (b) The magnitude of this drop depended in part on the spin-casting conditions used to prepare the films and indicated that different amounts of free volume were trapped in the film during spin casting depending on the rate that the polymer thin film was formed and that this rate could be changed by using different spin solvents and spin speeds.

(High MW homopolymers were used, especially in the case of PDMS, to prevent dewetting which can quickly occur in low molecular weight systems under these solvent annealing conditions and which can nullify and interfere with reflectometry measurements that assume continuous interfaces). To verify that the spin casting conditions were vital to determining the magnitude of the drop in swelling ratio, different spin speeds and solvents were used when casting a 45 nm thin film of 45 kg/mol PS-b-PDMS as shown in Figure 6.3b. When a lower spin speed and a higher boiling point (146°C) propylene glycol methyl ether acetate (PGMEA) spin-solvent was used, the BCP film was observed to form within approximately 6 s by noting the completion of the color cycling that occurred due to the gradual reduction in film thickness. When a higher spin-speed and lower boiling point cyclohexane spin-solvent was used, the BCP film was observed to form in < 1 s suggesting that the spun-cast polymers had less time to form lower-energy relaxed thin-film configurations and therefore likely had higher built-in strain and more free volume. Both films were spun for a total of 30 s to allow the spin solvent to evaporate out of the film after the initial film formation.

This spin casting hysteresis manifested itself within the first 30 s of the solvothermal anneal, where the quickly-formed cyclohexane-based film had a larger drop in swelling ratio relative to the gradually-formed PGMEA-based film and only finally caught up to the swelling ratio of the latter film after 270 s. We found that the slowly formed film had better microphase separation after the solvothermal anneal when compared to the more quickly formed film after 270 s of solvent vapor exposure, and this likely followed because the total effective time for self-assembly in a dynamic system such as this is proportional to the total area under the swelling ratio vs. time curve, as an increased swelling ratio decreases χ and increases diffusivity/mobility for a self-assembling system. I.e. the faster that a BCP film can reach a desired swelling ratio, the faster that an anneal can be completed. This means that future comparisons of fast annealing times should mention the time required for the formation of the BCP film, as there can be a trade-off between deposition speed and the amount of non-monotonic swelling behavior that can delay how quickly a film reaches a desired

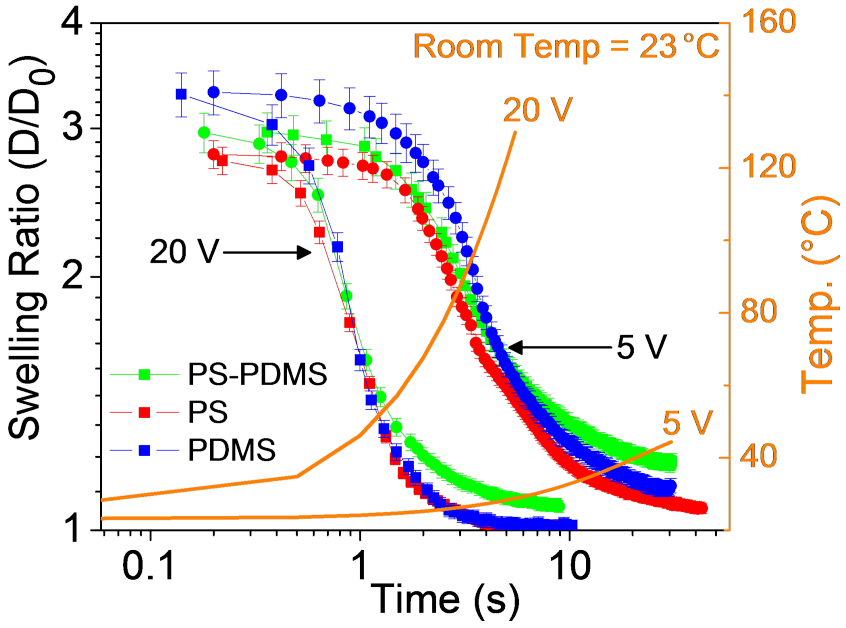

Figure 6-3: After the polymer films reached a given swelling ratios, a voltage to the resistive substrate holder was applied (here defined as t=0) causing the thin films to undergo temperature increases which resulted in drops to the swelling ratio as the solvents molecules in the films were boiled out. Depending on the rate of temperature increase, which was controlled by the applied voltage, different rates of collapse were achieved; and depending on the final temperature reached, different steady-state swelling ratios were achieved. The two quenching behaviors shown (5 and 20 V) indicate the slowest (approximately 10 s) and fastest (approximately 1 s) film collapses that were explored in this study.

swelling ratio and self-assembles.

After the films were allowed to swell, the effects of locally heating the sample in ambient solvent conditions were explored. The thermal quenching step of the solvothermal anneal resulted in a gradual film collapse as shown in Figure 6.3. This change in swelling ratio was analogous to that explored by others[70,141] where vapor pressures during the SVA were gradually decreased; but instead of requiring many minutes to gradually dilute and reduce the solvent vapor pressures, the thermal quench required seconds and seemed to have analogous levels of improvements to the self-assembly that were shown in the controlled film collapse studies. The time required for the homopolymer and BCP films to collapse could be controlled by changing how

fast the substrate heated. The temperatures reached during the quench determined the amount of solvent left within the film. At lower temperatures, the films finished with swelling ratios less than 1.3, which is insufficient for this system to undergo any meaningful self-assemblies under these short time-scales. When compared to typical quenching/solvent removal steps, which reduce the solvent vapor pressure above the substrate at varying rates, the films in the solvothermal anneal are quenched under saturated solvent conditions which could affect the top-film surface energies and therefore effect the self-assembly by, for example, creating neutral or strongly attractive boundary conditions for the different blocks although this effect was not noticeable when the microdomain morphology was analyzed. After the swelling and quenching behavior was determined, the quality of the self-assembly for two systems, a monolayer of spheres and a bilayer of cylinders, was analyzed by reactive ion etching of the majority block PS matrix with O_2 to and imaging the oxidized-PDMS structures with a scanning electron microscope (SEM).

The first example system, a templated monolayer of sphere forming 52 kg/mol PS-b-PDMS, is characterized in Figure 6.3 which succinctly exemplifies the separate solvent uptake and thermal quenching steps of a solvothermal anneal and points to the complexity of the many different swelling ratio paths that are possible to explore (i.e. rate of solvent uptake, swelling ratio to achieve, rate of solvent removal, etc.). This experiment reproduced our previous work where an 18 hour thermal anneal at 170°C was used on an e-beam lithography templated Si substrate with a PDMS brush to achieve a highly ordered arrangement of spheres. A high BCP mobility was expected due to the PDMS brush-coated Si and due to the lower minority volume fraction of PDMS as seen by others. We determined that the anneal could be completed within 30 seconds by allowing the film to reach a swelling ratio of 2.3 before a quench was initiated. This BCP system was quenched before any non-monotonic swelling behavior was visible and resulted in analogous quality of self-assembly when compared to the thermal anneal. For the second system, a templated bilayer of cylinder-forming 45 kg/mol PS-b-PDMS, the solvothermal annealing profile consisting of that shown in Figure 6.3(a), where a swelling ratio of approximately 2.8 was reached, combined with

the 5V thermal quench in Figure 6.3 was found to result in similar quality self-assembly when compared to our previous work, where we found that periodic arrangements of posts made with e-beam lithography and functionalized with majority-block PS-OH brush could template the self-assembly of a bilayer of cylinders to produce ordered 3D crossbars structures after a 3 hr SVA. A detailed discussion of the solvothermal anneal of the bilayer are explored below.

First, the amount of swelling required for a bilayer of cylinders required was determined. The film began as disordered micelles, Figure 6.3(a), so a sufficient amount of time was needed in order that the BCP PDMS cylindrical microdomains could separate from one layer of disordered domains into two layers of cylinders that could be templated. After this amount of time, which was 270 s for this system, a thermal quenching step resulted in changes to the film swelling ratios as previously shown Figure 6.3.

Many changes occur in a short amount of time during a thermal quenching step. In general, as a solvent is removed, diffusivity rates for the BCP should decrease as the effective χ parameter increases. However, an increase in temperature can counteract this to some extent as both the diffusivity and χ are dependent on it. The annealing trends were very clear that even after the BCP films reached a set swelling ratio, a few seconds (1-10 s) difference in solvent removal rate could drastically affect the qualities of self-assembly that resulted as shown in Figure 6.3 (a-d). Here, we found that the higher rates and the higher maximum temperatures reached resulted in a much lower quality self-assembly, Figure 6.3a, when compared to the lower rates and the lower maximum temperatures as in Figure 6.3d.

Finally, in order to verify that the thermal quench was vital to determining the quality of self-assembly for this BCP system, a comparison was made to different aspects of the anneal as shown in Figure 6.3. In Figure 6.3(a), the micrograph shows the initial morphology of a 45 nm BCP film immediately after spin casting with PGMEA followed by RIE. After a high-temperature thermal anneal, as shown in Figure 6.3 (b), a small amount of self-assembly resulted, as indicated by the very small domain size of the in-plane cylinders formed and by the lack of a visible post

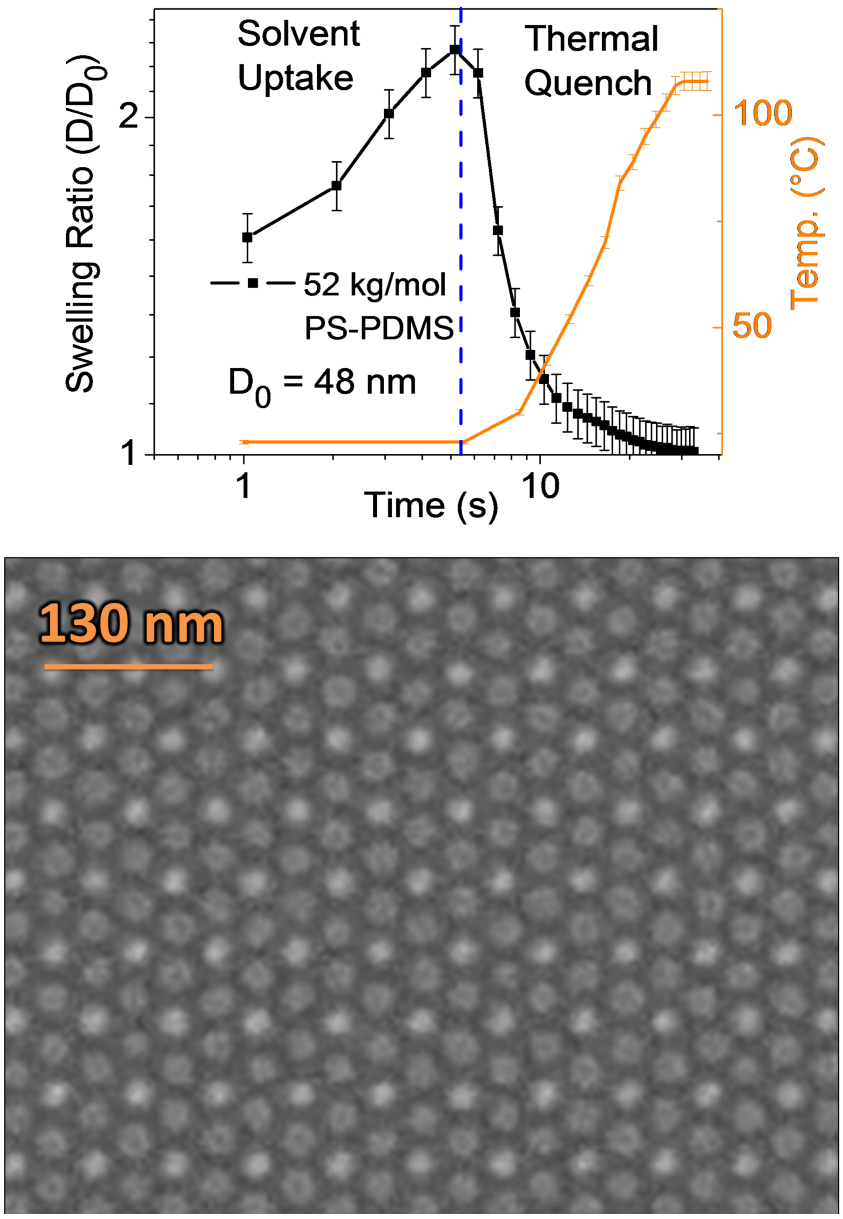

Figure 6-4: A short time (30 s) solvothermal anneal was required for a monolayer spheres. (a) The entire solvothermal anneal is shown whereby an initial solvent incorporation step is used to swell the film to a critical value before a thermal quench boils off the solvent. (b) An SEM micrograph after RIE showing that this fast solvothermal anneal resulted in highly ordered templated self-assembly of a monolayer of spheres.

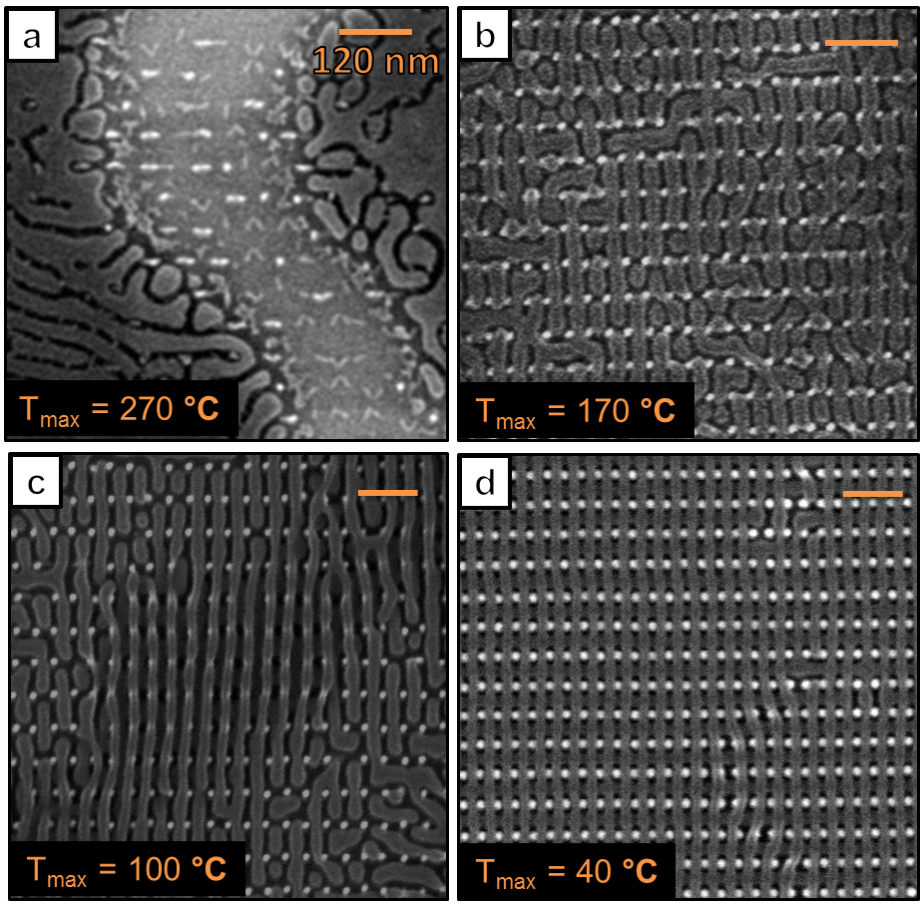

Figure 6-5: Top down scanning electron microscope (SEM) images showing vastly different qualities of templated self-assembly of a bilayer of PS-b-PDMS after the films were each allowed to reach a same swelling ratio of approximately 2.8 and then were exposed to different heating regimes that collapsed the films at different rates and reached different maximum temperatures. $(a)-(d)$ show the fastest $(1s)$ to the slowest $(10s)$ film collapses with each accompanied by different maximum temperatures.

template (approximately 38 nm in height) which should repel the PDMS domains of a moderately mobile BCP due to the PS brush coating the posts. When this annealing setup was used only as a SVA, with no thermal quench, for an entire hour, a moderate but poor amount of templated self-assembly occurred as in Figure 6.3(c). Both Figures 6.3(b,c) show the effects of what typically would be thought of as a higher drive towards self-assembly, i.e. higher temperatures (6.3 b) and longer SVA times (6.3c), then what is done on either of the solvothermal annealing steps as shown in Figure 6.3d, where a comparison is shown between our previous work requiring a 3 hr SVA versus a 5 min solvothermal anneal (270 s solvent incorporation + 30 s quench). Controlling the swelling ratio and heating paths that a given BCP system undergoes are important for finding the fastest and highest quality annealing process available.

6.4 Summary

This chapter described a novel solvothermal annealing method developed that encompasses a SVA followed by a thermal quench which was able to quickly anneal the templated BCP systems explored here, but is applicable to any BCP system with the appropriate choice of solvent vapors and processing temperatures. Attention was paid to the polymer film casting conditions as these were found to be important and could result in changes to the quality of self-assembly with the hysteresis of these conditions being manifested during the *in situ* monitoring of the non-monotonic swelling behavior. This annealing strategy enables fast self-assembly times which is very important if the DSA of BCPs is going to be a viable candidate for next-generation lithography.

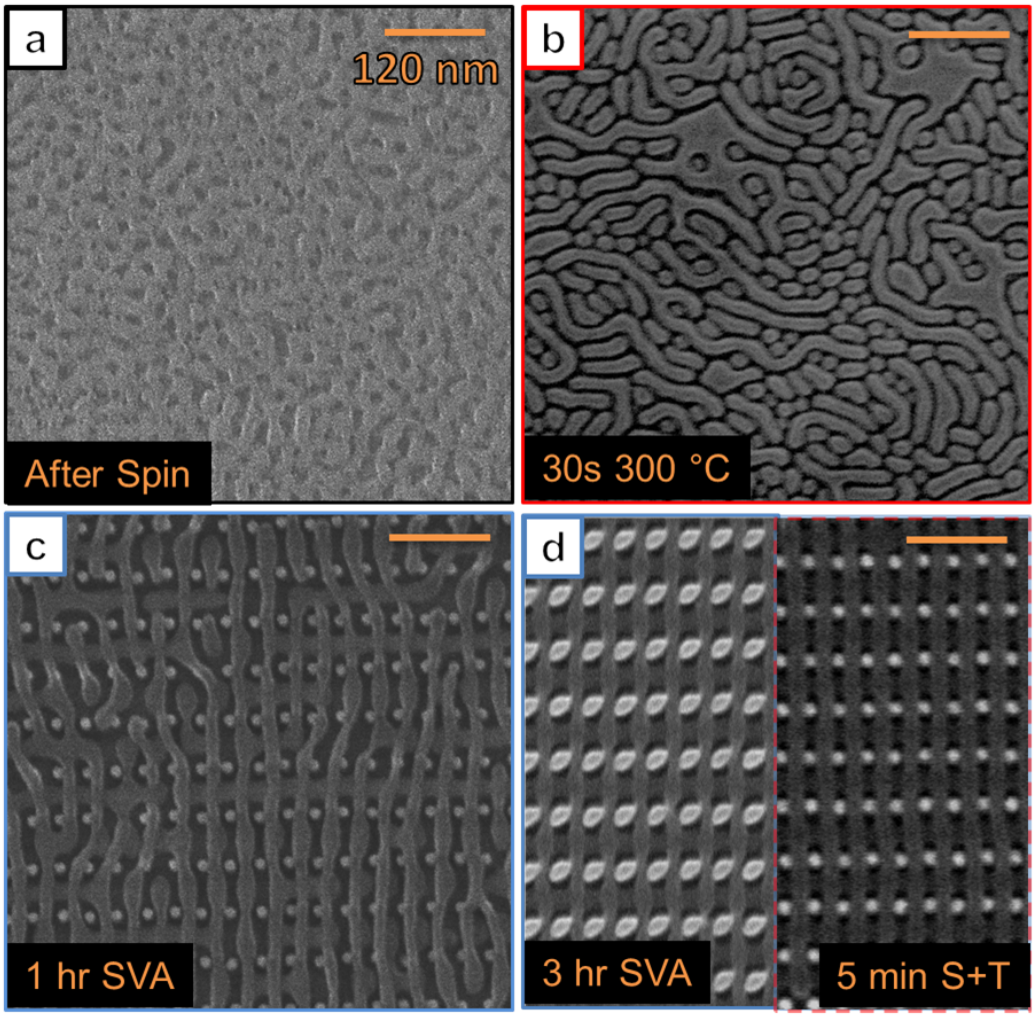

Figure 6-6: Micrographs of different annealing stages showing (after RIE) a cylinder forming 45 kg/mol PS-b-PDMS (a) after spin coating, (b) after just a high temperature thermal anneal, and (c) after just a 1 hr solvent vapor anneal (SVA). (d) A comparison between a 3 hr SVA, left box, and a 5 min solvothermal anneal, right box.

Chapter 7

Conclusion and Future Work

This thesis explored the capabilities of the polystyrene-block-polydimethylsiloxane block copolymer (BCP) system by investigating a number of solvent annealing strategies and by applying these strategies to facilitate novel templated self-assembly experimentation. The basic solvent annealing setup, with modifications to how fast the solvent was allowed to leave the film and with subsequent etching, enabled for example perpendicular features of cylinders or lamellae to form throughout thick films (>100 nm) which was difficult to envision being possible for these high-chi BCP systems.

Chapter 4 delved deeper into the work on a flow system to better control the solvent vapor annealing. The lack of a high degree of control of the basic solvent annealing setup, described in Chapter 2, is what prompted this work that explored fundamental differences between the types of solvent vapor environments that could be formed when the solvent liquids were separated and mixed together in a steady-state stream versus the vapor environment formed from mixed solvent liquids. Due to the non-idealities present in the toluene $n-$heptane system that was used, these differences were found to be important. The flow controlled solvent vapor annealing setup allowed for systematic and reproducible exploration of the the individual solvent vapor pressures and the connection to the resulting morphologies that the block copolymer film would undergo during the annealing. This control allowed for interesting comparison between experimental and simulated self-consistent mean field theory results.

With a better understanding and grasp of how to control of the self-assembly of BCPs with solvent annealing, experimentation on templated self-assembly was completed with a number of interesting finds. In Chapter 5, many different phenomena were explored that were enabled by simply changing the chemical functionalization of the post templates that were fabricated using electron beam lithography. Previous work in this area used a PDMS-OH brush functionalization which caused the posts to attract the minority-block domain of PDMS cylinders or spheres, our templated work used PS-OH as a brush which tended to repel these microdomains. Working with repulsion instead of attraction actually enabled a higher degree of control especially when moving to three dimensional self-assembly.

Typically, the experimentation in this thesis involved annealing steps that lasted on the order of 1 to 3 hours or longer. In the latter part of my work, I explored the possibility of bringing this annealing time down to the seconds and minutes timescale. This proved successful and the strategy is explored in Chapter 6. By decoupling the temperature of the polymer film from the solvent vapor environment, solvothermo annealing was a method developed where solvent was allowed to incorporate into the film and then was thermally quenched and removed by the application of heat at the polymer film. This method drastically reduced the required annealing times and hints towards possible industrial applications where self-assembly needs to be completed quickly in order to be economically feasible.

7.1 Suggested Future Work

7.1.1 Rapid Solvothermal Annealing

Although the shorter annealing times that were reached in the solvothermal annealing experiments were quite low, I do believe that they can be made even lower. The trick to doing this involves taking this methodology to even higher temperatures, and it involves being able to expose a polymer film even more rapidly to a high vapor pressure solvent environment. Currently, groups that are looking to improve upon

the annealing time are simply adding heat and solvent simultaneously. I believe that the best strategy is to take advantage of the decoupling of the temperatures of the polymer film and of the solvent vapor environment.

If the solvent vapor environment and the polymer film are heated as one system, then you run into limitations that have already been experienced by others in the field. This is due to the difficulties, for example, of making sure there are no temperature fluctuations in the vicinity of the polymer film. If there are, then any subtle decrease in temperature of the polymer film relative to the solvent vapor environment will result in some amount of condensation of solvents onto the polymer film. If condensation occurs, then the droplets tend to break up the polymer film and cause dewetting and other undesirable effects resulting in a failed anneal. It is therefore necessary to ensure that the temperature of the polymer film is controlled such that the desorption rate of the solvent molecules is high enough to prevent droplet formation and further condensation independent of what the solvent adsorption rate is, which is a function of the solvent vapor environment temperature. Simply put, we need to ensure that the temperature of the polymer film is slightly elevated above the temperature of the solvent vapor environment.

If this level of control could be achieved, then solvothermal annealing could be initiated at temperatures above the ambient temperatures that were used during my thesis. For example, consider the case where a polymer film at 81°C is introduced to a solvent vapor environment at 80.5°C. (As a comparison, in my thermal annealing experiments, polymer films at around 24°C were introduced to solvent vapor environments at the same temperature.) At these elevated temperatures, there would be a couple of different advantageous effects. One is that the population of solvent molecules in the vapor environments would be higher due to the higher temperatures of the liquid solvent bath. The other difference would be that the solvent molecules themselves would have higher amounts of thermal energy to facilitate faster diffusion.

During the first part of a solvothermal anneal, where we were waiting for a certain population of solvent molecules to enter and swell the film, the faster that the film could be swollen, the faster that the total anneal (including the thermal quench) could

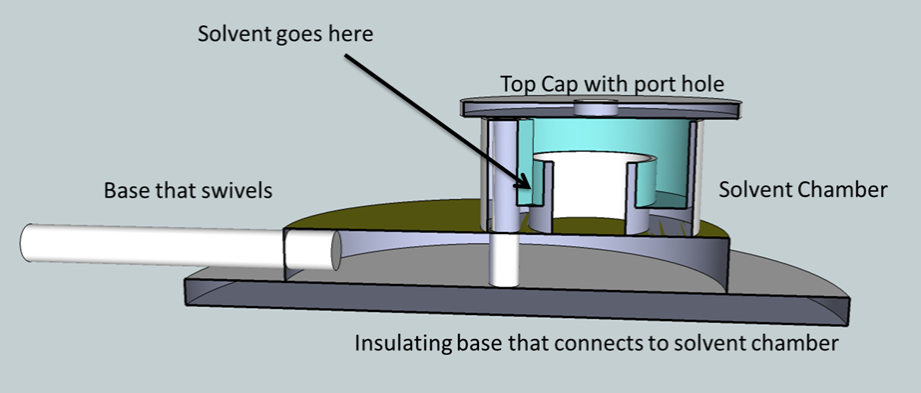

Figure 7-1: A schematic of a potential prototype to facilitate rapid thermal annealing.

be completed. Beginning the solvent incorporation at elevated temperatures and controlling the polymer film temperature to prevent condensation and drop formation would allow the polymer film to reach the desired swelling ratios at much faster rates. This would be due to the increased initial concentration of solvent molecules at the diffusion front (beginning at the top of the polymer film) due to the higher vapor pressures and higher solvent population and due to the increased kinetic diffusion rate due to the higher temperatures of the diffusing solvent molecules. Since the vapor pressures and the diffusion rates would both increase and since both are exponentially dependent on temperature, by increasing the temperature from 24 to 80°C the initial solvent swelling step would be predicted to be finished extremely fast (on the order of a couple seconds for the systems I explored). This would even be true for the bilayer crossbar structure that during my studies required over four minutes for the initial solvent swelling step. I believe, based on my experience, that it could be done in 10 s or so with such a setup. This is especially true considering that the current glass chamber setup would not allow for rapid exposure of the polymer film to a completely saturated solvent vapor environment. This was because it was required that the quartz window was opened slightly for the introduction of the polymer film allowing for some amount of solvent vapor to escape.

Taking these points into consideration, I initiated some exploration of building such a rapid solvothermal annealing system. The system would consist basically of the

following: 1) A metallic temperature-controlled base with a trench where a small Si substrate could be placed. 2) A stationary solvent annealing chamber containing small amounts of solvent liquid that was temperature controlled to increase the solvent vapor pressure. The top of the solvent annealing chamber would have a quartz viewing port where spectral reflectometry measurements could be done. 3) A mechanism by which the base could be rotated rapidly to introduce the trench (containing the polymer film on the Si) to the vapor environment created by the solvent annealing chamber. 4) Temperature controllers that would allow the base and the solvent annealing chamber to reach separate setpoint temperatures that would be controlled through feedback from embedded thermocouples.

A device such as this would have many advantages, including those mentioned above. Additionally, the amount of solvent waste would be drastically reduce compared to the flow controlled system which is constantly out-gassing solvent vapor to the environment. An example of a foreseen experiment would go as follows: 1) Set the temperature of solvent annealing chamber to 80°C, and the base to be 80.5°C. 2) Wait at least 15 minutes until the solvent vapor chamber reaches equilibrium and place the polymer film in the base trench. 3) Initiate the rotary motor that rotates the sample into the annealing chamber and stops underneath the spectral reflectometer beam measuring the swelling behavior in situ. 4) Once the polymer film reaches a desired swelling ratio, initiate a temperature increase on the base to 90°C or so and drive the solvent molecules out of the polymer film. 5) When the swelling ratio is < 1.5 initiate a rotation that removes the sample from the annealing chamber, and the experiment is finished.

The important parameters that will determine the quality of the self-assembly will be: 1) The swelling ratio reached before the thermal quench starts. 2) The temperature of the entire system when the polymer film reaches said swelling ratio. 3) The rate at which the film collapses during the thermal quench.

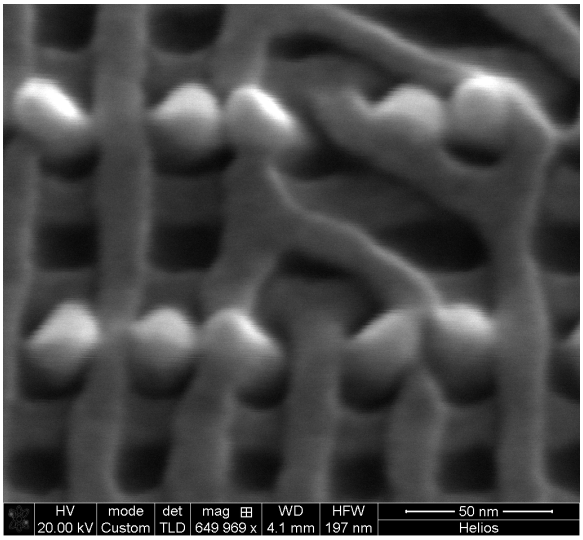

Figure 7-2: Pairs of collapsing posts could be the cause of self-assembled cylindrical inter-layer junctions that connect the top and bottom layers.

7.1.2 Controlling 3D Interconnects

Our work on 3D bilayer self-assembly resulted in some fascinating discoveries. The ability to independently control the orientation and direction two layers of in-plane cylinders of PDMS is a very exciting prospect, and there are still many areas to explore here. One area in particular would be the ability to control when a cylinder in a given plane switches between layers in the bilayer film. For example, if particular post placement would force a cylinder on the bottom layer to jump in a continuous manner (keeping the connectivity of the cylinder domain) to the top layer this could result in very useful levels of self-assembly control.

In some of our work on 3D bilayer self-assembly, we occasionally encountered defects that exhibited this type of behavior, but it was not intentional, as in Figure 7.1.2. Typically when the post patterns were created a dose matrix was done to account for various experimental changes that could occur from day to day (beam stability, development temperature/rate, etc.). The post patterns that received the lowest dose of electrons tended to have lower levels of cross-linking density within the negative resist of HSQ. This resulted in posts with generally lower moduli that tended to collapse upon further processing. I believe that it is possible to control post collapse

to force cylinders in a given layer to alter their trajectory and change layers. In Figure 7.1.2, it appears as if this post flexibility is one cause of the inter-layer defects.

An experiment to test this hypothesis would do the following: 1) Create a post template that results in a 90° crossbar structure after BCP self-assembly, but use a variable dose post pattern to create pairs of posts within the post template that have a lower stiffness (use a lower dose) and therefore a higher likelihood of collapse. 2) Test pattern dose layout requirements multiple times to determine the critical dose required for post collapse during self-assembly that initiates an interlayer defect. 3) Test whether subtle post placement alterations (I.e. move pairs of posts that are supposed to collapse closer together) that deviate from the ideal post lattice facilitate more reproducible post collapse. If it is possible to precisely control when a cylinder changes layers, then this method enables for example the ability to create self-assembled cross-point memory devices. For example, consider a simple crossbar structure where the outer boundaries of the post patterns are engineered to collapse and facilitate a transition where all of the bottom layer cylinders move to the top layer continuously. If we could then use a method such as atomic layer deposition to metallize all of these self-assembled cylinder wires, then the final pattern that would result from this is a crosspoint memory device where we have direct access to all of the relevant contacts because they would be in the top layer. This would be a step towards solving the problem of how exactly to apply voltages to lower levels of metallic wires deep in a self-assembled film.

7.1.3 3D TEM Tomography

Continuing on the theme of the bilayer self-assembly work, we have started to initiate some experimentation on being able to image the self-assemble bilayer structure before destructive reactive ion etching is done.

If self-assembled bilayer BCP films templated with posts of HSQ or PMMA could be fabricated on in the center region of large (1 mm x 0.1 mm) substrate of a < 50 nm thick suspended silicon nitride, it may be possible to use a tilt sequence of TEM images to reconstruct the 3D morphology of the self-assembled microdomains. The

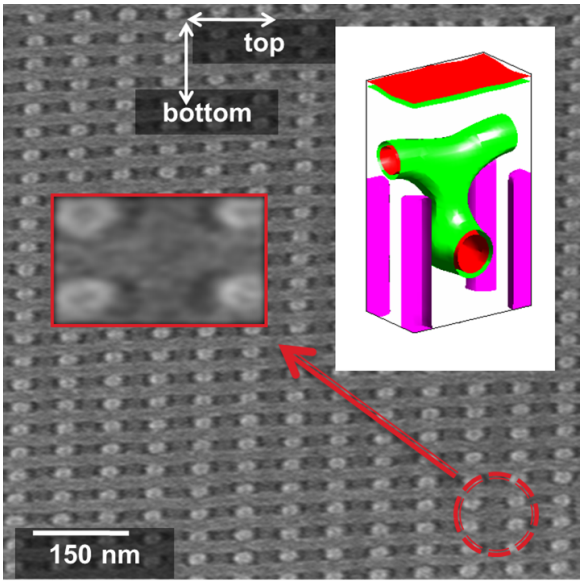

Figure 7-3: Possible regions showing inter-layer four-way junctions. These defects are predicted to exist with SCFT.

trick to getting the experiment successfully completed is doing the entire fabrication process on 3 mm diameter silicon nitride TEM grid. Initial TEM imaging being done at NIST shows great promise in being able to produce 3D morphology data with a predicted spatial resolution of 5 nm. At this level of resolution, we will be able to compare the predicted SCFT morphology with the experimental results. This will give us a great amount of insight into the effects of, for example, solvent vapor annealing and solvent vapor removal during quenching, which results in the collapse of the cylindrical microdomains during the self-assembly of the 3D crossbar structure. It is necessary to determine whether or not connections exist at the crosspoint locations where the bottom layer is immediately below the top layer of cylinders. SCFT energy calculations currently indicate that the existence of a connection results in a negligible energy penalty, but this model ignores the path dependence of the self-assembly that occurs in the experiments due to the large amount of swelling and deswelling that occurs during the solvent vapor annealing which may facilitate a higher probability of disconnect between the top and bottom layers as they are stretched vertically during the swelling.

7.2 Looking Ahead

The future of SVA looks very promising, but there are some difficulties remaining in this topic. This work and others have started to realize that controlling many variables simultaneously is going to be necessary for achieving manufacturing levels of control. Consider temperature as an example. When controlling for temperature during a SVA, the temperature of the solvent vapor and the substrate must be precisely controlled. Many of the important processes, such as the vapor pressure, swelling ratio, and polymer/solvent diffusion rates are all exponentially dependent on temperature and interdependent to each other. The exponential dependence of these important quantities points to the engineering challenge of constructing such a system.

An annealing BCP substrate inside a temperature controlled solvent vapor needs pathways for the thermal energy keeping the annealing BCP at a controlled but steady temperature. The engineering challenge lies in trying to control steady state temperatures of two coupled systems, but it seems to be necessary especially if future solvothermal anneals need a step of constant swelling ratio condition for a given time, because this would require that the substrate be heated at a slightly elevated temperature (1 or 2°C). Without proper thermal pathways, the substrate heating would heat the solvent vapor which would then reach higher pressures and swell the polymer more resulting in complicated feedback mechanisms to control for.Additionally, if the temperature of the substrate varies to far below that of the solvent vapor, condensation of liquid solvent droplets would occur and render the anneal useless.

If these challenges were overcome, a large amount of science could be done on the effects of many parameters such as vapor pressures of one or more solvents, swelling rate, temperatures of substrate relative to their T_g, and annealing time on the quality of a self-assembled film. Additionally, my work has shown that the effects of the precise BCP film casting conditions can have a hysteresis effect on the SVA, so a better understanding of the proper way to prepare a BCP before a SVA is required, but little work has been done in this area. Scientific understanding of these effects will require a combined approach with theoretical modeling, but SCFT may not be

the solution here, as a real solvent vapor anneal experiences many transient behaviors that may be better suited to understand with coarse grain particle models that allow swelling and that can track the location of solvent vapors in and out of the films as has recently been approached[142].

For SVA to become industrially viable, other considerations have to be taken into account that are usually ignored in an academic setting such as the environmentally friendliness of a process (this is of course due to the minuscule amount of waste that an academic source would contribute compared to an industrial source). Supercritical CO_2 is looked at as one possible solution for solvent annealing due to its abundance and non-toxic nature[143,144], although a polymer system needs to be designed that allows for selective swelling of each block, as studies on the PS-PMMA system show that sc-CO_2 is not a viable annealing agent for inducing long range order in this BCP system[145]. Now that researches have shown BCP proof of concept for many applications, an effort should be made to find BCPs that for example 1) have industrially friendly synthesis precursors, 2) have blocks that selectively swell to environmentally friendly solvents like water, 3) have a high etch selectivity, 4) have a high χ parameter to enable small features, and 5) are capable of being uniformly cast as thin films.

If the aforementioned solvothermal annealing chamber can be properly engineered, it offers one possible solution for an almost zero-solvent-waste solvent anneal due to the closed nature of the system. When a solvothermal anneal is finished, and the substrate is heated, a majority of the solvent is removed from the BCP film and it could theoretically be pulled out of the chamber with a minimal amount of accompanying solvent vapor. Additionally, the solvent vapor that does escape through the exit, could be condensed further back into a liquid state if the BCP film passed through an intermediary step at reduced temperatures so long as the reduced temperatures do not strain the BCP enough to induce defects.

If these and the accompanying engineering challenges can be overcome, I believe it can result in a manufacturing-friendly solvent anneal that is superior to thermal annealing and will enable many of the mentioned scientific questions to be explored.

Appendix A

Supplementary Information

A.1 Self Consistent Mean Field Theory Code

The following is the complete Mathematica code for 2D SCFT. It can be useful to see how the SCFT solving iterations for the diblock copolymer system is actually done. Mathematica is far removed from assembly language (unlike programming in C), so this code is quite slow. However, the plus side is that Mathematica is very succinct and human readable, which is useful for helping to understand how different steps are conceptually completed in the code. When the steps are understood, it is more straightforward for implementing the solver in C or C++.

```
Clear["Global`*"]

(*Initialization Conditions*)
NX = 8;     NY = 8;     NZ = 1; (*Finite Element Simulation Box Size*)
LX = 1 * L0;  LY = 1 * L0;  LZ = 1;  L0 = 3.5; (*Size of grids relative to polymer size*)
NS = 50; f = 0.5; NA = Floor[f * NS]; NB = NS - NA; G = 1000; xN = 24; (*Polymer chain length,
volume fraction, number of A block, Ginsberg, Flory Huggins*)
Δt1 = 5.0; Δt2 = (2/3 Δt1)/G; Iterations = 10000; σNoise = 0.1; μNoise = 0.65;
(*SCFT step sizes. This is empirically found*)
FieldNoise = RandomReal[NormalDistribution[μNoise, σNoise], {Iterations, NX, NY, NZ}];
(*Noise for temperature fluctuations*)
ρDeviationCap = 0.03; μdevcountmax = 0;
ΔSk2[NN_, LL_, i_] := NN/(NS LL) (2 π/NN (NN/2 - Abs[(i - 1) - NN/2]))^2;
expΔsk2 = Table[e^(-ΔSk2[NX,LX,i]-ΔSk2[NY,LY,j]-ΔSk2[NZ,LZ,k]), {i, NX}, {j, NY}, {k, NZ}];
(*Value needed for psuedospectral method*)
(*The following just initialize arrays in memory for each field and propagators solved
 during the SCFT calculations*)
iΩPlus = ConstantArray[0, {NX, NY, NZ}];
ΩMinus = ConstantArray[0, {NX, NY, NZ}];
ωFree[s_] := Piecewise[
    {{iΩPlus[[All, All, All]] - ΩMinus[[All, All, All]], s ≤ NA},
     {iΩPlus[[All, All, All]] + ΩMinus[[All, All, All]], NA + 1 ≤ s ≤ NS}}];
qDbk = ConstantArray[0, {NS, NX, NY, NZ}];
qDbk[[1, All, All, All]] = 1;
q†Dbk = ConstantArray[0, {NS, NX, NY, NZ}];
q†Dbk[[1, All, All, All]] = 1;
```

```
(*The SCFT loop follows:*)

Do[

(* Calculate q(r⃗, s + Δs) & q†(r⃗, s + Δs) *)
s = 1;
Do[
        qDbk[[s + 1]] = Flatten[ e^(ωFree[s]/(2 NS)) InverseFourier[
                exp△sk2      Fourier[e^(ωFree[s]/(2 NS)) qDbk[[s, All, All, All]]], 0], {s, 1, NS - 1}]
  Do[
        q†Dbk[[s + 1]] = Flatten[ e^(ωFree[NS-s+1]/(2 NS)) InverseFourier[
                exp△sk2      Fourier[e^(ωFree[NS-s+1]/(2 NS)) q†Dbk[[s, All, All, All]]], 0], {s, 1, NS - 1}]

  (* Calculate Q, ϕA, and ϕB *)
  Q = 1/(NX NY NZ) Total[Flatten[qDbk[[NS]]]];

ϕA = (Q 3 NS)^-1 (                                  qDbk[[1]] q†Dbk[[NS]] +
        Sum[(2 + 2. KroneckerDelta[Mod[s, 2], 0]) qDbk[[s]] q†Dbk[[(NS + 1) - s]], {s, 2, NA - 1, 1}]
                                                  + qDbk[[NA]] q†Dbk[[NB + 1]]);
ϕB = (Q 3 NS)^-1 (                                  qDbk[[NA + 1]] q†Dbk[[NB]] +
        Sum[(2 + 2. KroneckerDelta[Mod[s, 2], 0]) qDbk[[s]] q†Dbk[[(NS + 1) - s]], {s, NA + 2, NS - 1, 1}]
                                                  + qDbk[[NS]] q†Dbk[[1]]);

(* Check Deviations in ϕA + ϕB = 1 *)
ρDeviation = Sqrt[Total[Flatten[(ϕA + ϕB - 1)^2]]/(NX NY NZ)];
(* Update iμ+and iμ- *)
If[ρDeviation > ρDevationCap ∧ μdevcountmax < 6,
  iμPlus += LX LY LZ/(NX NY NZ) △t1/2 (ϕA + ϕB - 1);
  iμPlusNormalize = Total[Flatten[iμPlus]]/(NX NY NZ);
  iμPlus -= iμPlusNormalize;
  μdevcountmax += 1;,

  μMinus = μMinus + LX LY LZ/(NX NY NZ) G △t2/2 (ϕB - ϕA + (2 f - 1) + 2/xN μMinus) + Sqrt[△t2] FieldNoise[[Iter]];
  μdevcountmax = 0;]

(*Do this 'Iterations' number of times*)
, {Iter, 1, Iterations}]
```

A.2 Spectral Reflectometry

This section gives a brief explanation of spectral reflectometry which was used throughout this thesis work. The two most popular optical methods for measuring film thickness are ellipsometry and spectral reflectometry. Reflectometry measures over a wide range of wavelengths the amounts of light that reflects off a surface normal to the incoming light beam. Ellipsometry measures reflectance of polarized light at non-normal incidence. Using reflectometry allowed for the chamber design to be simplified, as a beam of light could simply reflect perpendicular to the surface, instead of having multiple quartz windows required at the incident and reflection angles.

The index of refraction, both the real and complex components (n and k), are one measure of how light propagates through a film. The time-independent propagation of an electromagnetic field through a material can be given by:

$$E = A_0 \cos\left(n\tfrac{2\pi}{\lambda}x\right) e^{\left(-k\frac{2\pi}{\lambda}x\right)}$$

The real component of the refractive index, n, measures the effective speed of light in the material relative to the vacuum speed. As a photon is traveling through a material it is constantly being absorbed and reemitted at the given wavelength. Between these absorption and reemission events, it is traveling at the vacuum light speed, c, but because these events take a finite amount of time, effectively the photon speed decreases (even though it's not the same identical photon, it is still a useful concept to use an effect speed relative to the light speed, as it gives a sense of how often photons are being absorbed and reemitted as it travels through a material.). The effect on the electromagnetic field is a change in the real space distance between peak to peak maximum intensity values. Hence, n is found in the cosine component.

Some fraction of these absorption events are permanent though, and the complex component of the index of refraction, k, also known as the extinction coefficient, measures the amount of light absorbed at a given wavelength. Hence, k is found in the exponential decay factor of the electromagnetic beam.

When reflection occurs at a single interface, it can be shown that the fraction of light that is reflected, R, is a function of the real and complex parts of the index of

refraction:

$$R = \frac{(n-1)^2+k^2}{(n+1)^2+k^2}$$

When light hits the polymer sample for example, there are two interfaces where reflection occurs: the top polymer-air interface and the bottom substrate-polymer interface. Due to the wavelike nature of light, the two reflected beams can either constructively or destructively interfere depending on their phase relationship. The phase relationship is determined by the optical path length difference which is a function of the film thickness, d, and the index of refraction as a function of wavelength. The reflections are in phase when $2nd = i\lambda$, where i is an integer.

One limitation of spectral reflectometry is that for very thin films, where the light does not complete a full oscillation in amplitude as it travels through the film and reflects back, it is very difficult to get an accurate measurement. In these cases, ellipsometry is better, as incident like coming from an angle effectively passes through a thicker film when compared to the spectral reflectometry beam which passes normal to the film. The F20 system used in this thesis work had the additional deuterium light source in order that smaller wavelengths of light were used. This gave a thickness measurement range of 3 - 20,000 nm.

A.3 Mass Flow Controllers

This section gives a brief overview of how mass flow controller (MFC) operates. This is intended to be supplementary information that helps rationalize some of the choices mentioned in Chapter 2, where the setup of the flow controlled solvent vapor annealing is discussed.

An MFC is basically composed of three components: a bypass, a sensing tube, and a control valve. A bypass provides a path for much of the incoming gas flow to enter and pass through to the control valve. Its other function is to allow a small amount of gas to enter into the sensing tubes, where the gas properties are analyzed. The sensing tube is a small diameter metallic piece which is designed to respond rapidly

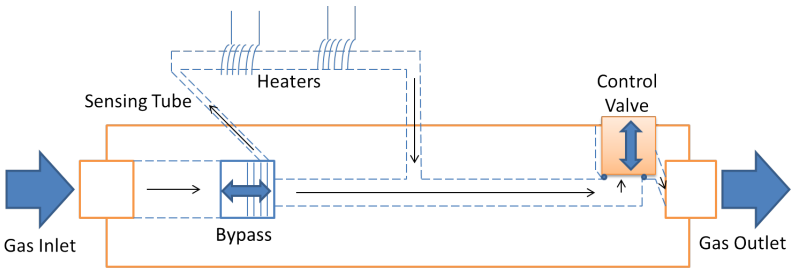

Figure A-1: A simplified overview of the basic components of a mass flow controller.

to changes in temperature that are provided by attached heaters. The bypass tube provides the initial pressure drop, and it is the piece replaced and calibrated when the MFCs are rebuilt to handle difference and/or larger volumetric flow rates. Physically handling the MFCs and causing the bypass to vibrate can alter its calibration, thus, it is necessary to keep the MFCs fixed and immobile.

The sensing tube has a number of heaters and temperature sensors along the tube. The tube must also be long enough such that the gas that enters reaches a steady state temperature before the last sensor. This is because the fundamental calculation of the mass flow rates involve the response of the gas to a heating source which is a function of its density and heat capacity. I.e. the rate of heat that the gas absorbs is the heat capacity per unit mass times the mass flow rate.

$$\text{HeatRateDeliveredtoGas}\left[\tfrac{J}{s}\right] = C_p\left[\tfrac{J}{gK}\right] * \text{FlowRate}\left[\tfrac{g}{s}\right] * (T_{\text{gasexit}} - T_{\text{enter}})\,[K]$$

Knowing the mass, temperature, and pressure allows one to calculate the volumetric flow rate in standard cubic centimeters per minute (sccm), the typical units for MFCs. The calculation assumes that the nominal temperature of the device lies in a certain range, because far outside of this range the heat capacity of the gas may change in a nonlinear manner. Thus, it is important that the MFCs are kept at a stable temperature. Finally, the control valve opens and closes to respond to a given flow rate calculated from the sensing tube data, it is an electronic feedback with the sensing tube to reach a given set point set by the operator.

Bibliography

[1] Darling, S. *Progress in Polymer Science* **2007**, *32*, 1152–1204.

[2] Bates, F. S.; Fredrickson, G. H. *Physics Today* **1999**, *52*, 32.

[3] Stoykovich, M. P.; Nealey, P. F. *Materials Today* **2006**, *9*, 20–29.

[4] Segalman, R. A. *Materials Science and Engineering: R: Reports* **2005**, *48*, 191–226.

[5] Stoykovich, M. P.; Nealey, P. F. *Science* **1997**, *276*, 1401–1404.

[6] Park, S.; Lee, D. H.; Xu, J.; Kim, B.; Hong, S. W.; Jeong, U.; Xu, T.; Russell, T. P. *Science* **2009**, *323*, 1030–1033.

[7] Stoykovich, M. P.; Müller, M.; Kim, S. O.; Solak, H. H.; Edwards, E. W.; de Pablo, J. J.; Nealey, P. F. *Science* **2005**, *308*, 1442–6.

[8] Ruiz, R.; Kang, H.; Detcheverry, F. A.; Dobisz, E.; Kercher, D. S.; Albrecht, T. R.; DePablo, J. J.; Nealey, P. F. *Science* **2008**, *321*, 936–939.

[9] Bita, I.; Yang, J. K. W.; Jung, Y. S.; Ross, C. A.; Thomas, E. L.; Berggren, K. K. *Science* **2008**, *321*, 939–43.

[10] Bates, F. S.; Fredrickson, G. H. *Annu. Rev. Phys. Chem.* **1990**, *41*, 525–557.

[11] Lodge, T. P.; Dalvi, M. C. *Phys. Rev. Lett.* **1995**, *75*, 657–660.

[12] Elbs, H.; Krausch, G. *Polymer* **2004**, *45*, 7935–7942.

[13] Jung, Y. S.; Ross, C. A. *Adv. Mater* **2009**, *21*, 2540–2545.

[14] Huang, E.; Russell, T. P.; Harrison, C.; Chaikin, P. M.; Register, R. A.; Hawker, C. J.; Mays, J. *Macromolecules* **1998**, *31*, 7641–7650.

[15] Lin, Z.; Kim, D.; Wu, X.; Boosahda, L.; Stone, D.; LaRose, L.; Russell, T. *Advanced Materials* **2002**, *14*, 1373–1376.

[16] Cheng, J.; Ross, C.; Thomas, E.; Smith, H.; Vancso, G. *Advanced Materials* **2003**, *15*, 1599–1602.

[17] Ross, C. A.; Jung, Y. S.; Chuang, V. P.; Son, J. G.; Gotrik, K. W.; Mickiewicz, R. A.; Yang, J. K. W.; Chang, J. B.; Berggren, K. K.; Gwyther, J.; Manners, I. *Proc. of SPIE* **2010**, *7637*, 76370H1–76370H7.

[18] Cheng, J. Y.; Mayes, A. M.; Ross, C. A. *Nature Materials* **2004**, *3*, 823–8.

[19] Cheng, J.; Ross, C.; Smith, H.; Thomas, E. *Advanced Materials* **2006**, *18*, 2505–2521.

[20] Bosworth, J. K.; Paik, M. Y.; Ruiz, R.; Schwartz, E. L.; Huang, J. Q.; Ko, A. W.; Smilgies, D. M.; Black, C. T.; Ober, C. K. *ACS Nano* **2008**, *2*, 1396–1402.

[21] Wu, Y.; Cheng, G.; Katsov, K.; Sides, S.; Wang, J.; Tang, J.; Fredrickson, G. H.; Moskovits, M.; Stucky, G. D. *Nature Materials* **2004**, *3*, 816–822.

[22] Sundrani, D.; Darling, S. *Nano Letters* **2004**,

[23] Chen, P.; Liang, H.; Shi, A.-C. *Macromolecules* **2007**, *40*, 7329–7335.

[24] Stoykovich, M.; Kang, H.; Daoulas, K.; Liu, G.; Liu, C. C.; de Pablo, J. J.; Müller, M.; Nealey, P. F. *ACS Nano* **2007**, *1*, 168–175.

[25] Olson, D.; Chen, L.; Hillmyer, M. *Chemistry of Materials* **2007**, *20*, 869–890.

[26] Segalman, R. A.; Hexemer, A.; Kramer, E. J.; Hayward, R. C. *Macromolecules* **2003**, *36*, 3272–3288.

[27] Turner, M. S.; Joanny, J. F. *Macromolecules* **1992**, *25*, 6681–6689.

[28] Liu, G.; Detcheverry, F.; Ramírez-Hernández, A.; Yoshida, H.; Tada, Y.; de Pablo, J. J.; Nealey, P. F. *Macromolecules* **2012**,

[29] Ji, S.; Nagpal, U.; Liao, W.; Liu, C.-C.; de Pablo, J. J.; Nealey, P. F. *Advanced Materials* **2011**, *23*, 3692–3697.

[30] Han, E.; Stuen, K.; La, Y.; Nealey, P. *Macromolecules* **2008**, *41*, 7019–7025.

[31] Wang, Q.; Yan, Q.; Nealey, P. F.; de Pablo, J. J. *The Journal of Chemical Physics* **2000**, *112*, 450–464.

[32] Kim, S. O.; Solak, H. H.; Stoykovich, M. P.; Ferrier, N. J.; DePablo, J. J.; Nealey, P. F. *Nature* **2003**, *424*, 411–414.

[33] Park, S.-M.; Stoykovich, M.; Ruiz, R.; Zhang, Y.; Black, C.; Nealey, P. *Advanced Materials* **2007**, *19*, 607–611.

[34] Xiao, S.; Yang, X.; Edwards, E. W.; La, Y. H.; Nealey, P. F. *Nanotechnology* **2005**, *16*, S324–S329.

[35] Ji, S.; Liu, C.-C.; Liu, G.; Nealey, P. F. *ACS Nano* **2009**, *4*, 599–609.

[36] Yang, J. K.; Jung, Y. S.; Chang, J. B.; Mickiewicz, R. A.; Alexander-Katz, A.; Ross, C. A.; Berggren, K. K. *Nature Nanotechnology* **2010**, *5*, 256–260.

[37] Fredrickson, G. H.; Ganesan, V.; Drolet, F. *Macromolecules* **2002**, *35*, 16–39.

[38] Fredrickson, G. H. *The Equilibrium Theory of Inhomogenous Polymers*; Oxford University Press: Oxford, England, 2006.

[39] Matsen, M. W.; Bates, F. S. *Macromolecules* **1996**, *29*, 1091–1098.

[40] Yang, Y.; Qiu, F.; Zhang, H.; Yang, Y. *Polymer* **2006**, *47*, 2205–2216.

[41] Matsen, M. W.; Thompson, R. B. *The Journal of Chemical Physics* **1999**, *111*, 7139.

[42] Mickiewicz, R.; Yang, J.; Hannon, A.; Jung, Y.-S.; Alexander-Katz, A.; Berggren, K. K.; Ross, C. A. *Macromolecules* **2010**, *43*, 8290–8295.

[43] Farrand, P.; Hussain, F.; Hennessy, E. *Medical Education* **2002**, *36*, 426–31.

[44] Bang, J.; Jeong, U.; Ryu, D. Y.; Russell, T. P.; Hawker, C. J. *Advanced Materials* **2009**, *21*, 4769–92.

[45] Lazzari, M.; López-Quintela, M. *Advanced Materials* **2003**, *15*, 1583–1594.

[46] Thurn-Albrecht, T.; Schotter, J.; Kästle, G. A.; Emley, N.; Shibauchi, T.; Krusin-Elbaum, L.; Guarini, K.; Black, C. T.; Tuominen, M.; Russell, T. *Science* **2000**, *290*, 2126–2129.

[47] Sivaniah, E.; Hayashi, Y.; Matsubara, S.; Kiyono, S.; Hashimoto, T. *Macromolecules* **2005**, *38*, 1837–1849.

[48] Son, J. G.; Bulliard, X.; Kang, H.; Nealey, P. F.; Char, K. *Advanced Materials* **2008**, *20*, 3643–3648.

[49] Jung, Y. S.; Ross, C. A. *Nano Letters* **2007**, *7*, 2046–2050.

[50] Kim, S.; Misner, M.; Xu, T.; Kimura, M.; Russell, T. *Advanced Materials* **2004**, *16*, 226–231.

[51] Bang, J.; Kim, S.; Drockenmuller, E.; Misner, M.; Russell, T.; Hawker, C. *Journal of the American Chemical Society* **2006**, *128*, 7622–7629.

[52] Freer, E. M.; Krupp, L. E.; Hinsberg, W. D.; Rice, P. M.; Hedrick, J. L.; Cha, J. N.; Miller, R. D.; Kim, H.-C. *Nano Letters* **2005**, *5*, 2014–2018.

[53] Nose, T. *Polymer* **1995**, *36*, 2243–2248.

[54] Jung, Y. S.; Chang, J. B.; Verploegen, E.; Berggren, K. K.; Ross, C. A. *Nano Letters* **2010**, *10*, 1000–5.

[55] Son, J. G.; Gwyther, J.; Chang, J. B.; Berggren, K. K.; Manners, I.; Ross, C. A. *Nano Letters* **2011**, *11*, 2849–55.

[56] Son, J. G.; Hannon, A. F.; Gotrik, K. W.; Alexander-Katz, A.; Ross, C. A. *Advanced Materials* **2011**, *23*, 634–639.

[57] Wu, S.; Brandrup, J.; Immergut, E.; Grulke, E.; Abe, A.; Bloch, D. *Polymer Handbook*; John Wiley & Sons: New York, 2005; pp 521–541.

[58] Albert, J. N. L.; Young, W.-S.; Lewis, R. L.; Bogart, T. D.; Smith, J. R. *ACS Nano* **2012**, *6*, 459–466.

[59] Paik, M. Y.; Bosworth, J. K.; Smilges, D. M.; Schwartz, E. L.; Andre, X.; Ober, C. K. *Macromolecules* **2010**, *43*, 4253–4260.

[60] Zettl, U.; Knoll, A.; Tsarkova, L. *Langmuir* **2010**, *26*, 6610–6617.

[61] Mukherjee, M.; Singh, A.; Daillant, J.; Menelle, A.; Cousin, F.; Saclay, C. E. A.; Cedex, F.-G.-s.-y.; Brillouin, L. L. *Macromolecules* **2007**, *40*, 1073–1080.

[62] Phillip, W. A.; Hillmyer, M. A.; Cussler, E. L. *Macromolecules* **2010**, *43*, 7763–7770.

[63] Leibler, L. *Macromolecules* **1980**, *13*, 1602–1617.

[64] Kim, H. C.; Russell, T. P. *J. Polym. Sci. Pol. Phys.* **2001**, *39*, 663–668.

[65] Knoll, A.; Magerle, R.; Krausch, G. *The Journal of Chemical Physics* **2004**, *120*, 1105–16.

[66] Kim, E.; Choi, S.; Guo, R.; Ryu, D. Y.; Hawker, C. J.; Russell, T. P. *Polymer* **2010**, *51*, 6313–6318.

[67] Bucholz, T. L.; Loo, Y. L. *Macromolecules* **2006**, *39*, 6075–6080.

[68] Russell, T. P.; Hjelm, R. P.; Seeger, P. A. *Macromolecules* **1990**, *23*, 890–893.

[69] Yan, H.; Blanford, C. F.; Lytle, J. C.; Carter, C. B.; Smyrl, W. H.; Stein, A. *Chem. Mater.* **2001**, *13*, 4314–4321.

[70] Albert, J. N. L.; Bogart, T. D.; Lewis, R. L.; Beers, K. L.; Fasolka, M. J.; Hutchison, J. B.; Vogt, B. D.; Epps, T. H. *Nano Letters* **2011**, *11*, 1351–1357.

[71] Cavicchi, K. A.; Berthiaume, K. J.; Russell, T. P. *Polymer* **2005**, *46*, 11635–11639.

[72] Peng, J.; Kim, D. H.; Knoll, W.; Xuan, Y.; Li, B.; Han, Y. *J. Chem. Phys.* **2006**, *125*, 647021–647028.

[73] Di, Z.; Posselt, D.; Smilgies, D. M.; Papadakis, C. M. *Macromolecules* **2010**, *43*, 418–427.

[74] Harant, A. W.; Bowman, C. N. *J. Vac. Sci. Technol. B* **2005**, *23*, 1615–1621.

[75] Xuan, Y.; Peng, J.; Cui, L.; Wang, H.; Li, B.; Han, Y. *Macromolecules* **2004**, *37*, 7301–7307.

[76] Tada, Y.; Yoshida, H.; Hirai, T.; Bosworth, J. K.; Dobisz, E.; Ruiz, R.; Takenaka, M.; Hayakawa, T.; Hasegawa, H. *Macromolecules* **2012**, *45*, 292–304.

[77] Vogelsang, J.; Brazard, J.; Adachi, T.; Bolinger, J. C.; Barbara, P. F. *Angew. Chem. Int. Ed.* **2011**, *50*, 2257–2261.

[78] Phillip, W. A.; O'Neill, B.; Rodwogin, M.; Hillmyer, M. A.; Cussler, E. L. *ACS Applied Materials & Interfaces* **2010**, *2*, 847–53.

[79] Mori, K.; Hasegawa, H.; Hashimotot, T. *Polymer* **1990**, *31*, 2368–2376.

[80] Hansen, C. M. *Hansen Solubility Parameters, A Users Handbook*; CRC Press, Florida, 2000.

[81] Bahadur, P.; Sastry, N. V. *Principles of Polymer Science*; Alpha Science International, Ltd, 2005.

[82] Helfand, E.; Tagami, Y. *J. Chem. Phys.* **1972**, *56*, 3592–3601.

[83] Hashimoto, T.; Shibayama, M.; Hiromichi, K. *Macromolecules* **1983**, *16*, 1093–1101.

[84] Bang, J.; Kim, B. J.; Stein, G. E.; Russell, T. P.; Li, X.; Wang, J.; Kramer, E. J.; Hawker, C. J. *Macromolecules* **2007**, *40*, 7019–7025.

[85] Guo, R.; Huang, H.; Chen, Y.; Gong, Y.; Du, B.; He, T. *Macromolecules* **2008**, *41*, 890–900.

[86] Jeong, J. W.; Park, W. I.; Kim, M. J.; Ross, C. A.; Jung, Y. S. *Nano Lett.* **2011**, *11*, 4095–4101.

[87] Zwietering, N. *Chem. Eng. Sci.* **1959**, *11*, 1–15.

[88] Cholette, A.; Cloutier, L. *Can. J. Chem. Eng.* **1959**, *37*, 105–112.

[89] Cavicchi, K. A.; Russell, T. P. *Macromolecules* **2007**, *40*, 1181–1186.

[90] Ginsburg, N.; Robertson, W. W.; Matsen, F. A. *J. Chem. Phys* **1946**, *14*, 511–517.

[91] Saez, C.; Compostizo, A.; Rubio, R. G.; Colín, A. C.; Peña, M. D. *J. Chem. Soc. Farad. T. 1* **1986**, *82*, 1839–1852.

[92] Ashcroft, S. J.; Clayton, A. D.; Shearn, R. B. *J. Chem. Eng. Data* **1979**, *24*, 195–199.

[93] Knoll, A.; Horvat, A.; Lyakhova, K.; Krausch, G.; Sevink, G.; Zvelindovsky, A.; Magerle, R. *Phys. Rev. Lett.* **2002**, *89*, 0355011–0355014.

[94] Chao, C.-C.; Ho, R.-M.; Georgopanos, P.; Avgeropoulos, A.; Thomas, E. L. *Soft Matter* **2010**, *6*, 3582–3587.

[95] Dalvi, M.; Lodge, T. *Macromolecules* **1993**, *26*, 859–861.

[96] Cheng, J. Y.; Rettner, C. T.; Sanders, D. P.; Kim, H.-C.; Hinsberg, W. D. *Advanced Materials* **2008**, *20*, 3155–3158.

[97] Rockford, L.; Liu, Y.; Mansky, P.; Russell, T.; Yoon, M.; Mochrie, S. *Physical Review Letters* **1999**, *82*, 2602–2605.

[98] Xiao, Q.; Wang, X.; Li, W.; Li, Z.; Zhang, T.; Zhang, H. *Journal of Membrane Science* **2009**, *334*, 117–122.

[99] Segalman, R.; Yokoyama, H.; Kramer, E. *Advanced Materials* **2001**, *13*, 1152–1155.

[100] Black, C.; Bezencenet, O. *IEEE Transactions On Nanotechnology* **2004**, *3*, 412–415.

[101] Ruiz, R.; Ruiz, N.; Zhang, Y.; Sandstrom, R.; Black, C. *Advanced Materials* **2007**, *19*, 2157–2162.

[102] Bosworth, J. K.; Black, C. T.; Ober, C. K. *ACS Nano* **2009**, *3*, 1761–6.

[103] Tang, C.; Lennon, E.; Fredrickson, G. *Science* **2008**, *322*, 429–432.

[104] Milliron, D. J.; Raoux, S.; Shelby, R. M.; Jordan-Sweet, J. *Nature Materials* **2007**, *6*, 352–6.

[105] Black, C. T. *Applied Physics Letters* **2005**, *87*, 163116.

[106] Naito, K.; Hieda, H.; Sakurai, M.; Kamata, Y.; Asakawa, K. *IEEE Transactions on Magnetics* **2002**, *38*, 1949–1951.

[107] Jung, Y. S.; Jung, W.; Tuller, H. L.; Ross, C. A. *Nano Letters* **2008**, *8*, 3776–80.

[108] Park, S.-M.; Craig, G. S. W.; La, Y.-H.; Nealey, P. F. *Macromolecules* **2008**, *41*, 9124–9129.

[109] Park, S.; Craig, G.; La, Y. *Macromolecules* **2007**, *40*, 5084–5094.

[110] Daoulas, K.; Müller, M.; Stoykovich, M.; Park, S.-M.; Papakonstantopoulos, Y.; de Pablo, J.; Nealey, P.; Solak, H. *Physical Review Letters* **2006**, *96*, 036104.

[111] Jung, H.; Hwang, D.; Kim, E.; Kim, B.-J.; Lee, W. B.; Poelma, J. E.; Kim, J.; Hawker, C. J.; Huh, J.; Ryu, D. Y.; Bang, J. *ACS Nano* **2011**, *5*, 6164–6173.

[112] Rose, F.; Bosworth, J. K.; Dobisz, E. A.; Ruiz, R. *Nanotechnology* **2011**, *22*, 035603.

[113] Kim, E.; Shin, C.; Ahn, H.; Ryu, D. Y.; Bang, J.; Hawker, C. J.; Russell, T. P. *Soft Matter* **2008**, *4*, 475.

[114] Shin, K.; Xiang, H.; Moon, S. I.; Kim, T.; McCarthy, T. J.; Russell, T. P. *Science* **2004**, *306*, 76.

[115] Henkee, C.; Thomas, E.; Fetters, L. *Journal of Materials Science* **1988**, *23*, 1685–1694.

[116] Yu, B.; Li, B.; Jin, Q.; Ding, D.; Shi, A.-C. *Soft Matter* **2011**, *7*, 10227.

[117] Ruiz, R.; Dobisz, E.; Albrecht, T. *ACS Nano* **2011**, *5*, 79–84.

[118] Peng, Q.; Tseng, Y.; Darling, S.; Elam, J. *ACS Nano* **2011**, *5*, 4600–4606.

[119] Ilievski, F.; Ross, C. A. *Journal of Vacuum Science & Technology B: Microelectronics and Nanometer Structures* **2010**, *28*, 42.

[120] Moon, H.-S.; Shin, D. O.; Kim, B. H.; Jin, H. M.; Lee, S.; Lee, M. G.; Kim, S. O. *Journal of Materials Chemistry* **2012**, *22*, 6307.

[121] Jeong, J. W.; Park, W. I.; Do, L.-M.; Park, J.-H.; Kim, T.-H.; Chae, G.; Jung, Y. S. *Advanced Materials* **2012**, *24*, 3526–31.

[122] Park, S.-M.; Liang, X.; Harteneck, B. D.; Pick, T. E.; Hiroshiba, N.; Wu, Y.; Helms, B. A.; Olynick, D. L. *ACS Nano* **2011**, *5*, 8523–8531.

[123] Voet, V. S. D.; Pick, T. E.; Park, S.-M.; Moritz, M.; Hammack, A. T.; Urban, J. J.; Ogletree, D. F.; Olynick, D. L.; Helms, B. A. *Journal of the American Chemical Society* **2011**, *133*, 2812–5.

[124] Jeong, S.-J.; Moon, H.-S.; Kim, B. H.; Kim, J. Y.; Yu, J.; Lee, S.; Lee, M. G.; Choi, H.; Kim, S. O. *ACS Nano* **2010**, *4*, 5181–5186.

[125] Tavakkoli, K.; Hannon, A.; Gotrik, K.; Alexander-Katz, A.; Ross, C.; Berggren, K. *Advanced Materials* **2012**, *24*, 4249–4254.

[126] Tavakkoli K. G., A.; Gotrik, K.; Hannon, A.; Alexander-Katz, A.; Ross, C.; Berggren, K. *Science* **2012**, *336*, 1294–1298.

[127] Duan, H.; Winston, D.; Yang, J. K. W.; Cord, B. M.; Manfrinato, V. R.; Berggren, K. K. *Journal of Vacuum Science & Technology B: Microelectronics and Nanometer Structures* **2010**, *28*, C6C58.

[128] Gotrik, K. W.; Hannon, A. F.; Son, J. G.; Keller, B.; Alexander-Katz, A.; Ross, C. A. *ACS Nano* **2012**, *6*, 8052–8059.

[129] Hamley, I. W.; Koppi, K. a.; Rosedale, J. H.; Bates, F. S.; Almdal, K.; Mortensen, K. *Macromolecules* **1993**, *26*, 5959–5970.

[130] Foerster, S.; Khandpur, A.; Zhao, J.; Bates, F.; Hamley, I.; Ryan, A.; Bras, W. *Macromolecules* **1994**, *27*, 6922–6935.

[131] Khandpur, A.; Foerster, S.; Bates, F.; Hamley, I.; Ryan, A.; Bras, W.; Almdal, K.; Mortensen, K. *Macromolecules* **1995**, *28*, 8796–8806.

[132] Kim, G.; Libera, M. *Macromolecules* **1998**, *31*, 2670–2672.

[133] Fukunaga, K.; Elbs, H.; Magerle, R.; Krausch, G. *Macromolecules* **2000**, *33*, 947–953.

[134] Kim, S. H.; Misner, M. J.; Russell, T. P. *Adv. Mater.* **2004**, *16*, 2119–2123.

[135] Albalak, R.; Capel, M.; Thomas, E. *Polymer* **1998**, *39*, 1647–1656.

[136] Zhang, X.; Harris, K. D.; Wu, N. L. Y.; Murphy, J. N.; Buriak, J. M. *ACS Nano* **2010**, *4*, 7021–7029.

[137] Park, W. I.; Kim, K.; Jang, H.-I.; Jeong, J. W.; Kim, J. M.; Choi, J.; Park, J. H.; Jung, Y. S. *Small* **2012**,

[138] Gao, P.; Mackley, M. *Proceedings: Mathematical and Physical Sciences* **1994**, *444*, 267–285.

[139] Singh, A.; Mukherjee, M. *Macromolecules* **2003**, *36*, 8728–8731.

[140] Mokarian-Tabari, P.; Collins, T. *ACS Nano* **2011**, *5*, 4617–4623.

[141] Roskov, K. E.; Epps, T. H.; Berry, B. C.; Hudson, S. D.; Tureau, M. S.; Fasolka, M. J. *Journal of Combinatorial Chemistry* **2008**, *10*, 966–73.

[142] Jha, P. K.; Zwanikken, J. W.; Detcheverry, F. A.; de Pablo, J. J.; Olvera de la Cruz, M. *Soft Matter* **2011**, *7*, 5965.

[143] Shim, J. J.; Johnston, K. P. *The Journal of Physical Chemistry* **1991**, *95*, 353–360.

[144] DeSimone, J. M. *Science* **2002**, *297*, 799–803.

[145] O'Driscoll, B. M. D.; Griffiths, G. H.; Matsen, M. W.; Hamley, I. W. *Macromolecules* **2011**, *44*, 8527–8536.